A Novel Geometric Theory of On-Machine Tool Measurement and Practical, Optimal Approaches to Highly Accurate and Efficient On-Machine Measurement

Zixi Fang

A Thesis

In the Department

of

Mechanical, Industrial, and Aerospace Engineering

Presented in Partial Fulfillment of the Requirements

For the Degree of Doctor of Philosophy at

Concordia University

Montreal, Quebec, Canada

August 2022

© Zixi Fang, 2022

CONCORDIA UNIVERSITY

School of Graduate Studies

This is to certify that the thesis prepared

By: Zixi Fang

Entitled: A Novel Geometric Theory of On-Machine Tool Measurement and Practical, Optimal Approaches to Highly Accurate and Efficient On-Machine Measurement

and submitted in partial fulfillment of the requirements for the degree of

Doctor of Philosophy (Mechanical Engineering)

complies with the regulations of the University and meets the accepted standards with respect to originality and quality.

Signed by the final examining committee:

Dr. Sébastien Le Beux Chair

Dr. Deyi Xue External Examiner

Dr. Liangzhu Wang External to Program

Dr. Chun-Yi Su Examiner

Dr. Youmin Zhang Examiner

Dr. Zezhong Chen Supervisor

Approved by Dr. Ivan Contreras

Chair of Department or Graduate Program Director

Dr. Mourad Debbabi

Dean of Faculty

Date: August 03, 2022

ABSTRACT

A Novel Geometric Theory of On-Machine Tool Measurement and Practical, Optimal Approaches to Highly Accurate and Efficient On-Machine Measurement

Zixi Fang, Ph.D.

Concordia University, 2022

Modern industry trends to smart machining that improves productivity at a low cost. The kernel technology of intelligent manufacturing is the automatic on-machine measurement (OMM). When applying OMM technology to computer numerical control (CNC) machines, in-situ measurement takes place in the machining environment without the need of unloading the tool and the part. However, adverse measurement environment, limitations on the efficiency of data capturing and processing, and diversified measured objects render efficient and accurate OMM very difficult. Holistic solutions are needed to advance OMM technology and therefore many scientific topics are involved. This work primarily focuses on geometric modeling of the on-machine cutting tool measurement and kinematic modeling for the calibration process of both the probe and the machine.

On-machine cutting tool measurement often takes place on a laser tool setter. However, the geometry principles of the gauging mechanisms of laser tool setters are complicated and had not been studied before. This dissertation modeled such a gauging mechanism and presented virtual simulations of the measurement processes on laser tool setters based on geometry principles.

The virtual simulations can predict and compensate the measurement errors, allowing for accurate tool setter calibration processes in practical situations.

For cutting tool measurement, the tool length characteristic curve for measurement of round-insert mills is discovered. The derivation of the tool length characteristic curve was carried out by modeling the geometries of tool length measurement processes on a laser tool setter. Based on this characteristic curve, an accurate and efficient approach to measuring lengths of mills with round inserts and bottom cutting edge wear is proposed.

Current techniques for probe calibration and machine calibration assume the impractical situations where either the machine is accurate or the location of the probe is accurately known. To address these drawbacks, the actual kinematic model of a six-axis belt grinding CNC machine with a customized add-on probe is built in this dissertation. Using this model along with a specially designed artifact can facilitate the simultaneous calibration of the probe position and the machine geometry error.

Keywords: on-machine tool setting; calibration; laser tool setter; gauging mechanism; multi-axis CNC machine tool; error identification

ACKNOWLEDGEMENTS

I first wish to express my sincerest gratitude and appreciation to my supervisor, Dr.Chevy Chen, for his priceless guidance and insights that lead me through this research. I have gained valuable research experience and technical skills under his supervision. Since 2013, Dr. Chen and I have been working on on-machine measurement technologies. We started in a machine shop far away from the university. We had to travel constantly to test our programs and algorithm with minimum help from outside sources. In the past decade, we saw the prototype of on-machine cutter measurement form, and eventually, the technology got accepted by many manufacturing companies for daily production. One of the most vivid memory was that Dr. Chen and I waited until 3 A.M. after the night shift of the machine shop ends. Then we conducted our experiment until dawn. The commitment to scientific research that Dr. Chen showed greatly influenced me and would keep on propelling me in my future life.

I would also like to thank my fellows in our lab for their generous support and ideas when I encountered problems. Specifically, Mr. Tao Fang and Mr. Zhifu Yi, in particular, helped me tremendously with the work conducted on the third part of this thesis.

Finally, I give my special thanks to my parents and my girlfriend for their unselfish love. The complex nature of a Ph.D. work is bounded to be challenging to any individual and I am no exception. The countless time that I was in an emotional trough, it was their unconditional support that helped me through every hurdle. I cannot thank them enough.

Contents

List of Figures

List of Tables

Chapter 1

Introduction

1.1 Background

Modern industry always directs manufacturers to effectively produce various complex parts with tight tolerance at a low cost. In the context of Industry 4.0, different intelligent manufacturing solutions have been sought for production optimization by manufacturing firms to remain competitive [1]. Intelligent manufacturing distinguishes itself in its ability of self-awareness and self-correction[2]. One kernel technology of intelligent manufacturing is the automatic on-machine measurement, which is a synergy between measurement operations and manufacturing processes. Specifically, sensors are used to monitor and capture manufacturing systems parameters, simultaneously with the manufacturing processes. The collected information is used in two folds: 1) serve as verification of the current product quality and tool status; 2) provide a basis for immediate self-adjustment on the manufacturing processes. As a result, it creates a closed-loop process control paradigm that enables just-in-time quality controls over the manufacturing processes, promoting manufacturing zero defects products. In addition, it boosts productivity by reducing cycle time and eliminating non-value-adding activities and resources [3].

Computer numerical control (CNC) machining remains a major means of fabricating mechanical components in the aerospace and automotive industries. During CNC machining processes, machine geometry errors, tool dimensional errors, continuous tool wear and part/tool deflections, etc., are reflected on the machined workpiece. Applying on-machine measurement (OMM) technology to facilitate intelligent, automatic, and non-disruptive workflow is now indispensable and inevitable. In OMM, smart and automatic in-situ measurement takes place on the CNC machines without the need of unloading the tool and the part, so it is convenient to perform periodic checks of cutting tools and part status for corrective actions. Figure 1.1(a) shows a cutting tool is measured by a laser tool setter installed on the machine table and Figure 1.1(b) shows a touch trigger probe that is driven by a CNC machine tool to measure a part surface. Applications for machine tool calibration using OMM technology are also studied in recent research. The tight measurement and manufacturing integration offered by OMM is defined as one “the future of manufacturing metrology” in 2011[4]. Employing OMM as its kernel, the concept “closed-door machining”, applies adaptive machining strategies based on the OMM acquired data to deliver “right-first-time” products[5], which is continuously being adopted by giant manufacturers such as Pratt & Whitney, Safran, and Rolls-Royce [6-8].

(a) (b)

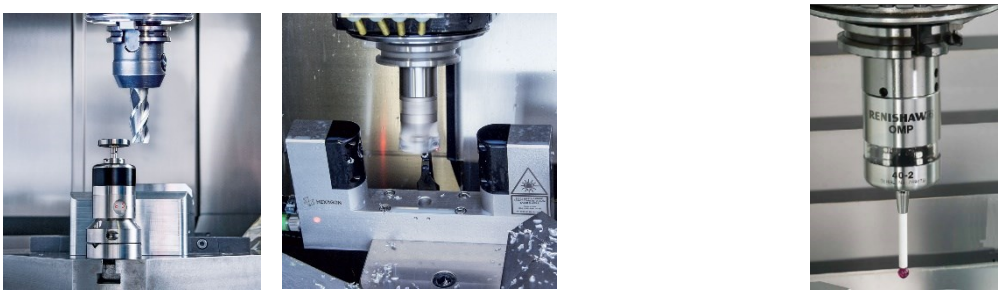

Figure 1.1 (a) On-machine tool setters and (b) an on-machine touch triggered probe.

Despite its benefits, developing efficient and accurate on-machine measurement systems is not trivial. The rather adverse working environment is the major concern of OMM and it distinguishes OMM systems from the offline measurement systems. Traditional offline measurement systems, such as coordinate measurement machines for part coordinate measurement and optical tool pre-setters for tool geometries measurement, operate in a temperature, humidity-controlled environment. The machines that drive these traditional measurement sensors (such as touch-trigger probes or laser scanning probes) are designed specifically for measurement tasks. Since no cutting forces would exert on the machine structure, the machines can be specifically designed. Under these special conditions, traditional offline measurement systems can achieve high accuracies. However, OMM is performed on a CNC machine where machining takes place and the delicate ideal measurement environment cannot be guaranteed. A CNC machine is designed to withstand large cutting forces. Thus, it is more rigid but less accurate and it tends to suffer from thermal deformations and geometry deformations

due to machining tasks. In addition, OMM calls for efficient measurement processes, quick data processing, and data transmission because in-process measurement tasks should improve, instead of hampering, productivity. Easy integration between the measurement device and the CNC machine should also be considered so that OMM can be widely applied. Under this requirement, the most widely accepted devices are on-machine probes and tool setters, and their accompanied controlling and data processing programs are written in the MACRO language of the CNC machine, which has limited functionalities. However, the objects being measured by these devices are complicated. This dilemma calls for careful studies and modeling of the measurement process to find a smart way for the given measurement tasks. In summary, the studies of OMM systems require a holistic solution to provide accurate measurement results efficiently in a general manufacturing environment.

1.2 Literature review

1.2.1 Fundamentals of on-machine measurement technologies

On-machine measurement integrates measurement devices on the machine to allow in-situ measurement tasks to take place without the need of unloading the measured object off the machine. One typical setup of on-machine measurement systems is shown in Figure 1.2, which facilitates the on-machine measurement of parts. In this case, a measurement device called a touch trigger probe is loaded on the CNC machine spindle. A wireless receiver is also set up at the corner of the machine. The receiver is connected to the CNC control. During the measurement task, the CNC machine drives the probe to touch the part surface and when the

probe is triggered, a signal will be sent from the probe to the receiver. When the receiver acquires the signal, it will send issued a signal to the CNC control and the CNC control capture the location of the sensor in the machine coordinate system. Eventually, the system can calculate the location of the surface point being measured.

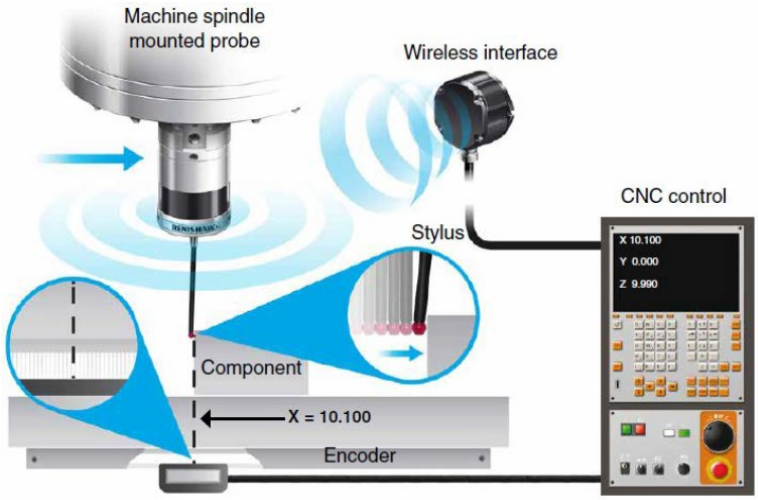

Figure 1.2 On-machine measurement system for part measurement[9]

Another typical setup is shown in Figure 1.3, where it facilitates the measurement of a cutting tool on a machine. The measurement device is a laser tool setter. It is mounted on the machine table and is connected to the CNC control. During the tool measurement, the tool is driven by the CNC machine to block the laser beam. Once the threshold value of the laser beam is reached, a signal is sent to the CNC control, and the tool position in the machine coordinate system is recorded. Then the tool dimensions are calculated.

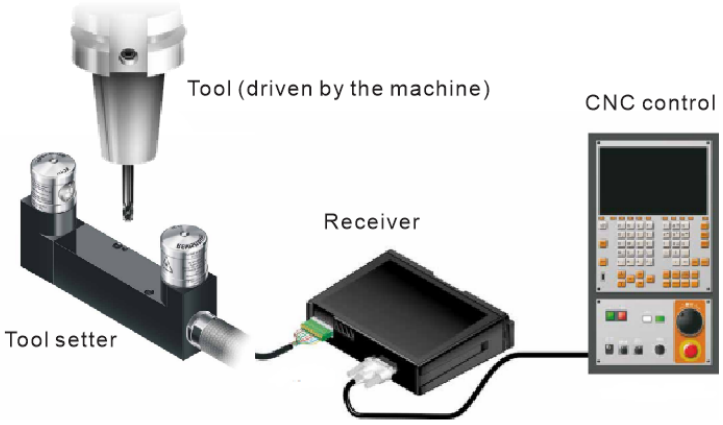

Figure 1.3 On-machine measurement system for tool measurement[9]

Over the years, numerous researches have been developed to advance on-machine measurement technologies. ISO-230[10] lists influences on the performance of on-machine measurement systems, which include:

a) Repeatability of the machine tool;

b) Geometric accuracy of the machine tool;

c) Contamination of objects being measured (detected);

d) Probing error and repeatability of the probing system;

e) Probing system qualification;

f) Thermal effects on the machine tool, probing system, artifact, and workpiece/tool;

g) Feed speeds and accelerations during measurement;

h) Standoff and overtravel distances;

i) Time delay and time delay variation between probing signal and read-out machine tool position transducers;

j) The surface of the workpiece/tool probed.

With the advance in manufacturing technology, numerous products and solutions have been provided to address these factors. Currently, modern machine shops are operating in a temperature-controlled environment. The newer generations of CNC machines have advanced functions such as thermal error compensations[11] and can position as accurately as 1 micron even when they are performing machining tasks. At the same time, for existing convention CNC machines, machine tool error detection devices and solutions, such as laser interferometers, R-test, and ball-bar systems are now commercially available to provide accurate machine error measurement. Therefore, proper adjustments can be made. In addition, the measuring devices have become more accurate over the years. A typical on-machine touch-triggered probe now can achieve lobbing errors of less than 2 microns and 0.1-micron repeatability [9]. While typical tool setters can detect the tool immediately when the laser beam is blocked, with 0.1-micron repeatability.

1.2.2 Literature review on the research and development of on-machine measurement.

Over the years, numerous approaches and research have been developed that can help improve the performance of the on-machine measurement. The objectives of these approaches are to measure, predict and compensate for measurement process errors originating from the relatively adverse operating environment. Research and methods are usually grouped by

addressing issues from the measurement devices and their associated measurement processes. The measurement devices often include the machine, the probe, and the tool setter.

1) Methods to improve the accuracy of the machine

The machine tool motion inaccuracy in following planned paths is one the most influential factors that limit the performance of OMM systems. According to ISO-230(1), the term volumetric performance is used to describe "the ability of a machine tool to perform the intended multi-axes functions anywhere within the entire machine working volume or a smaller volume as agreed between the manufacture and user"[10]. The volumetric error may be induced by the imperfect machine structure components, errors from the control system, the thermal deformation during operating tasks, vibration, cutting loads, etc. With the machine volumetric errors, the actual machine positions do not accord with the command positions [10, 12]. Consequently, different positions of the part of the cutter will be measured by the measurement device, resulting in measurement error. In the field of on-machine measurement, due to the absence of cutting forces, the most influential factors are imperfect machine structure components (quasi-static geometric errors) and thermal deformation errors. Nevertheless, the volumetric error of the machine should be calibrated and compensated frequently.

Hsu and Wang [13] summarized that the technical route of machine volumetric compensation techniques generally comprises three steps: (1) developing an error model for machine tools, (2)

using a measuring device to obtain data and solve the error models, and (3) conducting error compensation using the error model. The following presents the current techniques and research.

Volumetric modelling

Schultschik [14] in 1977 first described the volumetric model to represent the errors of machine components mathematically. Researchers employ homogeneous transformation matrices that incorporate geometry errors to develop machine kinematic models [15-17] since 1986. Screw theories [18, 19] were favored by other researchers.

By far, building machine kinematic models with homogeneous transformation matrices (HTM) is the most widely accepted method. With the advance in CNC machine technologies, kinematic models for various machines were studied. For example, Kiridena et al. developed kinematics models for commonly seen five-axis CNC machines[16]. Srivastava, et al., used HTM to model the angular errors and linear errors of a five-axis CNC machine. Their model also incorporated thermal errors[17].

Lee proposed a multi-degree-of-freedom piezoelectric sensor for machine volumetric error measurement based on a rigid multi-body system [20]. Zhu et al. presented a generic geometric error model for machine tools using a rigid multi-body system and theory [19]. Yang et al. established the geometric errors identification model for the five-axis machine based on screw

theory so the forward and inverse kinematics models are explicit and can be solved efficiently [21].

Geometric error measurement

The techniques for geometric error measurement can be categorized as direct measurements and indirect measurements. In direct measurements, efforts are made to isolate a single machine axis so that the measurement of the mechanical errors would not be interfered with by other axes [22]. Some of the direct measurement methods, which involve the usage of special gauges, are standardized in ISO 10791[12, 23-25]. The most widely accepted technique in direct measurements is the application of laser interferometers, such as Renishaw's XL-80. With supporting lens and software, laser interferometers can calibrate the positional accuracy and the pitch and yaw errors along a linear axis, straightness of linear axes, and positional accuracy of rotary axes [26, 27]. The lack of efficiency often hinges on direct measurement techniques to be applied frequently.

In indirect measurements, analyses are performed on the actual "tooltip" motions of the machine, since these motions are the superposition of all single error parameters [28]. The indirect measurements are usually used for machines with rotary axes. The schemes often involve developing kinematic models for the machines to describe the relation amongst "tooltip" position, machine command values (coordinates data input in G-codes to control the machine

movement), and geometric errors [4, 6, 19]. To track the tooltip position and obtain the aforementioned relation, many devices and methods have been invented over the years, for example, double ball bar tests [20-23], R-test [24, 25], machining tests [5, 26], and on-machine measurement artifacts [1-3, 27].

Particularly, in recent years, OMM techniques for machine geometric error have been a focus for researchers. Compared with other indirect methods, OMM techniques are the least demanding in technicians' experience and more efficient. Ibaraki et al. first proposed a scheme to evaluate the machine error by on-machine probing a cube [28]. Givi and Mayer [29]performed OMM tasks on a workpiece that is produced by a set of machining tests. The measurement results are used to identify the machine errors. Chen et al. presented a method to identify the machine rotary axes location errors by probing a sphere on a machine [30]. Renishaw provides AxiSet CheckUp commercial software, in which a sphere is probed by a touch-triggered probe, to facilitate the verification of rotary axes' linear location errors[9]. However, the software does not detect squareness errors. Major CNC control brands such as FANUC [31], SIEMENS[32], etc. provide compatibility for these OMM systems, making these systems widely available and very convenient for periodic machine checkups. Nevertheless, the OMM systems provide tremendous convenience for periodic machine checkups and compensation for the machine geometric errors. Therefore, this dissertation aims to contribute to the field of OMM machine calibration.

Thermal error measurement

The motions of machine components and environment heat sources often contribute to the temperature changes in the machine structures and thus lead to the deformation of machine motions. The ideal relative position and orientation between the tool and the on-machine measurement tool setter (or the probe and the workpiece) might be altered due to machine thermal error. As an important topic in machine volumetric error measurement and compensation, various research and techniques have been published.

Fraser et al. established a generalized model for CNC machine thermal deformation, and generalized heat transfer functions and verified it with finite element methods (FEM) [33]. Subsequently, they proposed a generalized modeling technique for real-time thermal deformation compensation [34]. Zou investigated the thermal effects generated by the friction linear rolling guides using FEM methods [35]. Gomez-Acedo et al. proposed a method for compensating thermal errors of large gantry-type machine tools by verifying their FEM models with data obtained from resistance temperature detectors[36]. Nowadays, advanced CNC machines are equipped with temperature sensors to detect temperature changes in the key components of the machine. Artificial intelligent methods are incorporated into the CNC control for real-time temperature control [11]. In this research, the machines used in the experiment were placed in a temperature-controlled room and it was assumed that the temperature factors are negligible to the obtained data.

2) Methods to improve the accuracy of the probe

For part on-machine measurement, touch-trigger probes are often used. Traditionally, touch-trigger probes are used frequently for CMM jobs and are considered very accurate once their effective probe tip radii are calibrated [37, 38]. The process usually involves sampling a standard artifact from different directions and applying least-square fit methods to the sampled data to calculate a value for the probe tip radius. This compensation method is known as the probe calibration method [38]. The research work published by Jarman and Traylor [39] identifies probing errors that exist mainly due to the probe pretravel behavior and blending deflections of the probe stylus being the reason for this behavior. Cauchick-Miguel et al.'s detailed experiment, measuring a Taylor-Hobson hemisphere, demonstrated that the pretravel distance show antistrophic characteristics due to the probe's internal structure, specifically, a three-lob pattern [40] and suggested the probe pretravel distance errors need to be compensated depending on the probing directions. To facilitate the compensation depending on probing directions, error mapping methods are frequently used in the industry [41]. However, error mapping methods cannot accurately compensate for errors in the non-recorded probing directions. It is also time and memory-consuming. Shen and Moon proposed using neural network methods to find a best-fit curve for the relatively smaller experiment data set. The curve can be used to find the pretravel distance of any given probing direction [42]. Mayer et al. surveyed the probe stylus deflection behavior using a 3D camera and their experiment data and presented a model for probing pretravel distance prediction [43]. These methods are data-driven. Estler et al. [44], Shen and Springer [45], Wozniak et al.[37], Jankowski and Wozniak [46] investigated and modeled the probe pretravel behavior by analyzing the force distribution of the probe's internal structure and the probe stylus deflection during probing procedures. Their works describe parametric

mechanistic models useful for the pretravel distance prediction at any given probing direction. When using these models for coordinate measurement machine probes errors compensation, they usually generate satisfactory results.

3) Methods to improve the accuracy of the tool setters

Laser tool setters are often used for OMM tool measurement process. Laser tool setters employ non-contact laser technology and have been widely used on CNC machines. Reiser [47] described a laser system with a photo-electric sensor for tool setting and tool breakage detection. When the voltage of the photoelectric sensor on the receiver identifies that the tool blocking 50% of the laser beam, the system triggers a signal. It can gauge tool size on CNC machines. Ryabov *et al*. [48] developed a prototype of on-machine tool condition monitoring. It projected the laser beam onto a cutter, and the reflected laser is in different signal patterns under different circumstances, such as tool rotation, tool vibration, and tool chipping. Panart *et al*. [49] presented a method to track the sub-micrometer gap between the cutter tip and the workpiece surface using the far-field laser diffraction principle. Chen and Zhang [50] reported a machine vision system to monitor on-machine tool wear. Their work was mostly focused on assessing tool wear and predicting tool life. Shi *et al*. [51] concentrated on the ultra-precision machining process. Based on the Fraunhofer diffraction theory, they set up an experiment to gauge the sharp diamond tool size. They [52] also studied the effects of the measurement device misalignment with a machine axis on the tool setting.

As a non-contact tool measurement system with high accuracy, laser tool setters are commercially available [9, 53, 54]. Generally, a laser tool setter is equipped with a laser transmitter and a receiver. A laser beam is emitted from the transmitter to the receiver. To gauge a tool, it blocks the laser beam. When the signal intensity on the photodiode of the receiver is at the threshold, the tool setter triggers a signal. Results of testing the tool setter in the lab have demonstrated its repeatability $\pm 1 \mu m$ [53-55]. According to the works [56, 57], the working principles of the laser tool setter are described as follows. The tool blocking the laser beam reduces the light intensity on the photodiode in the receiver, and the intensity pattern drops in measurement. The laser intensity determines the photodiode voltage, and it is monitored by a dedicated circuit. The sampling rate in monitoring the voltage is higher than 96K Hz. The intensity pattern is pre-programmed and recognized by a dedicated circuit. This method can reject false signal triggers due to coolant droplets and debris. Once the circuit recognizes the tool blocking the laser beam and the photodiode intensity dropping by 50%, the tool setter triggers a signal. The photodiode property is studied in the research of Park *et al*. [58] and Lee *et al*. [59]. The researchers have proven that if the tool diameter is significantly larger than the laser beam, the receiver power is linearly related to the ratio of the shaded area to the unshaded area on the receiver screen. However, if the tool size is comparable to the laser beam diameter in micro-machining, the light diffraction is significant and the linear relationship does not hold.

Studies have shown that the laser tool setters suffer from several error sources in practical application, including their installation misalignment and tool geometric differences. Other sources include the low-quality measuring rods, the machine spindle run-out [60, 61], and the

spindle speed and the feed rate [56]. Unfortunately, these error sources are ignored by the current applications of non-contact laser tool setters [62]. Renishaw [56] and Lee *et al*. [63] have made attempts to model the measurement errors in terms of the tool geometric error and setup error of the laser tool setter. They modeled the tool as a true cylinder and the laser beam as an inclined line. Then the measurement errors are calculated based on the front view and the top view of the setup. Their method is approximated and cannot calculate the actual measurement error. Milton *et al*. [64] designed a set of experiments based on statistical analyses to identify the best feed rate and spindle speed for referencing laser tool-setters. Their method is experimentally based and does not calculate the measurement error due to the error sources. Unfortunately, there is no research on a completed tool setting model using laser tool setters.

1.3 Research problems and objectives

1.3.1 Research problems

The literature review in the last section provides the general directions of theories and technologies in the field of on-machine measurement:

1) Mathematical modeling of the physical and geometrical working principles of the measurement device (a probe) can predict the errors that occur in the measurement process, which can be compensated accordingly.
2) Based on the machine kinematic models, the geometric errors of the machine can be identified and measured by using on-machine measurement devices. The CNC controls often provide functionalities for rapid geometric error measurement and compensation.

3) Modern CNC machines and commercially available on-machine measurement devices provide very high accuracy and repeatability under ideal working conditions.

From the literature review, it can be seen that few researchers emphasized the science in the measurement processes. The work focusing on the measurement process can help develop advanced measurement strategies that improve both accuracy and efficiency by studying the working measuring mechanism and the manufacturing process. The final measurement accuracy not only depends on the accuracy of the measurement device but also depends on how the object is being measured. Unfortunately, this is generally neglected by the current research. In addition, although prior researchers have published works on machine calibration using kinematic modeling, this technique is still not perfect. This dissertation attempts to fill these voids. Specifically, three gaps in the current research can be identified and should be solved with this dissertation.

On-machine cutting tool measurement is rarely discussed in the current research. Laser tool setters are commonly used devices for on-machine cutting tool measurement. The geometry principles of the triggering mechanisms are complicated and they affect the accuracy of the measurement process. However, these geometry principles have not yet been studied and thus the accuracy of the measurement process is estimated based on trial and error. In the meantime, the speed of the measurement process tends to be very conservative.

Cutting tools have complex geometries and they are traditionally measured on a tool presetter. When a cutter is measured on a laser tool setter on-machine, its complex geometries reflect as measurement errors. Current methods for on-machine cutting tools measurement simplify the problem by rotating the tool at a very high speed and measuring with a very small feed rate. These methods discard valuable tool geometry data such as the wear of each flute that can benefit the manufacturing process and they are also very inefficient. To the author's knowledge, there is a lack of research on modeling the cutting tool on-machine measurement process and thus there is a lack of an effective and accurate way of cutting tools.

In the prior research on calibrating the CNC machines using on-machine measurement, kinematic models were built with the position of the probe in the machine coordinate system known before the calibration. However, the machine axes geometric errors deviate the probe from its ideal position. The simultaneous calibration of both the machine and probe has posed a challenge to the current scheme of on-machine calibration.

1.3.2 Thesis objectives

This thesis sets the objectives to address the current research gaps and to contribute to the geometry modeling research field (Chapter 2 and Chapter 3) and kinematic modeling research field (Chapter 4) of on-machine measurement technology. The thesis is organized as the follows:

- In Chapter 2, the geometry principles of the laser tool setters are investigated and are modeled mathematically. Subsequently, virtual simulations of the measurement processes on laser tool setters are developed using geometry principles. These virtual

simulations predict the measurement errors and compensating for those errors allows for accurate tool setter calibration processes in practical situations.

- In Chapter 3, the characteristic curve for length measurement of round-insert mills is discovered, using both the kinematics and geometric fundamentals of measuring the length of a round insert mill. Based on this characteristic curve, an accurate and efficient approach to measuring lengths of mills with round inserts and bottom cutting edge wear is proposed and a new scientific approach is established to accurately and efficiently measure the mill length on a laser tool setter.
- In Chapter 4, the actual kinematic model of a six-axis belt grinding CNC machine with a customized add-on probe is built. Using this model along with a specially designed artifact can facilitate the simultaneous calibration of the probe position and the machine geometry error.
- Chapter 5 conducts a conclusion.

Chapter 2 Precise Mathematical Model for Computer Simulation of Gauging with On-machine Laser Tool Setters in Practical Situations and Its Application in the Calibration Process

2.1 Introduction to on-machine tool setting

On-machine tool setting with laser tool setters is a process of determining cutter size (e.g., cutter diameter and length) in the part machining process. This emerging technique is crucial to improving part accuracy, implementing unmanned machining, and reducing production time. In machining of metal parts, cutters wear down with smaller diameters and shorter lengths. Before machining, the machinist manually measures the cutters' sizes with an offline presetter and keys in their values to the machine control. After machining some parts, a cutter wears down. Then, the machinist has to unclamp the cutter from the spindle, measure its size with the presetter, key its offsets into the machine control, and put it back on the spindle. It is very time-consuming and inconvenient for the machinist to set cutters with a presetter, so they often do not set the cutters' wear offsets in machining. Consequently, wear offsets of the cutters are not compensated in part machining, resulting in large machining errors. Therefore, in the manufacturing industry, it is in high demand that cutters are regularly gauged on-machine in the part machining process to cut parts accurately and precisely.

At present, many CNC machining centers have laser tool setters installed. There are two systems of laser tool setter: the fixed and the separated systems (see Figure 2.1). The fixed system has the transmitter and the receiver units housed within a single assembly, and the units are less than 400 mm apart (see Figure 2.1(a)). The separated system has an individual transmitter and receiver assemblies, and they can be 2000 mm apart (see Figure 2.1(b)). Under the perfect lab conditions, the tool setting precision of the laser tool setters reaches 0.1 micro, which is much better than what the industry requests. Thus, machinists desire that they can quickly and accurately gauge cutters on-machine with laser tool setters, instead of manually setting cutters with offline presetters.

(a)

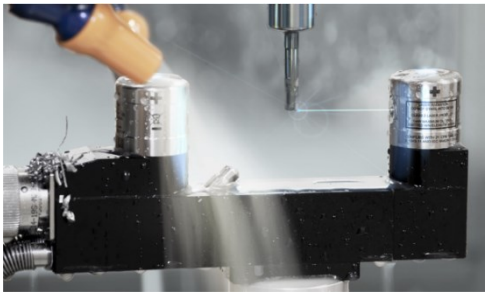

(b)

Figure 2.1 (a) A fixed system of laser tool setters, and (b) a separated system of laser tool setters.

Due to the quality hardware of the laser tool setters, their physics mechanism can ensure precise tool setting. However, the conventional geometric mechanism of the laser tool setters hypothesizes the ideal situation, such as the measuring rod is a perfect cylinder, the axes of the spindle and the cutter being concentric, and perfect alignment between the laser axis and the machine coordinate system, in gauging the laser axis location and the cutter size. This geometric mechanism includes (a) when the measuring rod blocks the laser beam by 50%, the shaded area generated by the rod blocking the laser beam is half of the circular area of the laser beam projection on the photodiode, the Z-coordinate of the laser axis reference point in the machine coordinate system is determined; and (b) when a cutter blocks the laser beam by 50%, the shaded area generated by the cutter blocking the laser beam is half of the circular area of the laser beam projection on the photodiode, the cutter length is determined. Unfortunately, in practice, the conventional geometric mechanism cannot accurately determine the coordinates of the laser

axis reference point and the cutters' sizes, for example, the tool setters' low accuracy (larger than ±0.02 mm) and long time (longer than 90 seconds) in tool setting. Therefore, many laser tool setters are seldom used by machinists.

The ideal situation assumed in the conventional geometric mechanism is unrealistic and different from the practical situation. The practical situation refers to the average-quality end measuring rod, the concentric error between the axis of the spindle and that of the cutter, misalignment of the laser beam, the coordinate error of the laser axis reference point, irregular shapes of the worn cutters, and long measuring time, etc. Thus, the geometric mechanism in the practical situation should be developed. Few people have investigated the geometric mechanism in the practical situation, and there is not any technical article about the geometric mechanism. Since the geometric mechanism significantly affects the accuracy of tool setting, it is necessary to investigate the geometric mechanism in the practical situation.

This section takes the initiative to investigate the geometric mechanism of determining the Z-coordinate of the laser axis reference point in the practical situation. In this work, first, literature about on-machine tool setting is reviewed. Second, a new mechanism for gauging laser axis reference point is developed, and an approach to calculating the rod origin in the tool setter coordinate system is proposed. Then, an applied mathematical model of calculating the area of the shaded region on the receiver screen is established. The model will be applied to the newly proposed calibration process for determining the coordinates of the laser axis reference point in

the machine coordinate system. Finally, this mathematical model and the calibration methods are verified with computer simulations and experiments.

2.2 Comprehensive review on literature about on-machine tool setting

Laser tool setters have been used in the industry for several years. A laser tool setter consists of a transmitter and a receiver [9, 53, 54], each has a micro-hole, and they are aligned. The laser diode in the transmitter emits a laser beam from the micro-hole through the micro-hole in the receiver to the photodiode [55]. Generally, the parallel light source is used, and the laser beam diameter is 0.2 mm. The optical power of the laser is 1 mW, and its wavelength is 670 nm. Several companies (such as Renishaw, Hexagon, and Heidenhain) produce laser tool setters, and they focus on the receiver photodiode quality and the micro-hole design. The designs of the micro holes were patented; airflow is continuously ejecting with speed over 250 m/s from the micro holes to prevent moisture from coming inside, and the micro-hole in the transmitter narrows the laser beam. Thus, this laser beam is very concentrated with high intensity, and it is insusceptible to random environmental influence [55]. The lab test results conducted by Renishaw [56] and many other lab test results [53, 54] demonstrated that their laser tool setters were very reliable with $\pm 1 \mu m$ repeatability. Renishaw's patents [57, 65] disclosed the measuring mechanism of Renishaw laser tool setters. A photodiode in the receiver detects the intensity of the laser beam. In measuring, when a tool blocks the laser beam, the laser intensity on the photodiode drops, and the amount of drop is monitored with a circuit. The circuit samples the photodiode voltage at a rate higher than 96 KHz. An algorithm continuously running in the circuit identifies the

pattern of voltage drop, which enables the laser tool setter to reject erroneous laser blocking by coolant droplets or debris. At the moment the laser intensity drops 50% of the original laser intensity, the photodiode voltage increases to the threshold, and the circuit immediately sends a signal to the machine control. Park *et al*. [58] studied a photodiode property. When an object occludes the laser beam, the laser intensity on the photodiode is inverse proportional to the ratio of the shaded area over the original laser area on the photodiode. The laser diffraction could slightly influence the laser intensity on the photodiode by 5%. In addition, the photodiode voltage is linearly related to its laser intensity. Lee *et al*. [59] developed a laser micro-tool setter based on the laser Fresnel diffraction. Their research studied the relationship among the photodiode laser intensity, the photodiode voltage, and the micro-tool shadow on the photodiode. They found that the laser intensity reduction due to the laser diffraction could be neglected when the tool was significantly larger than the laser beam and the photodiode voltage was linearly related to the laser intensity. If the tool diameter was less than 1 mm, this relationship was not linear, and the nonlinearity increased as the tool diameter decreased.

Conventional thought is that the hardware of laser tool setters determines accuracy and precision, while the real measuring situations do not affect them. Up to now, little research has been conducted and published on how the real measuring situations affect accuracy. Renishaw [66] assumed the ideal measuring situations: (a) the geometric shapes of the end measuring rod and the tools are cylinders and (b) the laser tool setter is perfectly aligned. Then, Renishaw noticed that this assumption could cause tool measurement error, and Renishaw [56] and Lee *et*

al. [63] calculated tool measurement error due to misalignment of a laser tool setter. Unfortunately, they did not consider the geometric errors of the tools, the end measuring rod, and their concentricity about the spindle axis. Li *et al*. [60, 67] established the geometric model of rotating tools with the spindle runout and predicted the mechanics of cutting with the tools. In practice, an end measuring rod or a tool has a rounded edge at the bottom. Hoffmann and Hopcroft [68] modeled the fillet surface of the edge with implicit equations. They generated a fillet surface by sweeping a family of curves. Chiyokura [69] proposed a method of blending polyhedron surfaces. Choi and Ju [70] used the rolling ball method to model a fillet surface of a rounded edge. They constructed a blending surface by sweeping rational quadratic curves along the intersections of the offset surfaces of parametric, rectangular patches. Their method is effective for constructing blending surfaces.

The measuring mechanism that a tool or an end measuring rod blocking the laser beam and forming a shaded region on the photodiode can be represented geometrically by projecting the tool along the laser direction onto the photodiode. The literature about calculating the object projection and the boundary and the area of the projection region is reviewed here. Tokuyama and Bae [71] and Elber [72] proposed methods of computing the silhouette curve of an object along a projection direction. Tokuyama and Bae [71] defined the isocline curves of a surface with a draft angle, and Elber [72] specified that when the draft angle was zero, the isocline curves became a silhouette curve. Some silhouette curves are highly nonlinear and should be represented with advanced methods. To display algebraic curves, Arnon [73] employed the

cylindrical, algebraic decomposition algorithm to determine the topological structure of an algebraic curve. Sutcliffe [74] traced the curve in a region by connecting the positive and negative values of the curve function with lines. Chandler [75] proposed a pixel-based curve tracing algorithm without calculating partial derivatives of the curve. Tokuyama and Bae [71] proposed a curve tracing algorithm by computing points on a silhouette curve with the gradient methods.

To find the boundary of an object's normal projection region on a plane, the homogeneous transformations for points on the silhouette curves of the object were derived in [76]. The boundaries of the shade regions could intersect with each other. Sutherland and Hodgman [77], Vatti [78], and Greiner and Hormann [79] proposed three polygon clipping methods. In Sutherland and Hodgman's [77] method, the clip polygon is traversed, and each side of the clip polygon is extended infinitely. Tests for the vertices of the subject polygon to the extended line are carried out, and only those vertices on the visible side of the subject polygon are kept. Their methods are suitable for convex polygons. Vatti's [78] rendered a scanline method to handle concave polygons; however, it is complicated [79]. Greiner and Hormann [79] simplified the process of finding polygon intersections. Their method gathers the portions of sides of each polygon lying inside the other polygon. This method outperforms Vatti's method and can handle concave polygons. However, it fails in degenerate cases. These techniques are needed to test if the projected end measuring rod intersects with the laser beam cross-section. Besides, a paper about computing the area of a region with a polygon boundary is reviewed. Beyer [80]

documented the expression for calculating the area of a closed polygon without holes and self-intersection, given its vertices along the contour.

Studies have shown that the laser tool setters suffer from several error sources in practical application, including their installation misalignment and tool geometric difference. Other sources include the low-quality measuring rods, the machine spindle run-out [60, 61], and the spindle speed and the feed rate [56]. Unfortunately, these error sources are ignored by the current applications of non-contact laser tool setter [62]. Milton *et al*. [64] designed a set of experiments based on statistical analyses to identify the best feed rate and spindle speed for referencing laser tool-setters. Their method is experimentally based and does not calculate the measurement error due to the error sources. Unfortunately, there is no research on a completed tool setting model using laser tool setters.

2.3 Development of new mechanism of determining z-coordinate of laser axis reference point in practical situations

2.3.1 Introduction to the conventional mechanism of gauging with laser tool setter in ideal situations

The conventional mechanism of gauging with laser tool setter is based on a premise that its setup and the gauging process are in the ideal situation. First, a laser tool setter is set up on a

CNC machining center in the ideal situation, which is shown in Figure 2.2. The machine coordinate system ($\mathbf{X}_m\mathbf{Y}_m\mathbf{Z}_m\mathbf{O}_m$, m for machine) is illustrated in this figure (not at the correct location). The transmitter emits a laser beam to the photodiode inside the receiver, generating a red circular region on the photodiode. According to the specification of the laser tool setter, the laser beam diameter is 0.2 mm. So, the diameter of the red circular region of the laser beam projection is 0.2 mm. The axis of the laser beam is perfectly aligned with the $\mathbf{X}_m$-axis (in special cases, the laser beam can be installed to align with the $\mathbf{Y}_m$-axis).

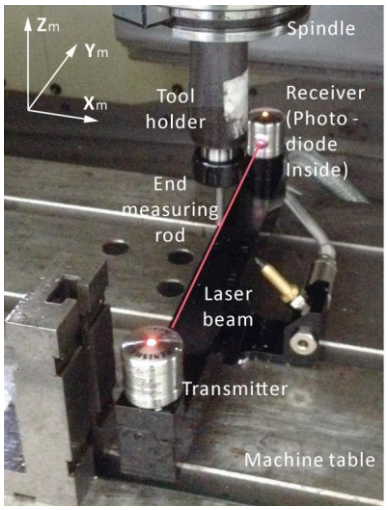

Figure 2.2 A laser tool setter is perfectly set up on a CNC machining center.

Second, the gauging process is in the ideal situation (see Figure 2.3(a)). The end measuring rod is in the shape of a true cylinder. Its length L_r refers to the distance between the spindle

reference point and the rod (bottom) center, which is gauged on a tool presetter. The measuring rod is clamped in the machine spindle and the machine spindle does not rotate in measurement.

(a)

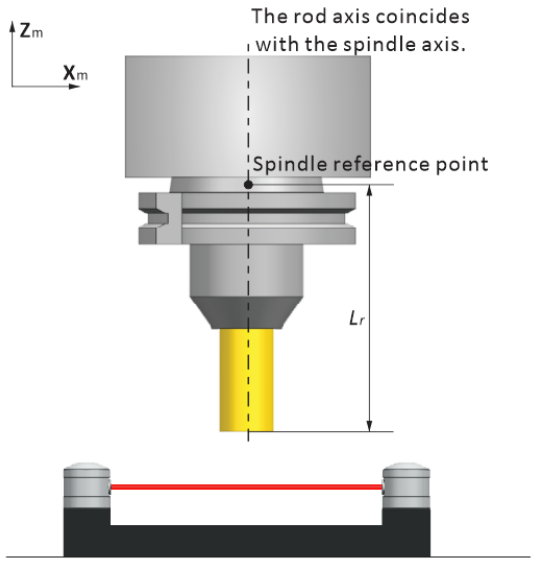

(b)

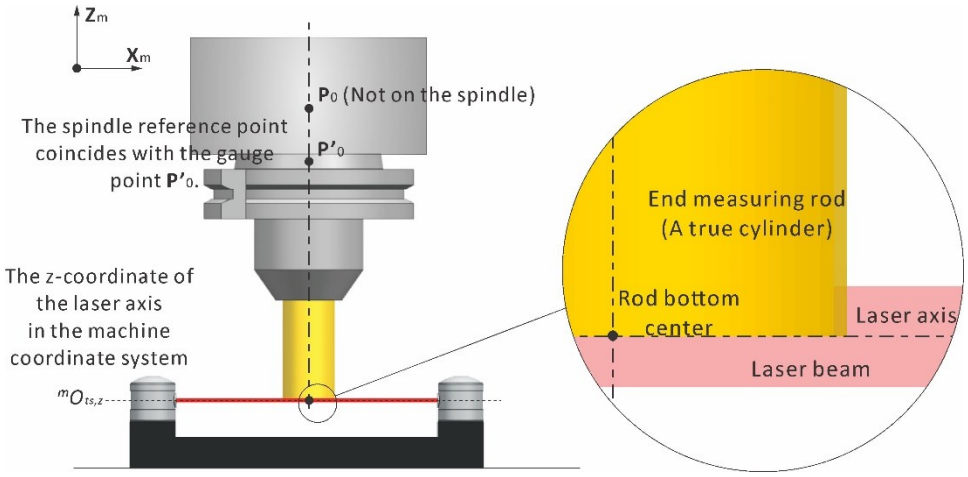

(c)

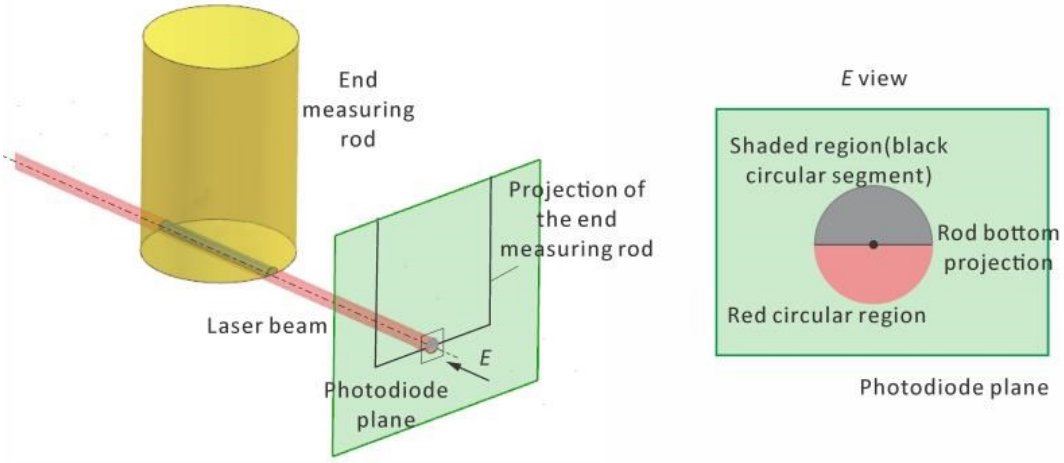

Figure 2.3. (a) The spindle reference point is at an origin of measurement, (b) the conventional method of gauging the Z-coordinate of the laser axis reference point with the measuring rod in the ideal situation, and (c) the conventional mechanism of gauging with laser tool setter.

Then, the conventional mechanism of gauging the Z-coordinate of the laser axis reference point $\mathbf{O}_{ts}\left[{}^{m}O_{ts,x}, {}^{m}O_{ts,y}, {}^{m}O_{ts,z}\right]^{T}$ in the machine coordinate system (see Figure 2.3(b)). Here, two terms are defined. A laser axis reference point is defined as a point on the laser axis and near its midpoint, at which position and orientation of the laser beam axis are gauged and represented (see Figure 2.3(b)). Origin of measurement is defined as a position for the spindle reference point. When the spindle reference point reaches an origin of the measurement, the measuring rod is near the laser beam, and the measuring rod starts to gauge the laser axis. In Figure 2.3(b), the origin of measurement $\mathbf{P}_0$ is planned to be right above the laser axis reference point, and its

coordinates in the machine coordinate system are denoted as $\mathbf{P}_0\left[{}^{m}\mathrm{P}_{0,x}, {}^{m}\mathrm{P}_{0,y}, {}^{m}\mathrm{P}_{0,z}\right]^T$ (m for the machine coordinate system).

The gauging process includes the following four steps. (1) The machine spindle moves quickly so its reference point reaches the origin of measurement $\mathbf{P}_0$. (2) The measuring rod moves slowly along the negative $\mathbf{Z}_m$-axis towards the laser beam, blocking the laser beam from the receiver and forming a shaded (black) region inside the red circular region on the photodiode (see Figure 2.3(c)). The shaded region refers to the black circular segment of the red circular region split with a secant of the rod bottom projection. The shaded region of the rod projection is regular. The laser intensity on the photodiode is gradually reduced. (3) When the laser beam is blocked by 50%, the shaded area – the black circular segment – becomes half of the red circular area, and the spindle reference point reaches a point (see Figure 2.3(c)). Here, it is called a gauge point $\mathbf{P}_0'$ (the apostrophe means gauge point). At this moment, the laser intensity drops below the threshold of the photodiode, the photodiode generates a large voltage to trigger its circuit sending a signal to the machine control[53-55, 66], and the coordinates of the spindle reference point in the machine coordinate system are immediately recorded by the machine control, which is coordinates of $\mathbf{P}_0'\left[{}^{m}\mathrm{P}'_{0,x} \quad {}^{m}\mathrm{P}'_{0,y} \quad {}^{m}\mathrm{P}'_{0,z}\right]^T$. (4) The z-coordinate of the laser axis reference point in the machine coordinate system is determined as

$$ {}^{m}O_{ts,z} = {}^{m}\mathrm{P}'_{0,z} - L_r \tag{2.1}$$

This is the conventional mechanism of gauging with a laser tool setter in the ideal measuring situation.

Finally, the conventional method of gauging tool length in the ideal situation is explained (see Figure 2.4). In the ideal situation, any tool is in the shape of a perfect cylinder and is clamped in the machine spindle concentrically. In gauging, the tool rotates about the machine spindle axis. Similarly, the machine spindle moves quickly to a planned origin of measurement $\mathbf{T}_0$ (T for tool), then moves slowly along the negative $\mathbf{Z}_m$-axis towards the laser beam. When the tool blocks the laser beam, the shaded region of a circular segment is formed in the red circular region on the photodiode. When the tool blocks the laser beam by 50%, the area of the shaded region – the black circular segment – is half of the red circular area (see Figure 2.4). At the same time, the spindle reference point is at the gauge point $\mathbf{T}_0'$, and the coordinates of the spindle reference point in the machine coordinate system are recorded as the coordinates of $\mathbf{T}_0'$ $\begin{bmatrix} {}^m\mathrm{T}'_{0,x} & {}^m\mathrm{T}'_{0,y} & {}^m\mathrm{T}'_{0,z} \end{bmatrix}^T$. The tool length L_t (t for tool) is determined by

$$L_t = {}^m\mathrm{T}'_{0,z} - {}^mO_{ts,z} \tag{2.2}$$

It is evident that the accuracy of the z-coordinate of the laser axis reference affects the accuracy of the tool length.

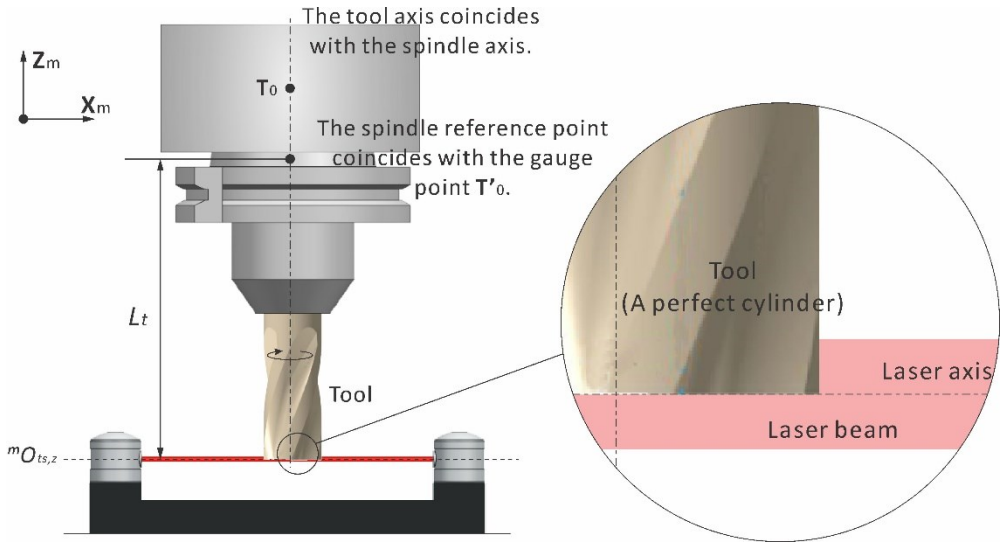

Figure 2.4. The tool length is measured on a laser tool setter in the ideal situation.

2.3.2 Analysis of the practical situation of laser tool setters, end measuring rods, and tools

In machine shops, the ideal situation of laser tool setters, end measuring rods, and tools does not exist, while the practical situation is quite different. Therefore, a new mechanism has to consider the practical situation, which is explained as follows.

First, misalignment of a laser tool setter cannot be eliminated in its calibration, especially for a separated system of the laser tool setter. When the transmitter and the receiver are set up on the machine, it is very difficult to adjust the transmitter and the receiver so that the laser axis is aligned to the $\mathbf{X}_m$ -axis. This misalignment cannot be eliminated in practice. In this work, the angle between the projections of the laser axis on a horizontal plane and the $\mathbf{X}_m$ - axis is called yaw angle α , and the angle between the laser axis and a horizontal plane is called pitch angle β

(see Figure 2.5). Because of its misalignment, the laser axis is not perpendicular to the axis of the measuring rod, so the calculation of the rod projection along the laser axis is complicated. The new mechanism should be investigated by considering this misalignment.

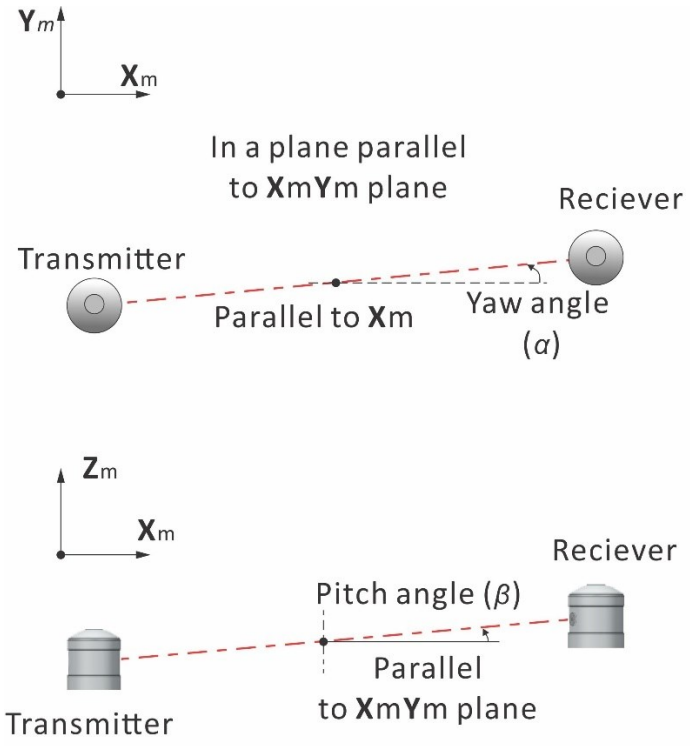

Figure 2.5. Definition of the pitch and the yaw angles of the laser axis.

Second, the practical situation of the end measuring rod is the main source of the Z-coordinate error of the laser axis reference point. The conventional mechanism assumes that the end measuring rod is in the shape of a perfect cylinder. However, the rod flank surface is a cylinder, the rod bottom plane could be oblique to the rod axis, and the rounded edge is a fillet surface between the flank and the bottom (see Figure 2.6). The actual shape of the end measuring rod determines the shaded region of the rod projection, which cannot be ignored in the new mechanism.

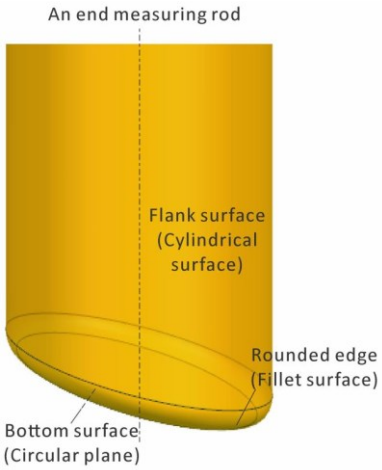

Figure 2.6. The geometric shape of an actual end measuring rod includes a cylindrical surface, a bottom plane, and a fillet surface.

2.3.3 Establishing a new geometric mechanism of gauging in practical situations

The conventional mechanism mentioned in the Section 2.3.1 cannot precisely represent the geometric natures of gauging with laser tool setter in the practical situation. One of the geometric natures is that the shaded region, inside the red circular region on the photodiode, is irregular with a curve border; while the conventional mechanism hypothesizes that the shaded region is a regular circular segment (see Figure 2.3(c)). Another geometric nature is when the area of the shaded region is half of the red circular area, the rod bottom center, and the laser axis reference point do not share the same Z-coordinate; while the conventional mechanism assumes the rod bottom center and the laser axis reference point share the same z-coordinate (see Figure 2.3). Therefore, the area of the shaded region and Z-coordinate difference between the rod bottom center and the laser axis reference point should be calculated. In this section, a new geometric mechanism of gauging with laser tool setter in the practical situation is developed.

Based on this mechanism, an accurate approach to calculating the Z-coordinate of the rod bottom center in the tool setter coordinate system is proposed in this paper. With this information, the Z-coordinate of the laser axis reference point can be accurately determined in the machine coordinate system using kinematics chains which are described in Section 5. To establish a new geometric mechanism of gauging with laser tool setter in the practical situation, precise mathematical models of the laser beam and the measuring rod should be established in a virtual gauging configuration. This configuration truly represents the geometries of the laser beam and the rod and their relative positions, so the gauging process can be simulated using a mathematical method.

The construction work includes the following three steps. First, a tool setter coordinate system ($\mathbf{X}_{ts}\mathbf{Y}_{ts}\mathbf{Z}_{ts}\mathbf{O}_{ts}$, ts for tool setter) is established, and the laser beam geometry is modeled. The origin $\mathbf{O}_{ts}$ of the tool setter coordinate system is set at the laser axis reference point. The $\mathbf{X}_{ts}$ -, $\mathbf{Y}_{ts}$ - and $\mathbf{Z}_{ts}$ -axes are parallel to the $\mathbf{X}_{m}$ -, $\mathbf{Y}_{m}$ - and $\mathbf{Z}_{m}$ -axes, respectively (see Figure 2.7). In the laser tool setter calibration, the pitch β and the yaw α angles of the laser axis are known. Thus, the geometric model of the laser beam is constructed in the tool setter coordinate system, shown in Figure 2.7.

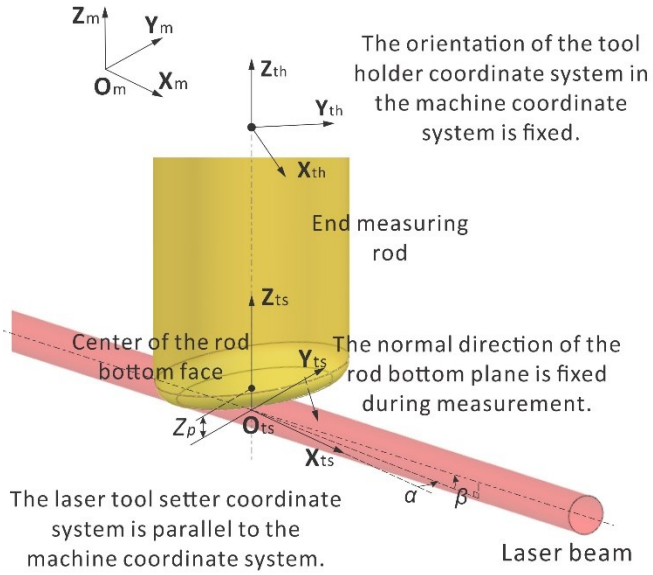

Figure 2.7 In the virtual gauging configuration, the actual laser beam and the actual measuring rod are modeled according to the practical situation.

Second, the actual measuring rod is modeled. The geometry of the actual measuring rod consists of a cylinder, a rounded edge, and a bottom plane. To obtain the rod geometry, the rod is tightened in a collet chuck tool holder and is gauged with a presetter (see Figure 2.8) and a coordinate measurement machine (CMM). On the tool presetter, the tool holder coordinate system is established. Then, the radius of the rod flank cylinder, the radius of the rounded edge, and the maximum length of the rod are measured. The rod bottom plane including the rod bottom center and its normal vector is measured and computed using a CMM. The maximum length of the rod is measured on the CMM again to convert the bottom plane geometries to the tool holder coordinate system ($\mathbf{X}_{th}\mathbf{Y}_{th}\mathbf{Z}_{th}\mathbf{O}_{th}$, th for tool holder). Now, it is important to place the rod geometric model in the virtual gauging configuration. Since the machine spindle does not

rotate in measurement, the measuring rod preserves its orientation with regard to the laser beam (see Figure 2.9). The normal direction of the rod bottom plane remains the same during measurement. Based on the position relationships among the tool holder, the machine, and the tool setter coordinate systems, the rod geometric model can be transformed in the tool setter coordinate system (see Figure 2.7).

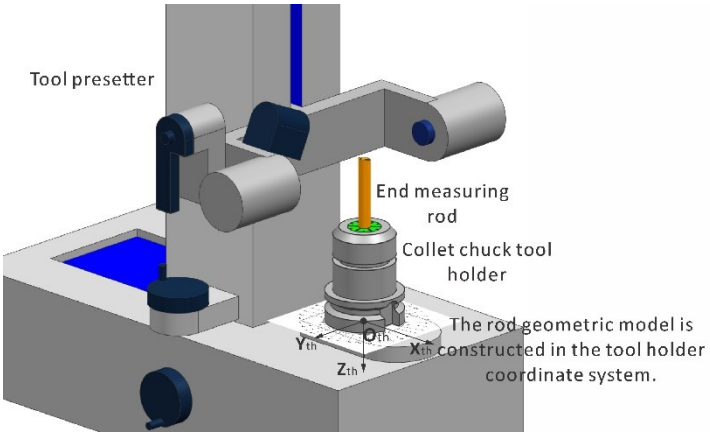

Figure 2.8 The end measuring rod clamped in the collet chuck tool holder is measured on the offline tool presetter in the tool-holder coordinate system.

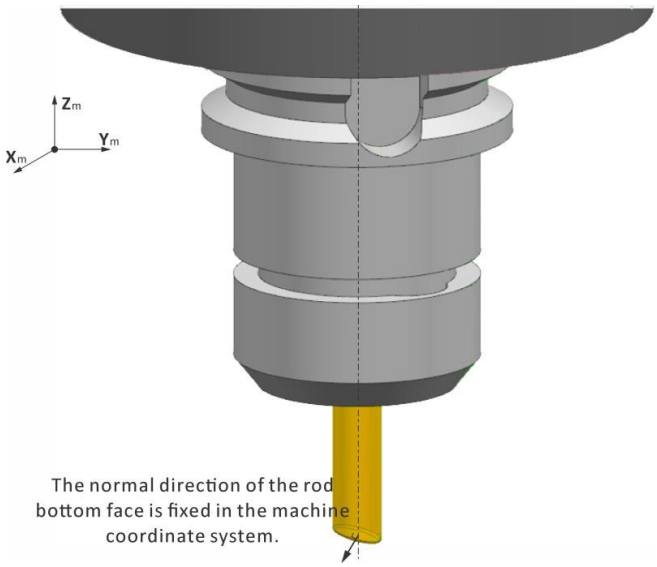

Figure 2.9 The geometry model of the end measuring rod mounted in the spindle in the virtual gauging configuration.

Third, this configuration is based on the tool setter coordinate system and the laser beam model. The actual measuring rod model is placed on the origin of measurement with the correct orientation. Therefore, the virtual gauging configuration is completed (see Figure 2.9).

Based on the virtual gauging configuration, a new geometric mechanism of gauging the z-coordinate of the laser axis reference point in the practical situation is explained here. From the origin of measurement, the rod is fed slowly towards the laser beam, blocking the laser beam from the receiver and forming a shaded black region on the photodiode. This shaded region is generated by the rod projection and is inside the red circular region of the laser beam projection;

the shaded region and the circular region are split by a curve of the rod bottom projection. It is important to know that the shaded region is irregular in the new mechanism, while the shaded region is regular in the conventional mechanism. The laser intensity on the photodiode is gradually reduced. When the spindle reference point reaches the gauging point and the rod blocks the laser beam by 50%, the area of the shaded region is half of the red circular area, and the shaded region is split by a curve with the red circular region (see Figure 2.3(c)). At this moment, the laser intensity is equal to the threshold of the photodiode, and the receiver circuit is triggered sending a signal to the machine control, and the coordinates of the gauge point in the machine coordinate system are immediately recorded by the CNC control (see Figure 2.3(a)). Since the shaded region is irregular at this moment, the z-coordinates of the rod bottom center and the laser axis reference point are not the same (see Figure 2.10). As a result, the z-coordinate of the laser axis reference point cannot be determined. Therefore, it is necessary to calculate the difference of the z-coordinates between the rod bottom center and the laser axis reference point, when the spindle reaches the gauge point in the computer gauging simulation, in order to determine the z-coordinate of the laser axis reference point.

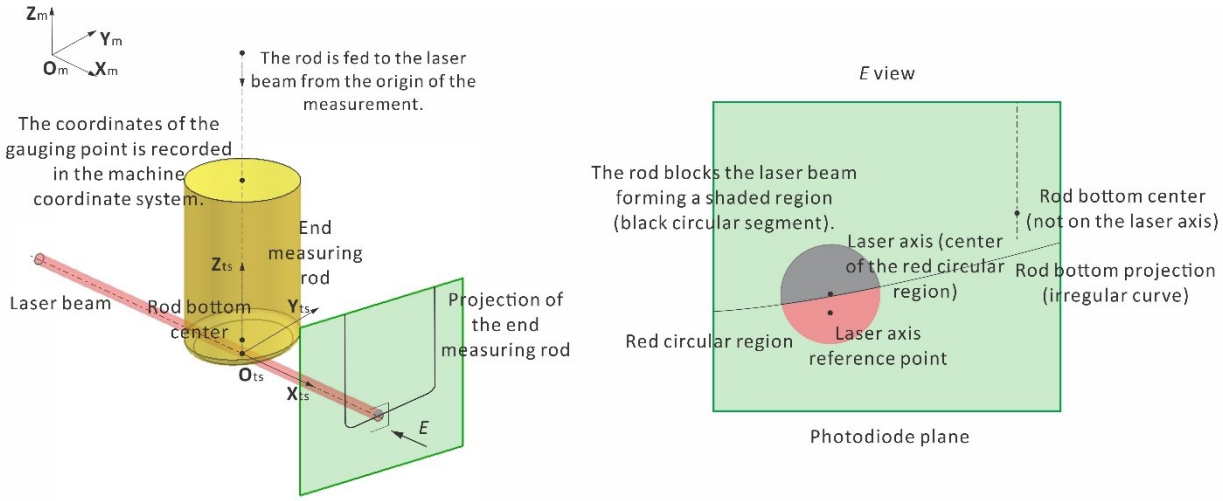

Figure 2.10 In the practical situation, the rod blocks the laser beam forming an irregular shaded region in the red circular region.

2.3.4 Proposing a new approach for computer simulation with virtual gauging configuration

Based on the above-mentioned geometric mechanism and the virtual gauging configuration, a new approach for computer gauging simulation is proposed. The objective of the simulation is to compute the z-coordinate of the rod bottom center in the tool setter coordinate system when the spindle reaches the gauge point. The simulation process is as follows. The rod starts from the origin of measurement and moves down to the laser beam. By using the Golden section method, each step in the gauging path is calculated. At each step, the area of the shaded region is calculated. If the area is null, the rod does not block the laser beam. A large step is followed. If the area is not null but less than half of the area of the red circular region, the rod blocks the

laser beam. However, the spindle does not reach the gauge point. Through iteration of computation, the gauge point could be determined, and the area of the shaded region is a half of the red circular region. The z-coordinate of the rod bottom center in the tool setter coordinate system is calculated. In this approach, the kernel technique is to calculate the boundary and the area of the shaded black region of the rod projection. Due to the complex geometric shape of the rod and misalignment of the laser axis, the conventional method cannot accurately calculate the shaded region. A new mathematical model of calculating the shaded region in the practical situation is proposed in the next section.

2.4 New and accurate mathematical model of calculating shaded region in practical situations

2.4.1 Mathematical representation of end measuring rod geometry in the tool holder coordinate system

The end measuring rod is clamped on a tool holder and based on the geometric model of the end measuring rod in the virtual measuring configuration, the geometric representation of the end measuring rod in the tool holder coordinate system can be formulated. The geometry and dimension notations of an end measuring rod are introduced in Figure 2.11. First, the tool holder coordinate system $\mathbf{X}_{th}\mathbf{Y}_{th}\mathbf{Z}_{th}\mathbf{O}_{th}$ is established on the tool holder reference center $\mathbf{O}_{th}$. The $\mathbf{X}_{th}$ -

axis is along the center of the tool holder keyway. The $\mathbf{Z}_{th}$ - axis is along the tool holder axis. The $\mathbf{Y}_r$ -axis is defined by the right-hand rule. The rod geometry is expressed in $\mathbf{X}_{th}\mathbf{Y}_{th}\mathbf{Z}_{th}\mathbf{O}_{th}$ and it includes a cylindrical surface $\mathbf{F}_c$ (c for cylindrical), a fillet (or chamfer) surface $\mathbf{F}_f$ (f for fillet), and a bottom plane $\mathbf{F}_b$ (b for bottom). The distance between the rod bottom plane center $\mathbf{O}_r$ (r for rod) and $\mathbf{O}_{th}$ is L_r. $\mathbf{O}_r$ is on the tool holder axis. The radius of the rod flank is R_r (r for rod). The unit vector $\mathbf{n}_b$ (b for bottom) is the normal of the bottom face in the tool holder coordinate system. The cylindrical surface $\mathbf{F}_c$ and the bottom plane $\mathbf{F}_b$ are connected with a fillet surface $\mathbf{F}_f$. The corner radius of the fillet surface is R_f (f for fillet).

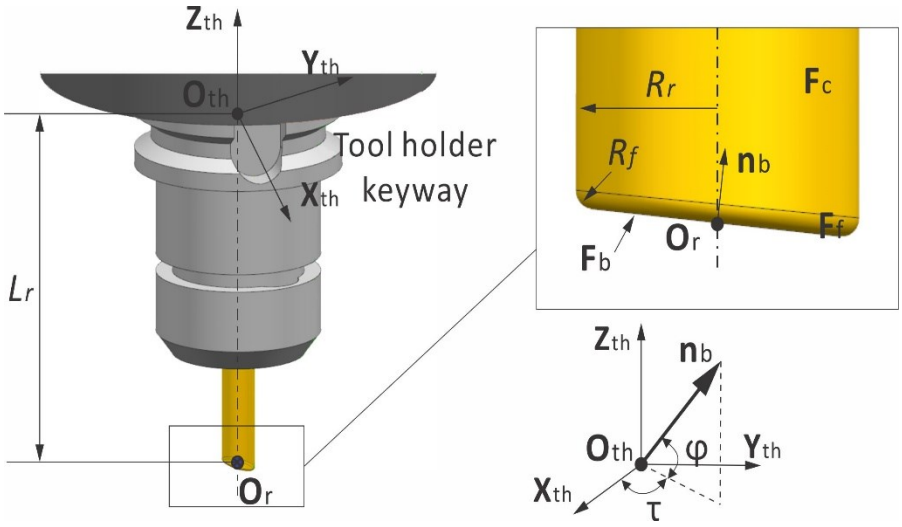

Figure 2.11. Illustration of an end measuring rod and the tool holder coordinate system $\mathbf{X}_{th}\mathbf{Y}_{th}\mathbf{Z}_{th}\mathbf{O}_{th}$.

The parametric equations of the rod's surfaces are derived here. In $\mathbf{X}_{th}\mathbf{Y}_{th}\mathbf{Z}_{th}\mathbf{O}_{th}$, we suppose the cylindrical surface $\mathbf{F}_c$ starts from the $\mathbf{X}_{th}\mathbf{Y}_{th}$ plane and it is parametrically represented as $\mathbf{F}_c(h,u)$. $\mathbf{F}_c(h,u)$ in $\mathbf{X}_{th}\mathbf{Y}_{th}\mathbf{Z}_{th}\mathbf{O}_{th}$ can be written as

$$^{th}\mathbf{F}_c(h,u)=\begin{bmatrix} R_r\cdot\cos u \\ R_r\cdot\sin u \\ h \\ 1 \end{bmatrix} \tag{2.3}$$

where $u\in[0,360\deg]$, $h\in[h_l,0]$. h_l is the lower limit of the cylindrical surface $\mathbf{F}_c$. It depends on both the parameter u and the shape of the fillet surface $\mathbf{F}_f$.

In $\mathbf{X}_{th}\mathbf{Y}_{th}\mathbf{Z}_{th}\mathbf{O}_{th}$, the bottom normal vector $\mathbf{n}_b$ can be expressed as

$$^{th}\mathbf{n}_b=\begin{bmatrix} \cos\varphi\cdot\cos\tau \\ \cos\varphi\cdot\sin\tau \\ \sin\varphi \\ 0 \end{bmatrix} \tag{2.4}$$

where φ is the angle between $\mathbf{n}_b$ and its projection on the $\mathbf{X}_{th}\mathbf{Y}_{th}$ plane and τ is the angle between the projection of $\mathbf{n}_b$ on the $\mathbf{X}_{th}\mathbf{Y}_{th}$ plane and the $\mathbf{X}_{th}$ axis. The rod bottom plane $\mathbf{F}_b$ passes through $\mathbf{O}_r$ and $\mathbf{O}_r$ in $\mathbf{X}_{th}\mathbf{Y}_{th}\mathbf{Z}_{th}\mathbf{O}_{th}$ can be written as

$$ {}^{th}\mathbf{O}_r = \begin{bmatrix} 0 \\ 0 \\ -L_r \\ 1 \end{bmatrix} \tag{2.5} $$

The rod bottom plane in $\mathbf{X}_{th}\mathbf{Y}_{th}\mathbf{Z}_{th}\mathbf{O}_{th}$ is

$$ x \cdot \cos\varphi \cdot \cos\tau + y \cdot \cos\varphi \cdot \sin\tau + (z + L_r) \cdot \sin\varphi = 0 \tag{2.6} $$

The fillet surface $\mathbf{F}_f$ is found by sweeping a sphere with the radius of the fillet R_f along a curve. This curve $\mathbf{C}_{in}$ is generated by intersecting the offset cylindrical surface $\mathbf{F}_c$ and the offset bottom plane $\mathbf{F}_b$. The offset amounts for both surfaces are equal R_f. Then, the fillet surface $\mathbf{F}_f$ is generated as a circular edge $\mathbf{C}_{ce}$ (C for curve and ce for circular edge) with a radius R_f sweeping along $\mathbf{C}_{in}$ (see Figure 2.12). $\mathbf{C}_c$ is a rational quadratic curve.

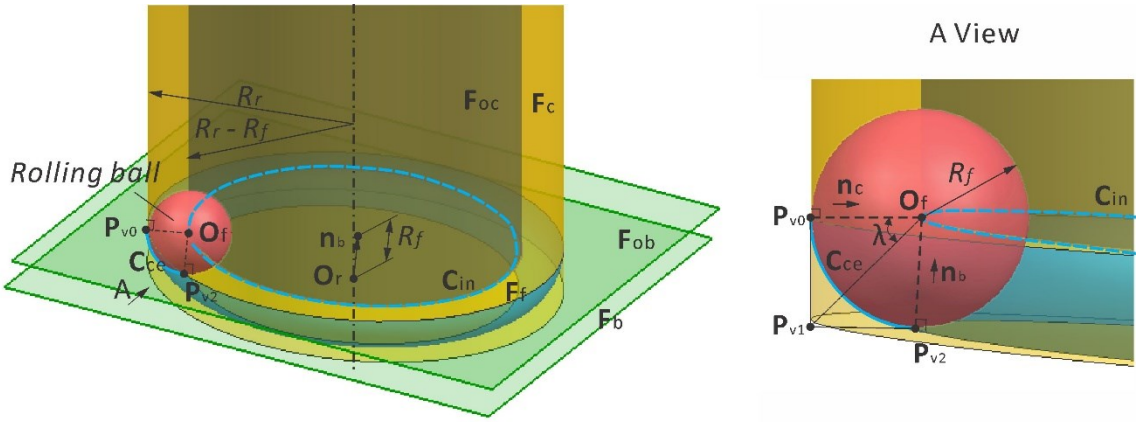

Figure 2.12. Illustration of the modelling of the end measuring rod fillet.

The offset surface of the cylindrical surface $\mathbf{F}_c$ is $\mathbf{F}_{oc}$ (o for offset and c for cylinderical), and

$$ {}^{th}\mathbf{F}_{oc}(h,u)=\begin{bmatrix}(R_r-R_f)\cdot\cos u\\(R_r-R_f)\cdot\sin u\\h\\1\end{bmatrix} \tag{2.7}$$

where $h\in[-\infty,+\infty]$, $u\in[0,360\,\text{deg}]$. The offset surface of the bottom plane $\mathbf{F}_b$, $\mathbf{F}_{ob}$ (o for offset and b for bottom), is

$$(x-R_f\cdot\cos\varphi\cdot\cos\tau)\cdot\cos\tau+(y-R_f\cdot\cos\varphi\cdot\sin\tau)\cdot\sin\tau+(z+L_r-R_f\cdot\sin\varphi)\cdot\tan\varphi=0 \tag{2.8}$$

The intersection curve $\mathbf{C}_{in}$ of $\mathbf{F}_{oc}$ and $\mathbf{F}_{ob}$ in $\mathbf{X}_{th}\mathbf{Y}_{th}\mathbf{Z}_{th}\mathbf{O}_{th}$ is

$$ {}^{th}\mathbf{C}_{in}(u)=\begin{bmatrix}(R_r-R_f)\cdot\cos u\\(R_r-R_f)\cdot\sin u\\R_f\cdot\sin\varphi-L_r-Q_1-Q_2\\1\end{bmatrix} \tag{2.9}$$

where

$$Q_1=\left((R_r-R_f)\cdot\cos u-R_f\cdot\cos\varphi\cdot\cos\tau\right)\cdot\frac{\cos\tau}{\tan\varphi} \tag{2.10}$$

$$Q_2=\left((R_r-R_f)\cdot\sin u-R_f\cdot\cos\varphi\cdot\sin\tau\right)\cdot\frac{\sin\tau}{\tan\varphi} \tag{2.11}$$

and $u \in [0, 360\text{deg}]$. A circular edge $\mathbf{C}_{ce}$ sweeping along this curve generates the fillet surface. $\mathbf{C}_{ce}$ can be modeled by using the rational parametric equation of conic curves, which requires three controlled vertices as input. The followings derive the equation for these three control vertices.

A sphere with a radius R_f is centered at a point $\mathbf{O}_f$ (f for fillet) on the intersection curve $\mathbf{C}_{in}$. The sphere is tangent to both $\mathbf{F}_c$ and $\mathbf{F}_b$ at $\mathbf{P}_{v0}$ and $\mathbf{P}_{v2}$ (v for vertex). These two points are two control vertices of $\mathbf{C}_{ce}$. $\mathbf{P}_{v0}$ in $\mathbf{X}_{th}\mathbf{Y}_{th}\mathbf{Z}_{th}\mathbf{O}_{th}$ is found as

$$ {}^{th}\mathbf{P}_{v0}(u) = \begin{bmatrix} R_r \cdot \cos u \\ R_r \cdot \sin u \\ R_f \cdot \sin\varphi - L_r - Q_1 - Q_2 \\ 1 \end{bmatrix} \tag{2.12} $$

Since $\mathbf{F}_b$ is a plane with a normal unit vector $\mathbf{n}_b$, $\mathbf{P}_{v2}$ in $\mathbf{X}_{th}\mathbf{Y}_{th}\mathbf{Z}_{th}\mathbf{O}_{th}$ is found as

$$ \begin{aligned} {}^{th}\mathbf{P}_{v2}(u) &= {}^{th}\mathbf{O}_f(u) - R_f \cdot {}^{th}\mathbf{n}_b \\ &= \begin{bmatrix} (R_r - R_f)\cdot\cos u - R_f \cdot \cos\varphi \cdot \cos\tau \\ (R_r - R_f)\cdot\sin u - R_f \cdot \cos\varphi \cdot \sin\tau \\ -L_r - Q_1 - Q_2 \\ 1 \end{bmatrix} \end{aligned} \tag{2.13} $$

Construct a tangent plane to $\mathbf{F}_c$ at $\mathbf{P}_{v0}$ and this plane will intersect $\mathbf{F}_b$, resulting in a line. A plane defined by $\mathbf{O}_f$, $\mathbf{P}_{v0}$ and $\mathbf{P}_{v2}$ will intersect the previous line at $\mathbf{P}_{v1}$, which can be found in $\mathbf{X}_{th}\mathbf{Y}_{th}\mathbf{Z}_{th}\mathbf{O}_{th}$ by

$$ {}^{\text{th}}\mathbf{P}_{\text{v1}}(u)=\frac{1}{2}\cdot\left[{}^{\text{th}}\mathbf{P}_{\text{v0}}(u)+{}^{\text{th}}\mathbf{P}_{\text{v2}}(u)\right]+\frac{1}{2}\cdot R_f\cdot\left(\frac{{}^{\text{th}}\mathbf{n}_{\text{c}}\cdot{}^{\text{th}}\mathbf{n}_{\text{b}}-1}{{}^{\text{th}}\mathbf{n}_{\text{c}}\cdot{}^{\text{th}}\mathbf{n}_{\text{b}}+1}\right)\cdot\left({}^{\text{th}}\mathbf{n}_{\text{c}}+{}^{\text{th}}\mathbf{n}_{\text{b}}\right) \tag{2.14} $$

vwhere $\mathbf{n}_{\text{c}}$ (c for cylinderical) is the unit normal vector of $\mathbf{F}_{\text{c}}$ at $\mathbf{P}_{\text{v0}}$. $\mathbf{n}_{\text{c}}$ in $\mathbf{X}_{\text{th}}\mathbf{Y}_{\text{th}}\mathbf{Z}_{\text{th}}\mathbf{O}_{\text{th}}$ is found by

$$ {}^{th}\mathbf{n}_{\text{c}}=-\begin{bmatrix}\cos u\\ \sin u\\ 0\\ 0\end{bmatrix} \tag{2.15} $$

$\mathbf{P}_{\text{v0}}$, $\mathbf{P}_{\text{v1}}$ and $\mathbf{P}_{\text{v2}}$ are functions of the parameter u, where $u\in[0,360\text{deg}]$ and these three points are used as the controlled vertices of the rational parametric equation of a quadratic curve $\mathbf{C}_{\text{ce}}$. When $\mathbf{C}_{\text{ce}}$ is an arc with a radius R_f connecting $\mathbf{P}_{\text{v0}}$ and $\mathbf{P}_{\text{v2}}$ centering at $\mathbf{O}_{\text{f}}$, its equation in $\mathbf{X}_{\text{th}}\mathbf{Y}_{\text{th}}\mathbf{Z}_{\text{th}}\mathbf{O}_{\text{th}}$ is

$$ {}^{\text{th}}\mathbf{C}_{\text{ce}}(v)=\frac{(1-v)^2\cdot{}^{\text{th}}\mathbf{P}_{\text{v0}}+2\cdot\cos(\lambda(u))\cdot(1-v)\cdot v\cdot{}^{\text{th}}\mathbf{P}_{\text{v1}}+v^2\cdot{}^{\text{th}}\mathbf{P}_{\text{v2}}}{(1-v)^2+2\cdot\cos(\lambda(u))\cdot(1-v)\cdot v+v^2} \tag{2.16} $$

where $v\in[0,1]$, $\lambda(u)=\dfrac{\cos^{-1}\left({}^{\text{th}}\mathbf{n}_{\text{c}}\cdot{}^{\text{th}}\mathbf{n}_{\text{b}}\right)}{2}$ and $\lambda(u)$ is a function of the parameter u. By sweeping $\mathbf{C}_{\text{ce}}$ along $\mathbf{C}_{\text{in}}$, we can find the fillet face $\mathbf{F}_{\text{f}}$ in $\mathbf{X}_{\text{th}}\mathbf{Y}_{\text{th}}\mathbf{Z}_{\text{th}}\mathbf{O}_{\text{th}}$ as

$$ {}^{\text{th}}\mathbf{F}_{\text{f}}(u,v)=\frac{(1-v)^2\cdot{}^{\text{th}}\mathbf{P}_{\text{v0}}(u)+2\cdot\cos(\lambda(u))\cdot(1-v)\cdot v\cdot{}^{\text{th}}\mathbf{P}_{\text{v1}}(u)+v^2\cdot{}^{\text{th}}\mathbf{P}_{\text{v2}}(u)}{(1-v)^2+2\cdot\cos(\lambda(u))\cdot(1-v)\cdot v+v^2} \tag{2.17} $$

where $v\in[0,1]$ and $u\in[0,360\text{deg}]$.

Finally, the lower limit boundary of the cylindrical surface $\mathbf{F}_c$ is the locus of $\mathbf{P}_{v0}$ when $\mathbf{C}_{ce}$ is sweeping along $\mathbf{C}_{in}$ and thus the cylindrical surface $\mathbf{F}_c(h,u)$ in $\mathbf{X}_{th}\mathbf{Y}_{th}\mathbf{Z}_{th}\mathbf{O}_{th}$ is

$$^{th}\mathbf{F}_c(h,u)=\begin{bmatrix} R_r\cdot\cos u \\ R_r\cdot\sin u \\ h \\ 1 \end{bmatrix} \tag{2.18}$$

where $u\in[0,360\text{deg}]$, $h\in[h_l,0]$ and $h_l=R_f\cdot\sin\varphi-L_r-Q_1-Q_2$.

2.4.2 Mathematical representation of end measuring rod in tool-setter coordinate system

By using the position relationships among the tool holder, the machine, and the tool setter coordinate systems, the end measuring rod can be represented in the tool setter coordinate system. The tool holder is clamped on the spindle. The tool holder reference point and the spindle reference coincide. The tool holder axis also coincides with the spindle axis, which is parallel to the machine $\mathbf{Z}_m$ axis. The coordinates of $\mathbf{O}_{th}$ in the machine coordinate system represent the spindle location.

In measurement, the spindle orientation is maintained at all times, and $\mathbf{X}_{th}$ - axis forms a tool holder angle θ_{th} (th for tool holder) with the machine coordinate system $\mathbf{X}_m$ - axis (see Fig.14). Since the tool setter coordinate system is parallel to the machine coordinate system, $\mathbf{X}_{th}$ - axis also forms an angle θ_{th} with the $\mathbf{X}_{ts}$ - axis. At any moment, the distance along the spindle axis

between the rod bottom center $\mathbf{O}_r$ and the laser axis reference point $\mathbf{O}_{ts}$ is Z_d (d for distance). The transformation matrix from $\mathbf{X}_{th}\mathbf{Y}_{th}\mathbf{Z}_{th}\mathbf{O}_{th}$ to $\mathbf{X}_{ts}\mathbf{Y}_{ts}\mathbf{Z}_{ts}\mathbf{O}_{ts}$ is

$$ {}^{ts}\mathbf{M}_{th} = \begin{bmatrix} \cos\theta_{th} & -\sin\theta_{th} & 0 & 0 \\ \sin\theta_{th} & \cos\theta_{th} & 0 & 0 \\ 0 & 0 & 1 & L_r + Z_d \\ 0 & 0 & 0 & 1 \end{bmatrix} \tag{2.19} $$

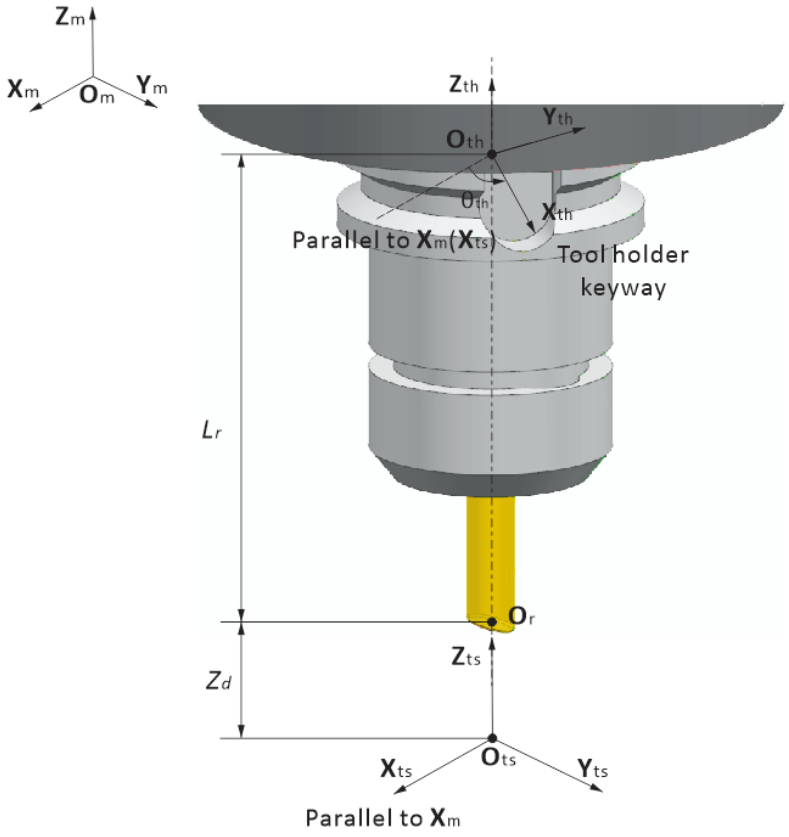

Figure 2.13. Illustration of the relationships among the tool holder coordinate system $\mathbf{X}_{th}\mathbf{Y}_{th}\mathbf{Z}_{th}\mathbf{O}_{th}$ and the tool setter coordinate system $\mathbf{X}_{ts}\mathbf{Y}_{ts}\mathbf{Z}_{ts}\mathbf{O}_{ts}$.

At any moment, in the tool setter coordinate system, the rod bottom center $\mathbf{O}_r$ is represented as

$$
\begin{aligned}
{}^{ts}\mathbf{O}_r &= {}^{ts}\mathbf{M}_{th} \cdot {}^{th}\mathbf{O}_r \\
&= \begin{bmatrix} 0 \\ 0 \\ Z_d \\ 1 \end{bmatrix}
\end{aligned} \tag{2.20}
$$

The cylindrical face of the end measuring rod is represented as

$$
{}^{ts}\mathbf{F}_c\left(h,u,Z_d\right) = {}^{ts}\mathbf{M}_{th} \cdot {}^{th}\mathbf{F}_c\left(h,u\right) \tag{2.21}
$$

where $u \in [0,360\text{deg}], h \in \left[h_l + L_r + Z_d, L_r + Z_d\right]$. ${}^{ts}\mathbf{F}_c$ is a function of Z_d.

The fillet face of the end measuring rod is represented as

$$
{}^{ts}\mathbf{F}_f\left(u,v,Z_d\right) = {}^{ts}\mathbf{M}_{th} \cdot {}^{th}\mathbf{F}_f\left(u,v\right) \tag{2.22}
$$

where $v \in [0,1]$ and $u \in [0,360\text{deg}]$. ${}^{ts}\mathbf{F}_f$ is a function of Z_d.

2.4.3. Formulating equations of the area of the shaded region

The above-mentioned measuring mechanism emphasizes that the shaded region is irregular. From the geometric perspective, the shaded region is part of the measuring rod projection covering the red circular region (or the laser beam projection) on the photodiode. Unfortunately, the shaded region is difficult to compute. In this section, by using the mathematical representations of the laser beam and the measuring rod geometries in the tool setter coordinate system, the equations of the rod projection along the laser beam on the photodiode are

formulated, and the equations of computing the boundary and the area of the shaded region are derived.

Suppose plane PL is the photodiode plane of the receiver, which is perpendicular to the laser axis (see Figure 2.14). The laser beam is projected along the direction $\mathbf{L}_v$ (L for laser and v for vector) onto plane PL as a red circular region, and its boundary is $\mathbf{C}_l$ (l for laser). The end measuring rod is projected along the direction $\mathbf{L}_v$ on plane PL, and its projection boundary is $\mathbf{C}_{sp}$ (s for shape and p for projection). When the end measuring rod blocks the laser beam, a shaded region *A* (A for area) is generated in the circular region on plane PL. Geometrically, the shaded region *A* is bounded by $\mathbf{C}_{sp}$ and $\mathbf{C}_l$. To calculate the boundary and area of the shaded region A bounded by $\mathbf{C}_l$ and $\mathbf{C}_{sp}$, first, the mathematical equations of $\mathbf{C}_l$ and $\mathbf{C}_{sp}$ are derived. The boundary of the circular area $\mathbf{C}_l$ on plane PL is a circle. According to direction $\mathbf{L}_v$, the silhouette $\mathbf{C}_s$ (s for silhouette) of the end measuring rod is determined and $\mathbf{C}_s$ is projected onto plane PL for the boundary $\mathbf{C}_{sp}$ of the rod projection on plane PL (see Figure 2.14). Second, the boundary of the shaded region in the circular area is found. Then, the area of the shaded region is calculated. The mathematical model is established step by step in the following.

The laser beam direction pointing from the laser tool setter transmitter to its receiver photodiode is represented in the tool setter coordinate system as (see Figure 2.14)

$$ {}^{ts}\mathbf{L}_v = \begin{bmatrix} \cos\beta \cdot \cos\alpha \\ \cos\beta \cdot \sin\alpha \\ \sin\beta \\ 0 \end{bmatrix} \tag{2.23} $$

The measuring rod projection (perpendicular to the laser axis) is represented by its projected boundary, $\mathbf{C}_{sp}$ (see Figure 2.14). The boundary curve $\mathbf{C}_{sp}$ can be obtained by first finding the silhouette curve of the end measuring rod along the laser beam direction $\mathbf{L}_v$, ($\mathbf{C}_s$ in Figure 2.14) and then projecting this silhouette curve on the photodiode plane.

Figure 2.14 shows the laser beam, the end measuring rod, and their geometric relationships. In Section 2.4.1, the coordinate system of the laser tool setter is constructed, and the parametric equations of the cylindrical surface $\mathbf{F}_c$, the fillet surface $\mathbf{F}_f$, and the bottom plane $\mathbf{F}_b$ are derived. According to the projection direction $\mathbf{L}_v$, the silhouette curve of the rod surfaces satisfies the following equation,

$$ {}^{ts}\mathbf{N} \cdot {}^{ts}\mathbf{L}_v = 0 \tag{2.24} $$

where ${}^{ts}\mathbf{N}$ is the normal vector of surfaces $\mathbf{F}_c$, $\mathbf{F}_f$ and $\mathbf{F}_b$ in the tool setter coordinate system. For example, when $Z_d = Z_{dn}$, the silhouette curve of the fillet surface can be determined with the following equation,

$$ f(u,v)\big|_{Z_d = Z_{dn}} \equiv {}^{ts}\mathbf{N}_{F_f} \cdot {}^{ts}\mathbf{L}_v = 0 \tag{2.25} $$

where ${}^{ts}\mathbf{N}_{F_f}$ is the surface normal vector of the fillet surface in the tool setter coordinate system. ${}^{ts}\mathbf{N}_{F_f}$ can be calculated as

$$ {}^{ts}\mathbf{N}_{F_f} = \frac{\partial\, {}^{ts}\mathbf{F}_f(u,v)\big|_{Z_d=Z_{dn}}}{\partial u} \times \frac{\partial\, {}^{ts}\mathbf{F}_f(u,v)\big|_{Z_d=Z_{dn}}}{\partial v} \tag{2.26} $$

Since Eq. (2.25) is an implicit equation, a numerical method is applied to calculate the parameters (u,v) of many points on the silhouette curve, and the parameters are substituted into Eq.(2.22) to calculate the point coordinates in the tool setter coordinate system. By connecting these points, the silhouette curve ${}^{ts}\mathbf{C}_s$ is determined. Similarly, the silhouette curves of the cylindrical surface are determined. Since the cylindrical surface, the fillet surface and the bottom plane are smoothly connected, the silhouette curves of the surfaces are continuous and smooth (see Figure 2.11) and the bottom face does not contribute to the silhouette curves.

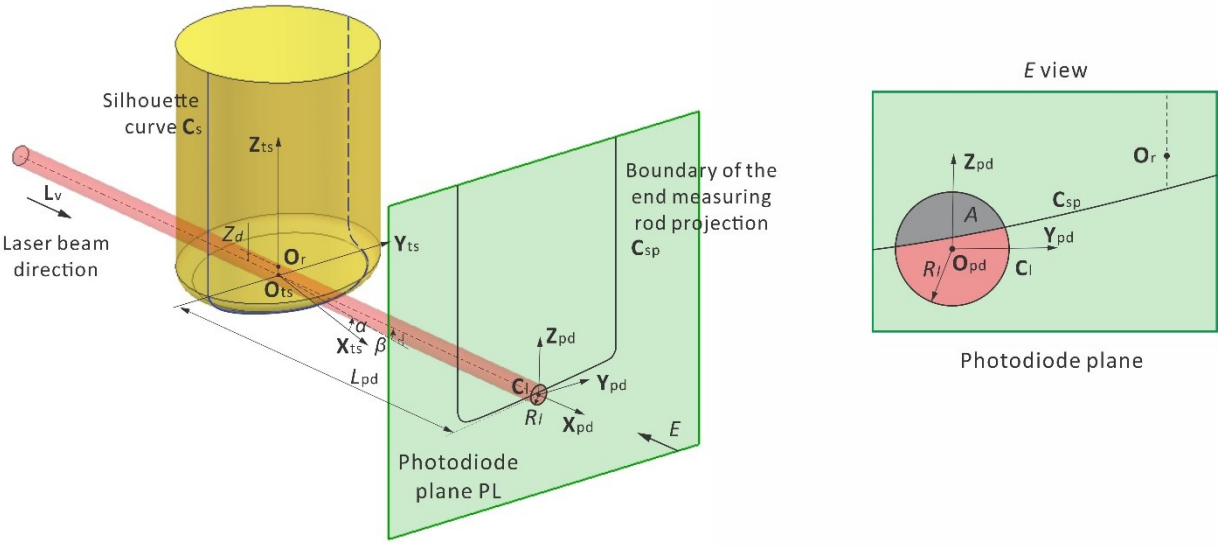

Figure 2.14. The mathematical model of calculating boundary and area of the shaded region in the circular area.

To calculate the shaded region A, the boundaries of the circular area $\mathbf{C}_l$ and the rod projection $\mathbf{C}_{sp}$ should be determined. First, a photodiode coordinate system ($\mathbf{X}_{pd}\mathbf{Y}_{pd}\mathbf{Z}_{pd}\mathbf{O}_{pd}$, pd for photodiode) is established as follows. In Figure 2.14, the intersection point $\mathbf{O}_{pd}$ between the laser axis and the photodiode plane is the origin. The laser axis is the $\mathbf{X}_{pd}$ axis, and the upward axis on the photodiode plane is the $\mathbf{Z}_{pd}$ axis. Thus, the relationship between the tool setter coordinate and the photodiode coordinate system is as follows.

The photodiode coordinate system is obtained by translating the tool setter coordinate system along the laser axis by distance L_{pd} and rotating it about $\mathbf{Z}_{ts}$ by α and about $\mathbf{Y}_{ts}$ by $-\beta$. Therefore, the transformation matrix from the tool setter coordinate system to the photodiode coordinate system is

$$ {}^{pd}\mathbf{M}_{ts} = \begin{bmatrix} \cos\alpha\cdot\cos\beta & \sin\alpha\cdot\cos\beta & \sin\beta & -L_{pd} \\ -\sin\alpha & \cos\alpha & 0 & 0 \\ -\cos\alpha\cdot\sin\beta & -\sin\alpha\cdot\sin\beta & \cos\beta & 0 \\ 0 & 0 & 0 & 1 \end{bmatrix} \tag{2.27} $$

Any point coordinates in the photodiode coordinate system $\mathbf{X}_{pd}$ - $\mathbf{Y}_{pd}$ - $\mathbf{Z}_{pd}$ - $\mathbf{O}_{pd}$ can be found by multiplying this matrix with the point coordinates $\mathbf{O}_{ts}\mathbf{X}_{ts}\mathbf{Y}_{ts}\mathbf{Z}_{ts}$ in the tool setter coordinate system.

In Figure 2.14, the laser beam projection on the photodiode is a circular area, so its boundary is a circle $\mathbf{C}_l$. When the end measuring rod is projected on the photodiode, the boundary $\mathbf{C}_{sp}$ of the shaded region is the projection of the silhouette curve $\mathbf{C}_s$. The equations of $\mathbf{C}_l$ and $\mathbf{C}_{sp}$ in the photodiode coordinate system are derived here. Since the boundary $\mathbf{C}_l$ is a circle, its parametric equation in the photodiode coordinate system is

$$ {}^{pd}\mathbf{C}_l = \begin{bmatrix} 0 \\ R_l \cdot \cos\theta_l \\ R_l \cdot \sin\theta_l \\ 1 \end{bmatrix} \tag{2.28} $$

where $\theta_l \in [0, 360\,\text{deg}]$ and R_l is the laser beam radius, which is specified by the tool setter manufacturer. The equation of $\mathbf{C}_{sp}$ in the photodiode coordinate system can be derived by formulating the equation of $\mathbf{C}_s$ in the photodiode coordinate system and projecting $\mathbf{C}_s$ onto the receiver screen. Thus, the equation of $\mathbf{C}_{sp}$ is

$$ {}^{l}\mathbf{C}_{sp} = \begin{bmatrix} 0 & 0 & 0 & 0 \\ 0 & 1 & 0 & 0 \\ 0 & 0 & 1 & 0 \\ 0 & 0 & 0 & 1 \end{bmatrix} \cdot {}^{l}\mathbf{M}_{ts} \cdot {}^{ts}\mathbf{C}_s \tag{2.29} $$

The shaded region A is bounded by boundaries $\mathbf{C}_l$ and $\mathbf{C}_{sp}$ on the receiver screen. Its area can be calculated based on its boundary. According to Eq. (2.28) of $\mathbf{C}_l$ and Eq. (2.29) of $\mathbf{C}_{sp}$,

boundary $\mathbf{C}_l$ is represented with a polygon Poly_{C_l}, and boundary $\mathbf{C}_{\text{sp}}$ is presented with a polygon $\text{Poly}_{C_{sp}}$. Then, a well-established method of calculating polygon intersection is applied, the intersection between polygons Poly_{C_l} and $\text{Poly}_{C_{sp}}$ is found. The boundary polygon Poly_A of the shaded region A is obtained by trimming polygons Poly_{C_l} and $\text{Poly}_{C_{sp}}$. Suppose the vertices of polygon Poly_A are $(y_1, z_1), (y_2, z_2), \ldots, (y_n, z_n)$. A well-established method of calculating the area of a region according to its polygon boundary is adopted. The area of the shaded region A can be calculated as

$$A = \frac{1}{2} \cdot \left(\begin{vmatrix} y_1 & y_2 \\ z_1 & z_2 \end{vmatrix} + \begin{vmatrix} y_2 & y_3 \\ z_2 & z_3 \end{vmatrix} + \ldots + \begin{vmatrix} y_m & y_1 \\ z_m & z_1 \end{vmatrix} \right) \tag{2.30}$$

The circular area of the laser beam projection can be calculated as

$$A_l = R_l^2 \cdot \pi \tag{2.31}$$

The ratio between the area of the shaded region and the circular area is

$$\eta = \frac{A}{A_l} \tag{2.32}$$

The equations of the mathematical model are derived, and this model is generic and accurate in calculating the area of the shaded region in the circular area during tool measurement. In practice, the end measuring rod has geometric errors, and it is clamped in the spindle with runout. The laser beam cannot be calibrated with perfect alignment with the machine axis. Under this

circumstance, the shaded region is irregular and its area is difficult to calculate. Fortunately, with this model, the area of the shaded region at any moment in laser beam calibration and the rod measurement location can be accurately and efficiently calculated. This model is a fundamental theory in tool measurement with the laser tool setter.

2.5 Establishing an accurate approach to determining Z coordinates of the laser axis reference point in the machine coordinate system

2.5.1 The kinematic chain of gauging system

Prior to the determination of the Z coordinates of $\mathbf{O}_{ts}$, its X- and Y- coordinates are determined. Generally, the end measuring rod used for calibration has high precisions in the radial directions and thus this research assumes the conventional calibration method can accurately determine the X- and Y- coordinates of $\mathbf{O}_{ts}$. To determine the Z coordinates of the laser axis reference point $\mathbf{O}_{ts}$ in the machine coordinate system, an end measuring rod is clamped in the machine spindle, and then the CNC machine moves the spindle and the rod to the laser tool setter so that the rod gauges the laser axis.

Thus, the kinematic chain of the gauging system consists of the CNC machine, the machine spindle, the measuring rod, and the laser tool setter. Each of the chain components has a unique coordinate system; the coordinate systems are called the machine ($\mathbf{X}_m\mathbf{Y}_m\mathbf{Z}_m\mathbf{O}_m$), the spindle

($\mathbf{X_s Y_s Z_s O_s}$), the tool holder ($\mathbf{X_{th} Y_{th} Z_{th} O_{th}}$), and the tool setter coordinate systems ($\mathbf{X_{ts} Y_{ts} Z_{ts} O_{ts}}$) (see Figure 2.15). The coordinate systems are defined as follows. $\mathbf{X_m Y_m Z_m O_m}$ is established in the machine setup by the machine manufacturer. $\mathbf{X_s Y_s Z_s O_s}$ is imaginarily defined at the spindle reference point, and its X-, Y- and Z-axes are parallel to the corresponding axes of $\mathbf{X_m Y_m Z_m O_m}$. The tool holder coordinate system is established and described in Section 4.2. $\mathbf{X_{ts} Y_{ts} Z_{ts} O_{ts}}$ is defined at the laser axis reference points, and its X-, Y- and Z-axes are parallel to the corresponding axes of $\mathbf{X_m Y_m Z_m O_m}$.

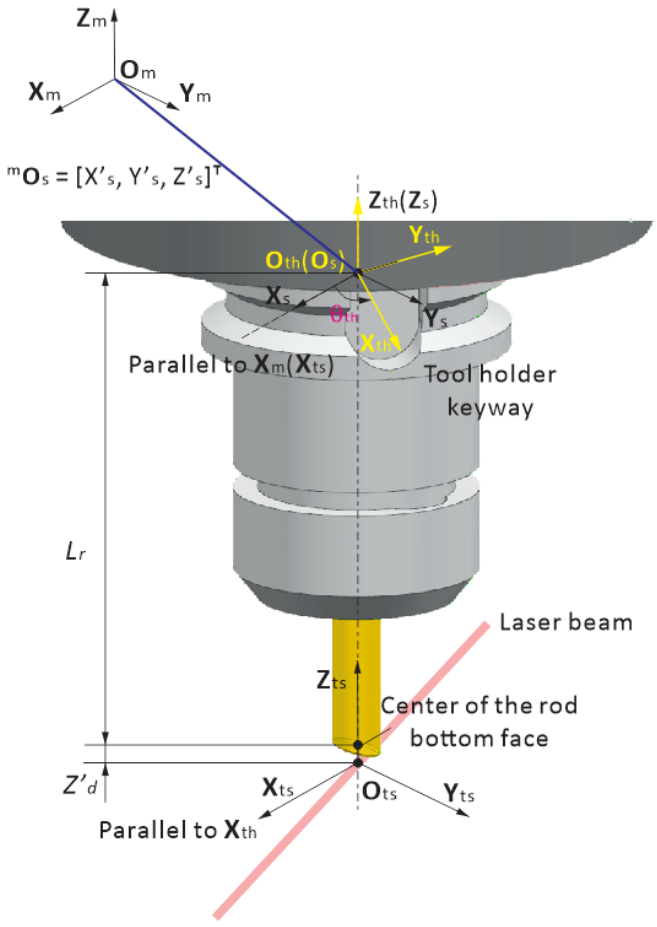

Figure 2.15. The kinematic chain of the gauging system.

When the measuring rod blocks the laser beam by 50% during calibration, the machine control records the coordinates of the spindle reference point at this instant, $\mathbf{O}'_s$ in $\mathbf{X}_m\mathbf{Y}_m\mathbf{Z}_m\mathbf{O}_m$. The spatial relationship that transforms from $\mathbf{X}_s\mathbf{Y}_s\mathbf{Z}_s\mathbf{O}_s$ to $\mathbf{X}_m\mathbf{Y}_m\mathbf{Z}_m\mathbf{O}_m$ can be derived as

$$ {}^{m}\mathbf{M}_{s} = \begin{bmatrix} 1 & 0 & 0 & X'_s \\ 0 & 1 & 0 & Y'_s \\ 0 & 0 & 1 & Z'_s \\ 0 & 0 & 0 & 1 \end{bmatrix} \tag{2.33} $$

where X'_s, Y'_s, and Z'_s are the coordinates of the spindle reference point in $\mathbf{X}_m\mathbf{Y}_m\mathbf{Z}_m\mathbf{O}_m$ when it reaches the gauging point. Since the spindle axis are aligned with the laser axis reference point in the Z direction and the X and Y coordinates of the laser axis reference point have been determined to be ${}^{m}O_{ts,x}$ and ${}^{m}O_{ts,y}$, Eq.(2.33) can be re-written as,

$$ {}^{m}\mathbf{M}_{s} = \begin{bmatrix} 1 & 0 & 0 & {}^{m}O_{ts,x} \\ 0 & 1 & 0 & {}^{m}O_{ts,y} \\ 0 & 0 & 1 & Z'_s \\ 0 & 0 & 0 & 1 \end{bmatrix} \tag{2.34} $$

According to the definition of $\mathbf{X}_{th}\mathbf{Y}_{th}\mathbf{Z}_{th}\mathbf{O}_{th}$ the transformation matrix from $\mathbf{X}_{th}\mathbf{Y}_{th}\mathbf{Z}_{th}\mathbf{O}_{th}$ to $\mathbf{X}_s\mathbf{Y}_s\mathbf{Z}_s\mathbf{O}_s$ is

$$ {}^{s}\mathbf{M}_{th} = \begin{bmatrix} \cos(\theta_{th}) & -\sin(\theta_{th}) & 0 & 0 \\ \sin(\theta_{th}) & \cos(\theta_{th}) & 0 & 0 \\ 0 & 0 & 1 & 0 \\ 0 & 0 & 0 & 1 \end{bmatrix} \tag{2.35} $$

and the transformation matrix from $\mathbf{X}_{ts}\mathbf{Y}_{ts}\mathbf{Z}_{ts}\mathbf{O}_{ts}$ to $\mathbf{X}_{th}\mathbf{Y}_{th}\mathbf{Z}_{th}\mathbf{O}_{th}$ is

$$ {}^{th}\mathbf{M}_{ts} = \begin{bmatrix} \cos(-\theta_{th}) & -\sin(-\theta_{th}) & 0 & 0 \\ \sin(-\theta_{th}) & \cos(-\theta_{th}) & 0 & 0 \\ 0 & 0 & 1 & 0 \\ 0 & 0 & 0 & 1 \end{bmatrix} \begin{bmatrix} 1 & 0 & 0 & 0 \\ 0 & 1 & 0 & 0 \\ 0 & 0 & 1 & -L_r - Z'_d \\ 0 & 0 & 0 & 1 \end{bmatrix} \tag{2.36} $$

where Z'_d is the Z-coordinate of the rod bottom center in $\mathbf{X}_{ts}\mathbf{Y}_{ts}\mathbf{Z}_{ts}\mathbf{O}_{ts}$ and it is obtained from the computer gauging simulation described in Section 4, when the area of the shaded region formed by the rod is 50% of the red laser beam circular area.

2.5.2 Mathematical representation of kinematics chain

From the above sections, the kinematics chain from $\mathbf{X}_{ts}\mathbf{Y}_{ts}\mathbf{Z}_{ts}\mathbf{O}_{ts}$ to $\mathbf{X}_{m}\mathbf{Y}_{m}\mathbf{Z}_{m}\mathbf{O}_{m}$ can be established and the transformation matrix from $\mathbf{X}_{ts}\mathbf{Y}_{ts}\mathbf{Z}_{ts}\mathbf{O}_{ts}$ to $\mathbf{X}_{m}\mathbf{Y}_{m}\mathbf{Z}_{m}\mathbf{O}_{m}$ is

$$ \begin{aligned} {}^{m}\mathbf{M}_{ts} &= {}^{m}\mathbf{M}_{s} \cdot {}^{s}\mathbf{M}_{th} \cdot {}^{th}\mathbf{M}_{ts} \\ &= \begin{bmatrix} 1 & 0 & 0 & {}^{m}O_{ts,x} \\ 0 & 1 & 0 & {}^{m}O_{ts,y} \\ 0 & 0 & 1 & Z'_s - L_r - Z'_d \\ 0 & 0 & 0 & 1 \end{bmatrix} \end{aligned} \tag{2.37} $$

and $\mathbf{O}_{ts}$ in $\mathbf{X}_{m}\mathbf{Y}_{m}\mathbf{Z}_{m}\mathbf{O}_{m}$ is

$$
{}^{m}\mathbf{O}_{ts} = {}^{m}\mathbf{M}_{ts} \cdot \begin{bmatrix} 0 \\ 0 \\ 0 \\ 1 \end{bmatrix} = \begin{bmatrix} {}^{m}O_{ts,x} \\ {}^{m}O_{ts,y} \\ Z'_{s} - L_{r} - Z'_{d} \\ 1 \end{bmatrix} \tag{2.38}
$$

This equation provides the means to calculate the Z-coordinates of the laser reference point in the machine coordinate system.

2.6 Verification and application

To verify the model and to demonstrate the significance of the proposed laser tool setter calibration method, two case studies are presented. Case study I demonstrates the accuracy of the proposed virtual gauging simulation and its mathematical model (described in Section 2.4). Case study II shows the validity of the calibration method (described in Section 2.5) with experiments.

In all the case studies, the three end measuring rods were used, including one rod with a bottom face perpendicular to the rod axis (known as a standard rod) and two end measuring rods with inclined bottom faces. Each rod was clamped on different tool holders. The radii of the rod flank cylinder R_r and the radii of the rounded edge R_f for each rod were measured on a tool

presetter. The bottom planes of end measuring rods were measured on a coordinate measurement machine (see Figure 2.16) and the geometries were converted into the tool holder coordinate system. The distance between the lowest point of the rod bottom and $\mathbf{O}_{th}$ both on the tool presetter and the coordinate machine for geometries information conversion. L_r is calculated based on the CMM measured geometries. All the rods have the same flank cylinder radius of 5 mm. The rounded edge radii of the rods were quite small in practice, not larger than 0.03 mm, as shown in Table 2.1. For the two rods with inclined bottom faces, one had a bottom face noticeably angled with regards to its axis and the other one was less inclined. The rod parameters are summarized in Table 2.1.

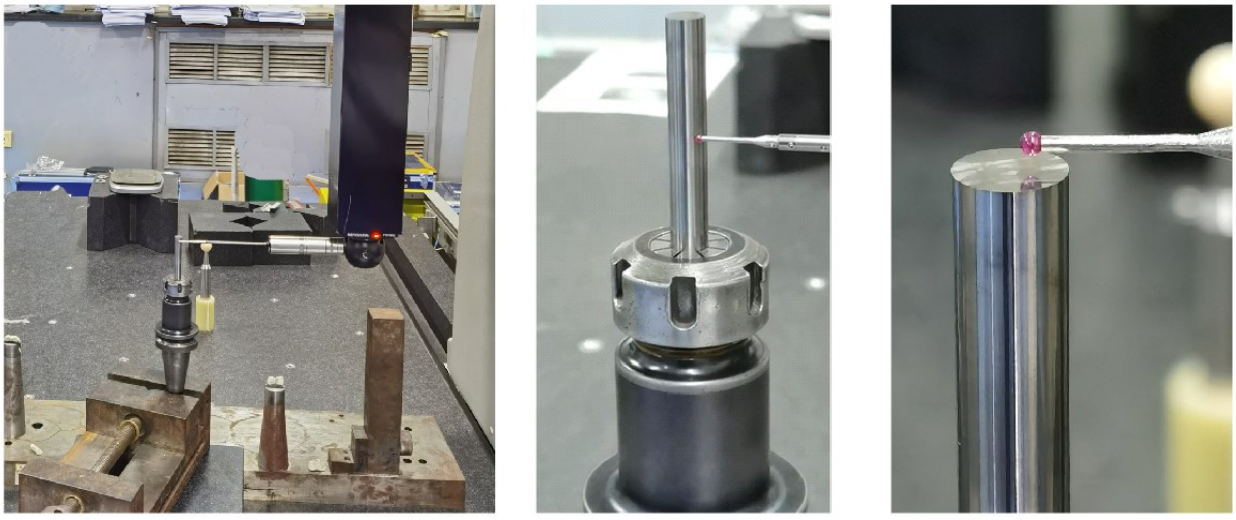

Figure 2.16 Gauging the geometries of the end measuring rod with a coordinate measurement machine.

Table 2.1. Parameters of three end measuring rods.

Parameters	Standard rod	Rod #1	Rod #2

Rod flank cylinder radius R_r (mm)	5	5	5
Rounded edge radius R_f (mm)	0	0.03	0.03
Angle φ (degree)	0	89.922	88.041
Angle τ (degree)	0	127.710	144.086
Distance between the rod bottom center and $\mathbf{O}_{th}$, L_r (mm)	133.702	160.591	179.822

2.6.1 Case Study I

This case study renders two examples to demonstrate the proposed mathematical model can accurately calculate the Z-coordinates of the rod bottom center in the laser coordinate system using a computer-aided simulation approach.

In both examples, the following verification methods were employed: First, the proposed mathematical model and virtual measurement simulation were implemented with programs in MATLAB software. This program was used along with the rod geometries and laser tool setter misalignment information to calculate the Z-coordinates of the rod bottom centers in the tool setter coordinate system, $Z_d^{'}$ at the triggering instant for the three end measuring rod. The laser projection shaded areas at the triggering instant were also recorded. To verify the calculation results, 3D models were first built in SIEMENS NX12® software by using the calculated $Z_d^{'}$ and the rod geometries data obtained from the tool presetter and the CMM. Finally, the shaded areas were measured in SIEMENS NX12® (see Figure 2.18) and the equality was verified against the calculated shaded area.

In the first example, the laser beam was assumed to be perfectly aligned with the machine X-axis, which means the pitch β and the yaw α angles are both equal 0°. The angle between the X-axes of $\mathbf{X}_{th}\mathbf{Y}_{th}\mathbf{Z}_{th}\mathbf{O}_{th}$ and $\mathbf{X}_{m}\mathbf{Y}_{m}\mathbf{Z}_{m}\mathbf{O}_{m}$ is $\theta_{th} = 0^{\circ}$. The initial searching values were selected to be 10 mm and the radius of the laser beam was $R_l = 0.2$ mm. A laptop computer with Intel Core i7 1.9GHz took about 3s to finish computing each case. 300 uniformly distributed sample points were used to represent the silhouette curve described in Eq.(2.25) and the computing accuracy of the Z coordinates of the end measuring rod bottom center was about 10^{-8} mm.

Table 2.2 listed the calculated $Z_d^{'}$ for the three rods and the corresponding laser projection shade areas and these results were also plotted in Figure 2.17. The measured shaded areas were also logged. It can readily be seen that the calculated shaded areas and the measured shaded areas in NX for both end measuring rods equal to each other up to the five decimal places. Further numerical comparison is not needed as the modeling accuracy of SIEMENS NX12® software for displaying irregular curves (in this case, the irregular curve is the projection of the rod bottom silhouette curve on the photodiode plane) is 0.0001 mm. This verifies the calculated z-coordinates for both rods were accurate. The results in Figure 2.17 also showed that when the end measuring rods with inclined bottom face triggered the laser beam, their bottom centers did not coincide with the laser axis, even though the laser beam aligned with the machine X-axis. Only when the standard rod with a flat surface was used to trigger a perfectly aligned laser tool setter would the rod bottom center coincide with the laser beam axis. Additionally, the maximum calculated Z coordinates of the three rods (shown in both Table 2.2 and Figure 2.17) reach up to

0.1376mm. If the geometry factors of the end measuring rods were ignored, as they were in traditional calibration methods, the Z coordinates differences would directly influence the accuracy of the calibration of the laser tool setter, rendering the calibration process erroneous.

Table 2.2 The calculated Z coordinates of the end measuring rod bottom center in the tool setter coordinate system and their corresponding calculated and measured shaded areas in example1.

	Z coordinates calculated by the simulations (Z'd)	Shaded area calculated by the simulations	Shaded area measured in NX software
Standard Rod	0 mm	0.06283 mm^2	0.06283 mm^2
Rod #1	0.0041 mm	0.06283 mm^2	0.06283 mm^2
Rod #2	0.1376 mm	0.06283 mm^2	0.06283 mm^2

(a)

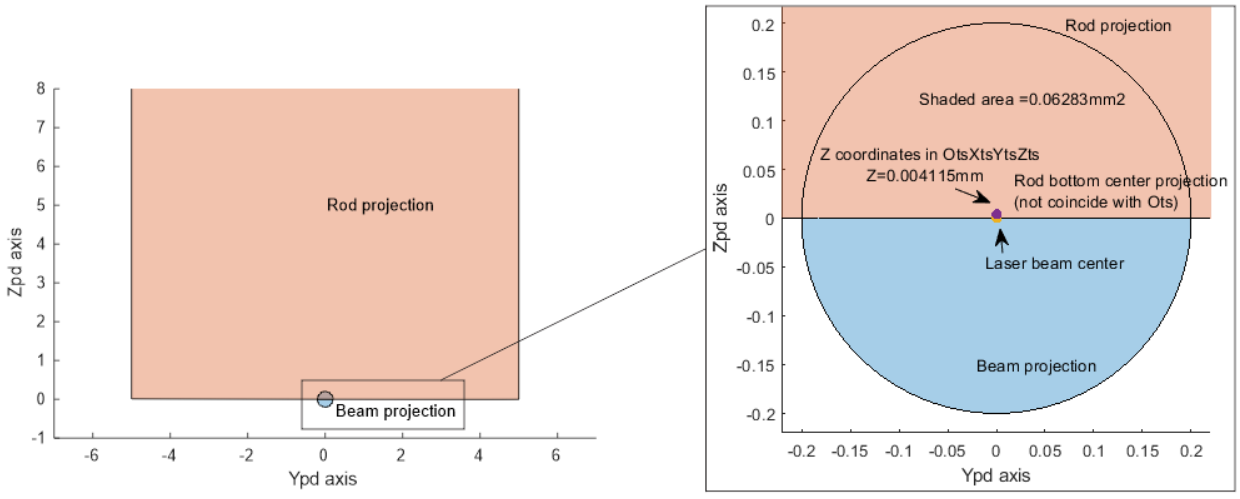

(b)

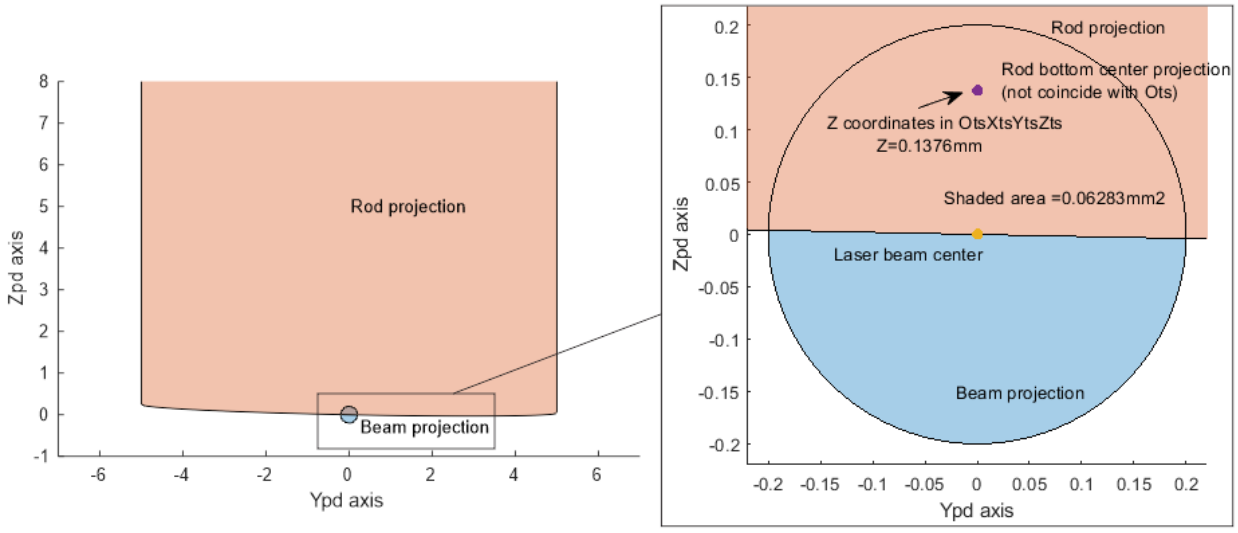

Figure 2.17. Simulation results of two end measuring rods blocking the laser in example 1; a) simulation results for rod #1 and b) simulation results for rod #2.

(a)

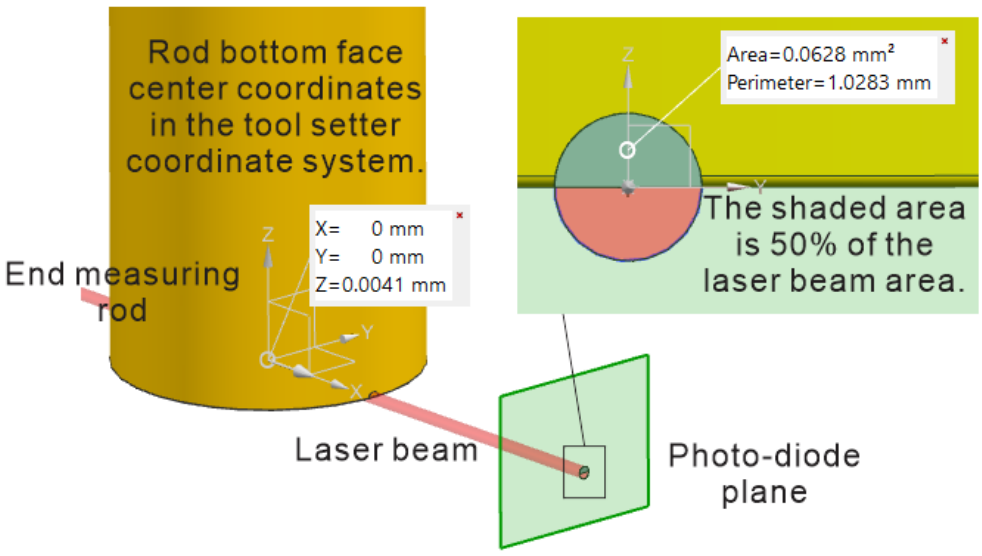

(b)

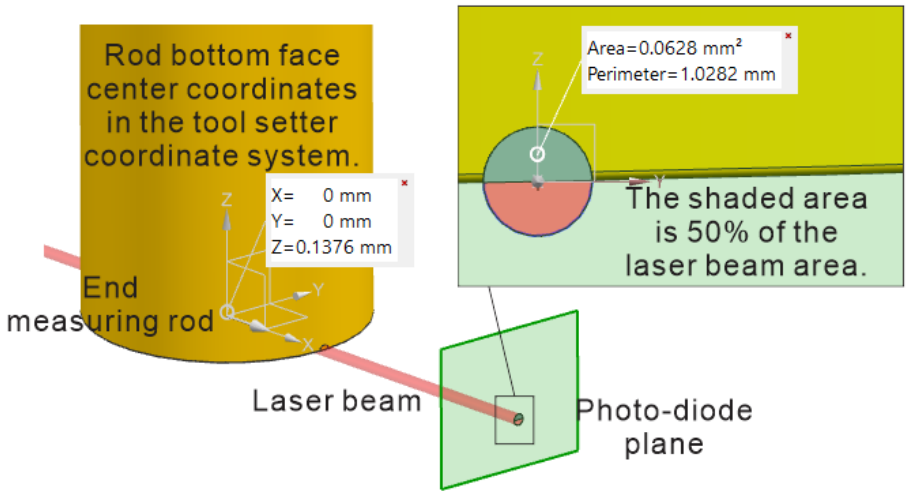

Figure 2.18 Verification of the simulated results of two end measuring rods blocking the laser in SIEMENS NX for example 1.

A second example is rendered for further discussion and comparison. In this example, the laser beam was misaligned with the machine X-axis. The laser axis has a pitch angle $\beta = 0.2836^{\circ}$ and a yaw angle $\alpha = 0.6241^{\circ}$. The program was run again with other parameters unchanged to calculate $Z_d^{'}$ for the three rods and the corresponding laser projection shade areas. The results were verified in the SIEMENS NX12® software.

The calculated Z coordinates for each rod and their corresponding shaded areas are listed in Table 2.3 and shown in Figure 2.19. It can be seen that using the simulated Z coordinates at triggering time to build the 3D model for each end measuring rod in SIEMENS NX12® (see Figure

2.20) could yield a shaded area that equals exactly 50% of the laser beam projection. This verifies the accuracy of the simulation. It is also obvious that when the laser beam is misaligned with the machine X-axis, even a standard end measuring rod is used for calibration, its bottom center does not coincide with the laser beam axis. In this example, the distance between the bottom center of the standard end measuring rod and the laser axis reaches 0.0246 mm. It is important to compensate for these differences in the calibration process.

(a)

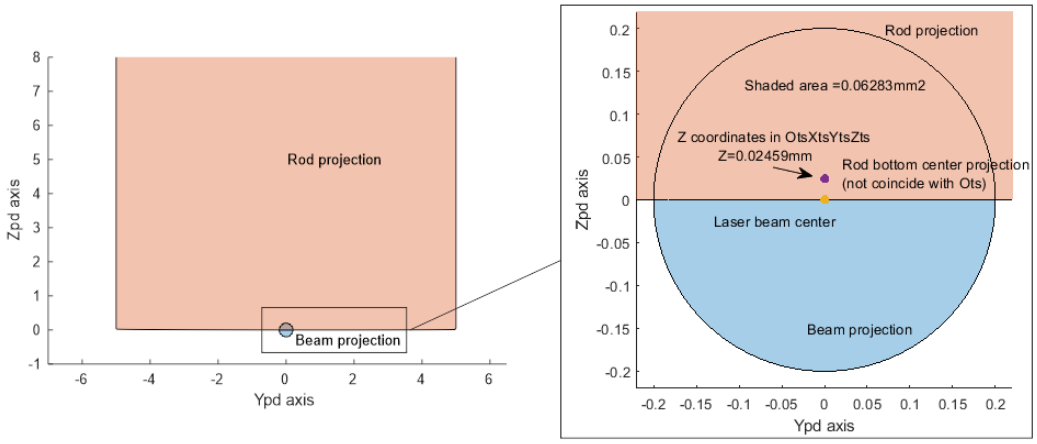

(b)

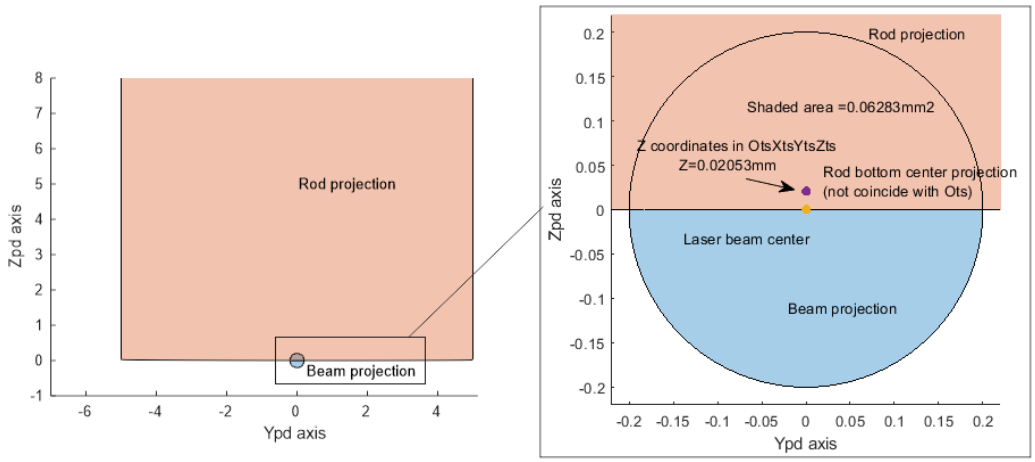

(c)

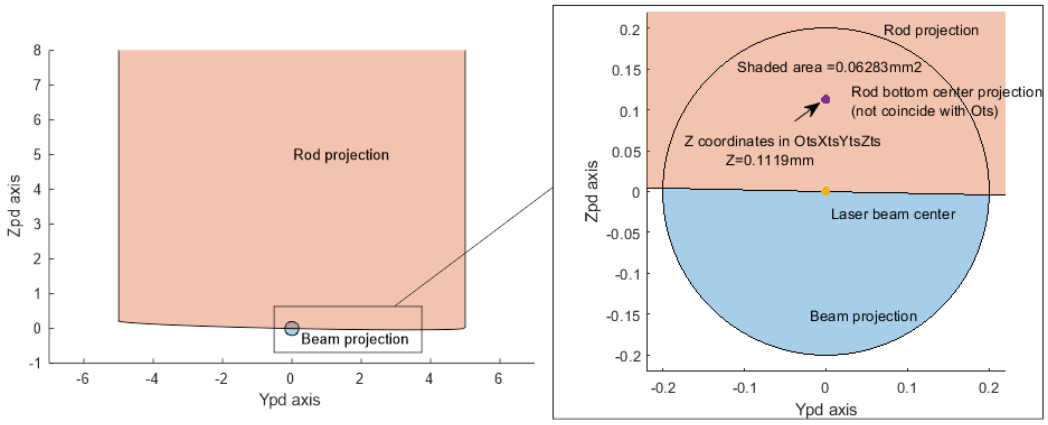

Figure 2.19. Simulation in example 2; a) results for the standard end measuring rod; b) results for rod #1 and 3) results for rod #2.

Table 2.3. Summary of the calculated Z coordinates of the end measuring rod bottom center in the tool setter coordinate system and their corresponding calculated and measured shaded areas in example2.

	Z coordinates calculated by the simulations	Shaded area calculated by the simulations	Shaded area measured in NX software
Standard Rod	0.0246 mm	0.06283 mm^2	0.06283 mm^2
Rod #1	0.0205 mm	0.06283 mm^2	0.06283 mm^2
Rod #2	0.1119 mm	0.06283 mm^2	0.06283 mm^2

(a)

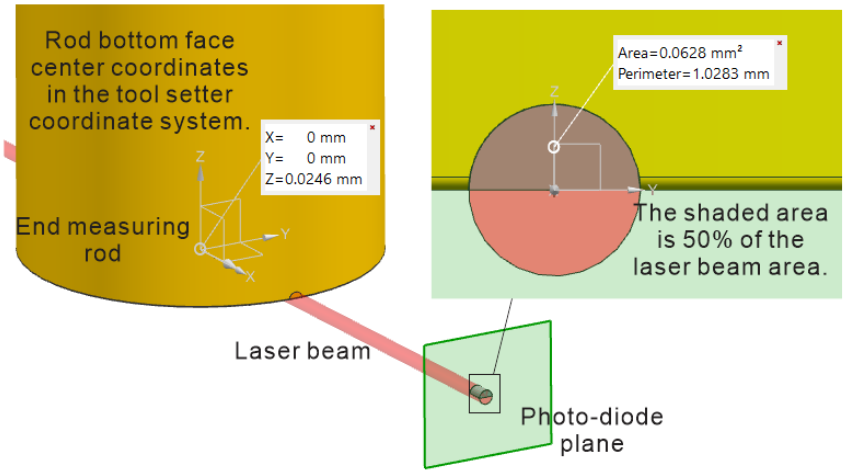

(b)

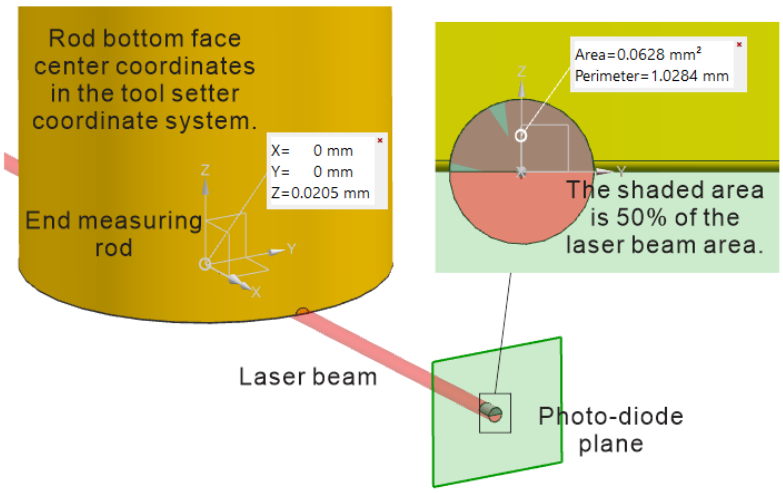

(c)

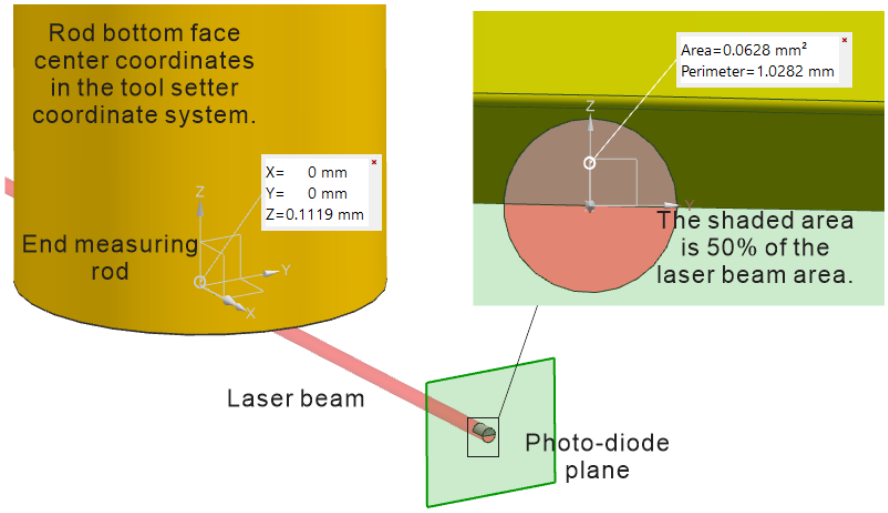

Figure 2.20 Verification of the simulated results of two end measuring rod blocking the laser in SIEMENS NX for example 2.

2.6.2 Case Study II

Experiments were carried out in this case study to confirm the validity of the proposed calibration method. The three end measuring rods were used to calibrate a laser tool setter installed on a CNC machine. Two calibration scenarios were examined in this case study: 1) the tool setter is perfectly aligned and 2) the tool setter is misaligned. The verification methods for these two scenarios were the following: 1) For the perfectly aligned case, using the standard rod with conventional methods can determine the true Z-coordinates of the laser axis in the machine coordinate system (since $Z_d^{'} = 0$ in Eq.(2.38)). The true Z-coordinates would be used as the benchmark. Other end measuring rods were used to determine the same Z-coordinates of the laser axis in the machine coordinate system with the proposed method. Comparing the output of the proposed method to the benchmark can showcase the validity of the proposed method;

2) For the misaligned case, since no currently available methods can determine the Z-coordinates of the laser reference point in the machine coordinate system, we check if using the proposed method can yield the same outcome even though end measuring rods with different geometries were used.

The machine in the experiment is a DMG CMX 50 U 5-axis CNC machine (Figure 2.21) and its spindle also pairs with SK-50 chucks. The angle between the X-axes of $\mathbf{X}_{th}\mathbf{Y}_{th}\mathbf{Z}_{th}\mathbf{O}_{th}$ and $\mathbf{X}_{m}\mathbf{Y}_{m}\mathbf{Z}_{m}\mathbf{O}_{m}$ is $\theta_{th} = 0^{\circ}$. Each rod was fed to triggered the laser tool setter. The measurement feed rate applied was 4mm/min and the spindles' orientations are fixed during the experiment. The Z coordinates of the spindle reference point in $\mathbf{X}_{m}\mathbf{Y}_{m}\mathbf{Z}_{m}\mathbf{O}_{m}$ when it reaches the gauging point, Z'_{s}, is obtained from the CNC control. The coordinates of the laser reference point were determined using Eq.(2.38). Z'_{d} is calculated with the program developed in Section 2.5. The experiment was repeated 3 times.

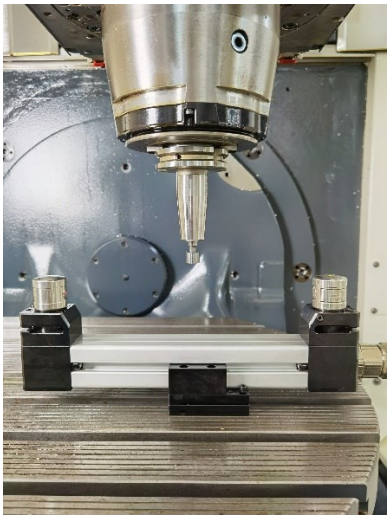

Figure 2.21. The machines used for the experiment.

Table 2.4. Experiment results for the perfectly aligned tool setter.

		Standard rod	Rod #1	Rod #2
Z'_s (mm)	Readout 1	-376.586	-349.695	-330.327
	Readout 2	-376.586	-349.695	-330.327
	Readout 3	-376.586	-349.695	-330.327
	Average	-376.586	-349.695	-330.327
L_r (mm)		133.702	160.591	179.822
Z'_d (mm)		0	0.0041	0.1376
${}^mO_{ts,z}$ (mm)		-510.288 (Benchmark)	-510.290	-510.287
Deviation from ${}^mO_{ts,z}$ gauged by the standard rod (mm)		0	-0.002	0.001

To address the first scenario, the calibration experiment was conducted on a perfectly aligned tool setter. The laser axis has a pitch angle $\beta = 0^\circ$ and a yaw angle $\alpha = 0^\circ$. Table 2.4 lists the experiment results, including the measured Z coordinates of the spindle reference point in $\mathbf{X}_m\mathbf{Y}_m\mathbf{Z}_m\mathbf{O}_m$ when the rod triggers the laser tool setter (Z'_s), the rod bottom center Z coordinates in $\mathbf{X}_{ts}\mathbf{Y}_{ts}\mathbf{Z}_{ts}\mathbf{O}_{ts}$ (Z'_d) and the determined Z coordinates of the laser reference point (${}^mO_{ts,z}$) in $\mathbf{X}_m\mathbf{Y}_m\mathbf{Z}_m\mathbf{O}_m$. Z'_d are obtained from Table 2.4. The distance between the rod bottom center and $\mathbf{O}_{th}$, L_r, are included to provide convenience for viewing. As can be seen, the Z-coordinates of the laser reference point of the tool setter was measured as 510.288 mm using the standard rod. This was the average of three readouts using the standard rod and it was taken as the benchmark.

${}^{m}O_{ts,z}$ measured by rod #1 and rod #2 were -510.290 mm and -510.287 mm. Their deviations from the benchmark were -0.002 mm and 0.001 mm. It can be observed that although geometries of the end measuring rods vastly differ from each other and the standard rod, with the proposed, the determined Z coordinates of the laser beam reference point are very close to the results obtained using the standard rods (less than 0.01mm). This suggests the proposed methods are very accurate. The slight differences between the determined ${}^{m}O_{ts,z}$ for each rod were most likely from the incomplete description of the rod geometries since only a finite number of data points on the rods could be obtained using a CMM.

In the same manner, a second calibration experiment was carried out on a misaligned tool setter.

Table 2.5. Experiment results with $\alpha = 0.6241^{\circ}$ and $\beta = 0.2836^{\circ}$

		Standard rod	Rod #1	Rod #2
Z'_s (mm)	Readout 1	-376.137	-349.258	-329.932
	Readout 2	-376.137	-349.258	-329.932
	Readout 3	-376.137	-349.258	-329.932
	Average	-376.137	-349.258	-329.932
L_r (mm)		133.702	160.591	179.822
Z'_d (mm)		0.025	0.021	0.112
${}^{m}O_{ts,z}$ (mm)		-509.864	-509.870	-509.866
Range of ${}^{m}O_{ts,z}$ (mm)		0.006		

Table 2.6. Experiment #2 results with $\alpha = 0.6240^{\circ}$ and $\beta = 0.5729^{\circ}$

		Standard rod	Rod #1	Rod #2
Z'_s (mm)	Readout 1	-374.616	-347.733	-328.46
	Readout 2	-374.616	-347.733	-328.46
	Readout 3	-374.616	-347.733	-328.461
	Average	-374.616	-347.733	-328.46
L_r (mm)		133.702	160.591	179.822
Z'_d (mm)		0.054	0.050	0.083
${}^mO_{ts,z}$ (mm)		-508.372	-508.374	-508.365
Range of ${}^mO_{ts,z}$ (mm)		0.009		

Table 2.7. Experiment #3 results with $\alpha = 0.9424^\circ$ and $\beta = 0.0911^\circ$

		Standard rod	Rod #1	Rod #2
Z'_s (mm)	Readout 1	-376.513	-349.62	-330.271
	Readout 2	-376.515	-349.62	-330.270
	Readout 3	-376.513	-349.62	-330.270
	Average	-376.514	-349.62	-330.270
L_r (mm)		133.702	160.591	179.822
Z'_d (mm)		0.007	0.003	0.128
${}^mO_{ts,z}$ (mm)		-510.223	-510.214	-510.220
Range of ${}^mO_{ts,z}$ (mm)		0.007		

Table 2.5 to Table 2.7 listed the measured Z coordinates of the spindle reference point in $\mathbf{X}_m\mathbf{Y}_m\mathbf{Z}_m\mathbf{O}_m$ when it triggers the laser tool setter (Z'_s), the simulated rod bottom center Z coordinates in $\mathbf{X}_{ts}\mathbf{Y}_{ts}\mathbf{Z}_{ts}\mathbf{O}_{ts}$ (Z'_d), and the gauged Z coordinates of the laser reference point (${}^mO_{ts,z}$) in $\mathbf{X}_m\mathbf{Y}_m\mathbf{Z}_m\mathbf{O}_m$. The most important result of the three experiments is that in each test, the gauged ${}^mO_{ts,z}$ using three rods were very close to each other. Namely, the range of the three ${}^mO_{ts,z}$ in the

first set of tests was 0.006 mm, in the second set of tests was 0.009 mm, and in the third set of tests was 0.007 mm. This suggests that when the laser tool setter is misaligned, with the proposed method, regardless of the rod geometries, the determined Z coordinates of the laser reference point are consistent and the proposed method is accurate. In addition, in three sets of tests, the rod bottom center Z coordinates of the standard measuring rod in $\mathbf{X}_{ts}\mathbf{Y}_{ts}\mathbf{Z}_{ts}\mathbf{O}_{ts}$ (Z'_d) at triggering instant varies and does not equal to zero. Specifically, in the first experiment, Z'_d for the standard measuring rod was 0.025 mm; in the second experiment, it was 0.054 mm; and in the third experiment, Z'_d for the standard measuring rod was 0.007 mm. If these gauging errors are disregarded, the calibration results would vary, depending on the misalignment of the laser tool setter. This indicates that when the laser tool setter is misaligned, gauging errors exist even though a standard measuring rod is used. Thus, the compensations method offered by the proposed method is essential. As for additional information, comparisons of ${}^{m}O_{ts,z}$ in three sets of tests are not necessary because the process of adjusting the laser axis angles would inevitably change the positions of the laser beam reference point. Finally, in the third test, both the yaw angle and the pitch angle are relatively large ($\alpha = 0.9424^{\circ}$ and $\beta = 0.0911^{\circ}$) but the range amongst the determined ${}^{m}O_{ts,z}$ of the three rods do not vary from that of the first and second test. This indicates the robustness of the proposed method against large laser tool setter misalignment.

2.7 Summary

This section proposed a novel theory for computer simulation of gauging in practical situations for calibrating on-machine laser tool setters. The fundamentals of the laser tool setters' working principles were first introduced. The practical application difficulties and the underlying scientific and geometric reasons were analyzed. Subsequently, we proposed a novel approach to calculating the rod origin in the tool setter coordinate system by studying the new mechanism of gauging the laser axis reference point. Mathematical models were built to calculate the area of the shaded region on the laser receiver photo-diode plane as the means to determine the relative positions between end measuring rods and the laser axis. In addition, the proposed computer simulation theory was applied and we established a novel method for determining the Z-coordinates of the laser tool setter in the machine coordinate system. Finally, the proposed computer simulation model and calibration methods were verified with computer-aided design software and experiment, showing very high accuracies.

Chapter 3

An Accurate and Efficient Approach for Measuring the Round Insert End-Mill Length and Bottom Cutting Edges Wear with On-Machine Laser Tool Setters

3.1 Introduction

Smart machining is aimed at automatically and efficiently machining parts with high dimension accuracy and better surface finish. An imperative and emerging technique of smart machining is on-machine measurement (OMM) of cutting tools, which includes the hardware of laser tool setters and measurement software (see Figure 3.1). Ideally, tool diameters and lengths and their wear can be automatically and constantly measured with laser tool setters on the machine table in regular machining breaks, the following machining is compensated with the tool size reduction, and the cutters are changed before they wear out. Therefore, the cutter OMM can achieve quality parts with high and consistent accuracy and less machining time without manual tool measurement on offline tool setters. Compared to solid carbide cutting tools, indexable cutters with inserts are more economic with good performance and are easier to change, and they are widely used in industry. In a machining process, inserts of the indexable cutting tool wear to a different extent. Until one insert is worn out, machining is stopped, and the insert is replaced. It is crucial to timely measure the tool length and the cutting edges wear with a laser tool setter. The current tool length is updated in the CNC controller, and the part is

cut with accurate z coordinates. Unfortunately, the current tool measurement software cannot measure cutter size with high accuracy and efficiency and cannot measure cutting edges wear in factories. This problem badly constrains the usage of the laser tool setters by machinists, and it is a bottleneck of smart machining (see Figure 3.2). Therefore, it is a must to develop advanced methods for the OMM of indexable cutters to meet the industry demand.

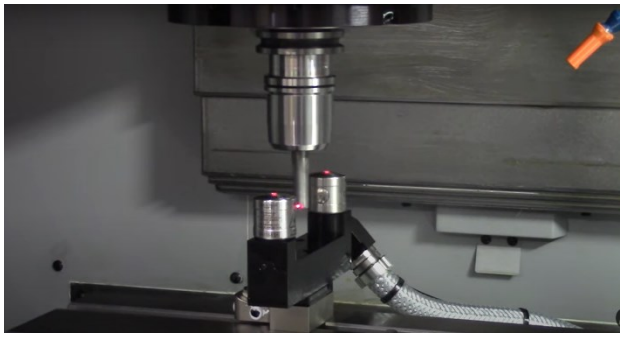

Figure 3.1. The cutter length is measured with a laser tool setter on a CNC machine.

Figure 3.2. An indexable end mill with round inserts is measured on a laser tool setter.

First, the status quo of the cutter OMM technique is introduced. As the OMM hardware, commercial laser tool setters, such as Renishaw and Blum laser tool setters, have been available for about 15 years[9, 53, 54]. A laser tool setter consists of a laser transmitter generating a laser

beam of a diameter of 0.4 mm and a receiver with a photodiode sensor. A laser beam emits from the transmitter and forms a circular light area of a diameter of 0.4 mm on the photodiode of the receiver. The working mechanism of laser tool setters is examined as follows [56, 81]. In a cutter measuring, when it gradually blocks the laser beam, the laser intensity on the photodiode is reduced, and the photodiode voltage is decreased. A dedicated circuit quickly monitors the photodiode voltage with a frequency of more than 96K Hz, so the lab test results show the repeatability of the tool setter is $\pm 1\ \mu m$ [53, 56, 81]. Until the cutter blocks the laser beam by 50% or more, the circuit finds out the photodiode voltage dropped below its threshold, and the tool setter triggers a signal to the CNC controller. Besides, the coolant droplets and the debris could block the laser beam, generating noise in the photodiode voltage. Thus, voltage patterns for different working conditions are recognized, and the measuring software can detect false signals. The laser tool setter mechanism, in general, is provided in the product manual, however, some data, such as the time starting from the tool setter sending a signal to the CNC controller receiving it, are not provided. Park *et al*. [13] and Lee *et al*. [59] put forward a photodiode property. Since the tool diameter is significantly larger than that of the laser beam, the photodiode voltage is linearly related to the ratio of the laser beam projection area on the photodiode to the shaded area generated by blocking the laser beam with the tool. This result is the fundamental physics of our research.

Parameters of measuring cutter size are important to measuring accuracy and efficiency. However, little research has been carried out to determine measuring parameters. The laser tool setter manufacturers have implemented their methods in software associated with their

hardware. Specifically, the spindle speed is high, and the feed rate is very low [81]. Thus, the measuring time is long. Generally, a laser tool setter can measure a tool length or a tool diameter in three minutes. Laser tool setters suffer from several error sources in practical application, including their installation misalignment, tool geometric difference, and the spindle speed and the feed rate [56, 63, 64]. Unfortunately, these error sources are ignored by the current laser tool setter manufacturers[66]. Renishaw [56]and Lee *et al*. [63] attempted to model the measurement errors in terms of the tool geometric error and setup error of the laser tool setter. In their model, the rotating tool is represented as a cylinder and the laser beam is represented as an inclined line. They approximated the measurement errors based on the front view and the top view of the setup. Their method does not consider the geometries of the cutter teeth nor the measurement of spindle speeds and feed rates. Milton *et al*. [82]focused on the calibration process and designed a set of experiments based on statistical analyses to identify the best feed rate and spindle speed for referencing laser tool-setters. Their method is experimentally based and does not study the measurement error during tool length measurement. Unfortunately, there is no research on a completed tool setting model using laser tool setters. In conclusion, the current tool length measurement methods employ high spindle speed and very slow feed rate and can only measure the lowest point of all cutting edges. These methods take a long time (about 2 minutes) to measure a cutter, and the random measurement error is large. Besides, these methods can only measure the cutting edge with the lowest point and cannot measure the other cutting edges for the maximum cutting-edge wear.

To address the problems of the current methods, this research discovers the tool length

characteristic curve and proposes an accurate and efficient approach to measuring the mill length and cutting-edges wear. First, the scientific fundamentals of measuring lengths of round-insert mills on laser tool setters are discussed. Second, the geometric model of inserts is derived, and the scientific theories of cutter length measurement are established. Then, the cutter length characteristic curve is discovered, and an accurate and efficient approach to measuring lengths of round-insert mills with laser tool setters. Finally, this approach is verified in two experiments. This research lays a theoretical foundation for on-machine cutter measurement, and can substantially advance smart machining technology.

3.2 Scientific fundamentals of measuring lengths of round-insert mills on laser tool setters

An indexable mill with round inserts consists of a group of replaceable round inserts, and a cutter body with the same number of seats and screws (or wedges), as shown in Figure 3.3. The inserts are clamped into the tool body seats; after an insert cutting edge wears out, the insert is re-indexed for a new cutting edge, or the insert is replaced with a new one. When the mill is only rotated by the spindle at the specified speed, without any feeding, the mill envelop is an imaginary surface of revolution. Thus, the mill length is regarded as the distance along the z-axis between the lowest point of the surface and the spindle reference point. Before using the mill, round inserts are manually screwed into the seats; unfortunately, they cannot be at the same height. While in machining, the inserts gradually wear to a different extent and their cutting

edges become irregular. Thus, the lowest point on one of the insert cutting edges determines the lowest point for the tool length. Conventionally, the indexable mill is measured on the offline tool setter by machinists. The tool is first set up in the tool setter with a chuck, and then by manually rotating the tool, the inserts' enlarged images are checked by eyes for the lowest point on an insert's cutting edge. Thus, this measurement is static. The length between the lowest point and the chuck reference point is read out as the tool length. The manual tool measurement on an offline tool setter takes a long time, and the tool cannot be measured on time for tool wear compensation in machining. Fortunately, automatic and in-process measurement of tools with a laser tool setter is a solution.

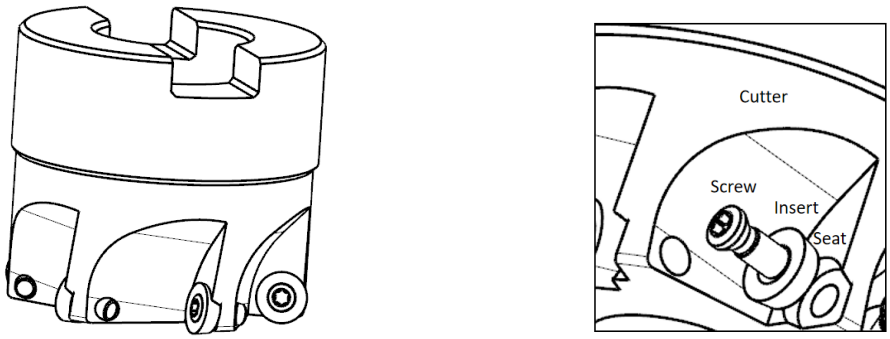

Figure 3.3. An indexable end mill with round inserts consists of a group of round inserts, and a tool body with seats and screws.

3.2.1 Mechanism and kinematics analysis of measuring the length of round-insert mills

The mechanism of cutter OMM with laser tool setters is introduced here. First, a laser tool setter is set up on the machine table with the laser beam axis aligned with either the machine x

or y-axis, and the machine x, y, and z coordinates of the laser axis are measured. Second, in measuring a round-insert mill, it is rotated; at the same time, it is fed toward the laser beam. Then, when a round insert blocks the laser beam by 50% or more, its photodiode sensor is triggered, sending a signal to the CNC controller; the machine coordinates of the spindle reference point are immediately recorded by the controller. Finally, its length is calculated by subtracting the z coordinate of the spindle reference point from the fixed z coordinate of the laser axis.

The kinematics of measuring lengths of round-insert mills with a laser tool setter is completely analyzed here. For an ideal mill with round inserts, the inserts are at the same height. Before measuring, a mill is set up in the spindle with its orientational angle between the first insert and the machine x-axis and is located at a height above the laser axis. In measuring, the mill rotates around the spindle axis and moves along the negative z-axis; the trajectory of the lowest point of each round insert is a helix. The helix radius is the distance between the lowest point and the spindle, and the helix pitch is the tool feed rate. Thus, the helix number is the same as the insert number. The helixes are shifted evenly along the z-axis by the central angle between two neighboring inserts. When an insert at a point of its helix blocks the laser beam by 50% or more, the z coordinate of the spindle reference point is immediately recorded, and the z coordinate of its lowest point could be less than that of the laser axis. The mill length is equal to subtracting the two z coordinates. Compared to the above situation, if the mill starts from a different height or its orientational angle between the first insert and the machine x-axis is different, another insert at a point of its helix could block the laser beam by 50% or more, the z

coordinates of the spindle reference point and the lowest point are different from the above situation. Thus, the true mill length is equal to the subtraction of the two z coordinates in each situation. For a real round-insert mill, the inserts cannot be installed at the same height, and the cutting edges of the inserts wear to different extents. The helixes generated by the lowest point on each insert are different in radius and phase shift. For each situation within a different height and an orientational angle, the mill length is equal to the subtraction of the z coordinates of the spindle reference point and the lowest point. Unfortunately, the z coordinate of the lowest point cannot be obtained.

A theory of measuring kinematics is that the measuring parameters, the spindle speed, and the tool feed rate, could significantly affect the accuracy and efficiency of measuring the tool length. The current measurement software calculates the mill length as subtraction of the z coordinate of the spindle reference point and that of the laser axis. However, the mill length is inaccurate. To increase measurement accuracy, the spindle speed is very high, and the feed rate is very low, for instance, the spindle speed is 3000 rpm, and the tool feed rate is 3 mm/min. This means the tool moves one micro in one revolution, resulting in a long measuring time, 2 to 3 minutes per measurement. Machinists cannot accept the long measuring time. This research establishes the measuring kinematics and proposes measuring simulation.

3.2.2 Blocking principles of measuring lengths of round-insert mills with a laser tool setter

To represent an insert blocking the laser beam, a geometry model is established. The laser beam projected on the diode plane is a circular area with a diameter of 0.4 mm. The round insert that blocks the laser beam forms a shade on the diode plane. The intersection between the circular area and the insert shade represents the laser beam blocked, which can be calculated. If the intersection area is more than 50% of the circular area, the measurement is completed. To measure the length of indexable mills with round inserts, the following principles are originally established.

Blocking principle 1:

To measure the length of indexable mills with round inserts, the laser beam should be blocked only by one insert.

[Proof]

The length of an indexable mill with round inserts is defined by the lowest point on the cutting edge of an insert. To measure the cutter length with a laser tool setter, it is necessary to measure the z coordinates of the lowest point and the spindle reference point and subtract the z coordinates. Thus, the insert with the lowest point should block the laser beam by 50%, and the z coordinate of the lowest point can be obtained. If two inserts block the laser beam, the z coordinate represents one of the two inserts. Therefore, the laser beam should be blocked only by one insert (see Figure 3.4).

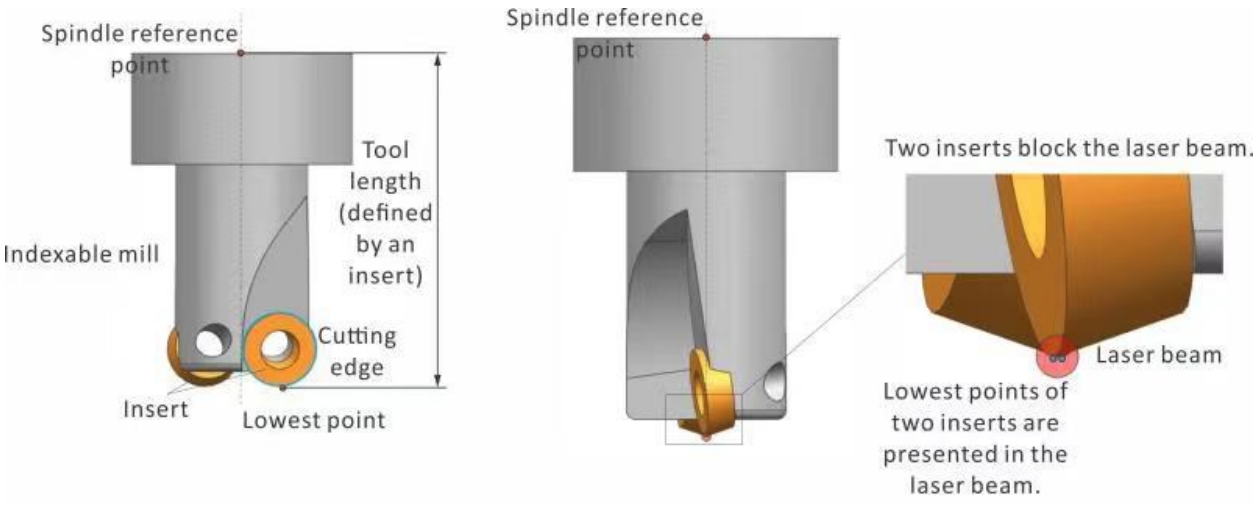

Figure 3.4. To measure the length of indexable mills with round inserts, the laser beam should be blocked only by one insert.

Blocking principle 2:

To measure the length of indexable mills with round inserts, the tool should be offset from the laser axis. The offset distance should not exceed the radius from the lowest point on the cutting edge of a round insert to the tool axis.

[Proof]

In measuring the length of indexable mills with round inserts, the relative location between the tool and the laser axis affects the length measuring accuracy. If the tool is offset from the laser axis by the tool axis, each insert can block the laser beam individually. Thus, it avoids

situations where multiple inserts block the laser beam at the same time. In addition, if the tool is offset from the laser axis by the distance from an insert's lowest point to the mill axis, the tool can block the laser beam in a maximum way by using its rake face. This avoids using the irregular flank face to block the beam. Thus, the tool length is more accurate (see Figure 3.5)

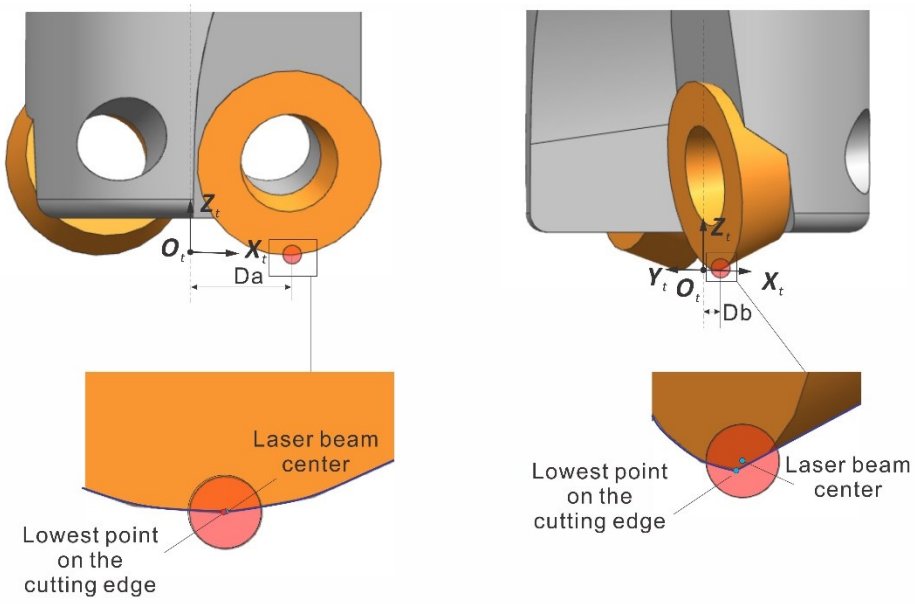

Figure 3.5. To measure the length of indexable mills with round inserts, the tool should be offset from the laser axis.

On the other hand, if the tool is offset from the laser axis by a distance larger than the radius from the lowest point on the cutting edge of a round insert to the tool axis, the lowest point of the cutting edge has no chance to block the laser beam. Thus, the measured tool length is erroneous.

3.3 Derivation of geometric models of the round inserts

The insert coordinate system ($\mathbf{X}_i$ - $\mathbf{Y}_i$ - $\mathbf{Z}_i$ - $\mathbf{O}_i$) is established as follows (see Figure 3.6). In this research, we pay attention to the rake face, the cutting edge, and the flank face of the insert. For a round insert, the cutting edge **E** is a circle and $\mathbf{C}_i$ is the center of the cutting edge. Two points on the cutting edge **E**, **A** and **B**, can be selected so that lines $\mathbf{C}_i\mathbf{A}$ and $\mathbf{C}_i\mathbf{B}$ are perpendicular to each other. The tangent lines of the cutting edge at **A** and **B** intersect at $\mathbf{O}_i$. $\mathbf{O}_i$ is the virtual cutting point of the insert in cutting design. The origin of the insert coordinate system is established at $\mathbf{O}_i$, the $\mathbf{X}_i$ axis is along the vector $\mathbf{BO}_i$, the $\mathbf{Z}_i$ axis is along the vector $\mathbf{O}_i\mathbf{A}$ and the $\mathbf{Y}_i$ axis follows the right-hand rule.

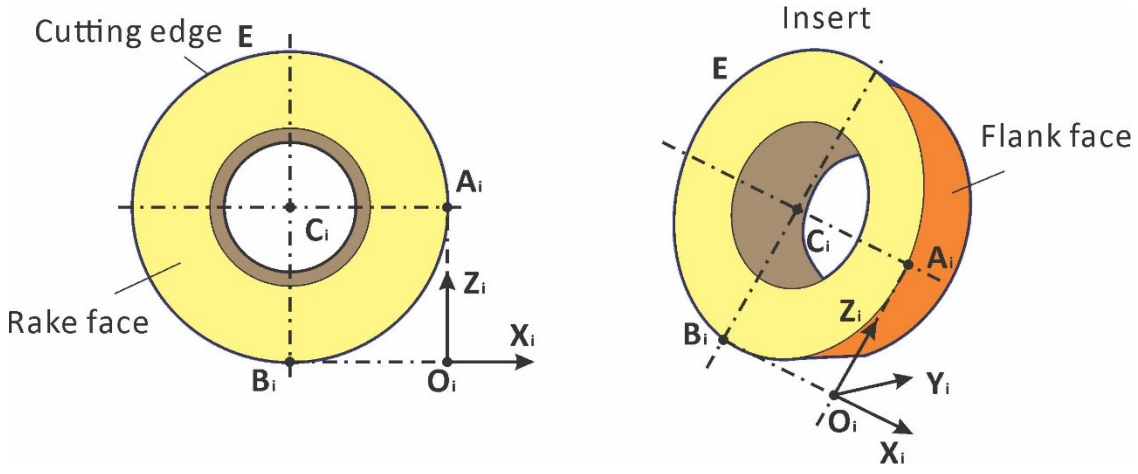

Figure 3.6. The establishment of the insert coordinate system.

We assumed that the rake angle of the insert is 0 and the rake face of the insert is represented by a plane. Since the cutting edge of the insert is a circle (see Figure 3.7) and the parametric equation of the cutting edge E in $\mathbf{X}_i$ - $\mathbf{Y}_i$ - $\mathbf{Z}_i$ - $\mathbf{O}_i$ is

$$ {}^{i}\mathbf{E} = \begin{bmatrix} R\cdot\cos(\alpha) - R \\ 0 \\ -R\cdot\sin(\alpha) + R \\ 1 \end{bmatrix}, \quad 0 \le \alpha \le 360^{\circ} \tag{3.1} $$

where R is the radius of the insert.

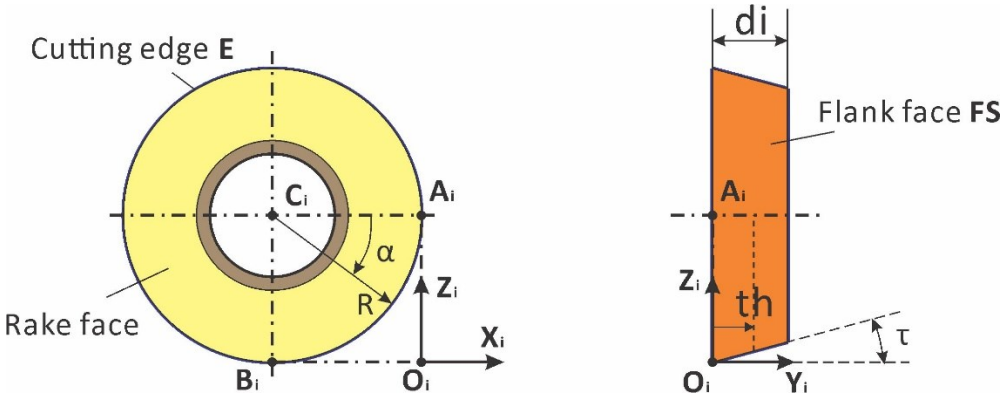

Figure 3.7. Parameterization of the cutting edge E.

The flank face of an insert, **FS**, is modeled with a frustum of a right circular cone (see Figure 3.7). The parametric equation for the flank face is

$$
{}^{i}\mathbf{FS} = \begin{bmatrix} \left(R - \dfrac{th}{\cot\tau}\right)\cdot\cos(\alpha) - R \\ th \\ -\left(R - \dfrac{th}{\cot\tau}\right)\cdot\sin(\alpha) + R \\ 1 \end{bmatrix}, \quad 0 \le \alpha \le 360^{\circ} \text{ and } 0 \le th \le di \tag{3.2}
$$

where di is the thickness of the insert and τ is the clearance angle of the insert.

The coordinate system for the indexable mill cutting tool ($\mathbf{X}_t$ - $\mathbf{Y}_t$ - $\mathbf{Z}_t$ - $\mathbf{O}_t$) is established as follows (see Figure 3.8). When an insert is clamped onto the cutter body, a plane passing through the virtual cutting point $\mathbf{O}_i$ of the insert and perpendicular to the tool axis intersects the tool axis at $\mathbf{O}_t$. The origin of the cutting tool coordinate system is set up at $\mathbf{O}_t$. The $\mathbf{Z}_t$ axis is along the tool axis; the $\mathbf{X}_t$ axis is defined by the vector $\mathbf{O}_t\mathbf{O}_i$, and the $\mathbf{Y}_t$ axis follows the right-hand rule. The distance between $\mathbf{O}_t$ and $\mathbf{O}_i$ is r, which is often approximately referred to as the radius of the cutter.

The relationship between the insert and the tool coordinate system is derived as follows. As illustrated in Figure 3.8, the insert is clamped onto the cutter body with a radial angle θ_r and an axial angle θ_a. The radial angle θ_r is measured from the $\mathbf{X}_t$ to $\mathbf{X}_i$ and the axial angle θ_a is measured defined as the angle between axial $\mathbf{Z}_i$ and plane **PI**, plane **PI** passing through the axial $\mathbf{O}_i\mathbf{X}_i$ and perpendicular to the plane $\mathbf{X}_t\mathbf{Z}_t$.

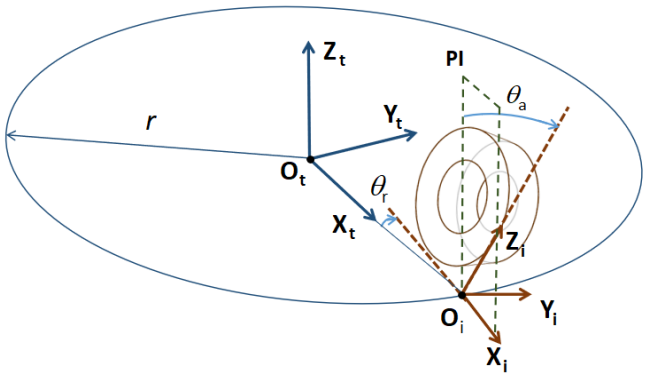

Figure 3.8. Location relationship between $\mathbf{X_t}$ - $\mathbf{Y_t}$ - $\mathbf{Z_t}$ - $\mathbf{O_t}$ and $\mathbf{X_i}$ - $\mathbf{Y_i}$ - $\mathbf{Z_i}$ - $\mathbf{O_i}$.

Based on the above geometries, the relationship between $\mathbf{X_t}$ - $\mathbf{Y_t}$ - $\mathbf{Z_t}$ - $\mathbf{O_t}$ and $\mathbf{X_i}$ - $\mathbf{Y_i}$ - $\mathbf{Z_i}$ - $\mathbf{O_i}$ can be derived and the equivalent transformation matrix from $\mathbf{X_i}$ - $\mathbf{Y_i}$ - $\mathbf{Z_i}$ - $\mathbf{O_i}$ to $\mathbf{X_t}$ - $\mathbf{Y_t}$ - $\mathbf{Z_t}$ - $\mathbf{O_t}$ is

$$ {}^{t}\mathbf{M}_{i} = \begin{bmatrix} 1 & 0 & 0 & r \\ 0 & 1 & 0 & 0 \\ 0 & 0 & 1 & 0 \\ 0 & 0 & 0 & 1 \end{bmatrix} \cdot \begin{bmatrix} \cos(\theta_r) & \sin(\theta_r) & 0 & 0 \\ -\sin(\theta_r) & \cos(\theta_r) & 0 & 0 \\ 0 & 0 & 1 & 0 \\ 0 & 0 & 0 & 1 \end{bmatrix} \cdot \begin{bmatrix} 1 & 0 & 0 & 0 \\ 0 & \cos(\theta_a) & \sin(\theta_a) & 0 \\ 0 & -\sin(\theta_a) & \cos(\theta_a) & 0 \\ 0 & 0 & 0 & 1 \end{bmatrix} \tag{3.3} $$

Thus, the parametric equation of the cutting edge in $\mathbf{X_t}$ - $\mathbf{Y_t}$ - $\mathbf{Z_t}$ - $\mathbf{O_t}$ is

$$ \begin{aligned} {}^{t}\mathbf{E} &= {}^{t}\mathbf{M}_{i} \cdot {}^{i}\mathbf{E} \\ &= \begin{bmatrix} R \cdot \left[\cos(\theta_r) \cdot (\cos(\alpha) - 1) + \sin(\theta_r) \cdot \sin(\theta_a) \cdot (1 - \sin(\alpha)) \right] + r \\ R \cdot \left[-\sin(\theta_r) \cdot (\cos(\alpha) - 1) + \cos(\theta_r) \cdot \sin(\theta_a) \cdot (1 - \sin(\alpha)) \right] \\ R \cdot \cos(\theta_a) \cdot (1 - \sin(\alpha)) \\ 1 \end{bmatrix}, \quad 0 \le \alpha \le 360^\circ \end{aligned} \tag{3.4} $$

and the parametric equation of the flank face in $\mathbf{X_t}$ - $\mathbf{Y_t}$ - $\mathbf{Z_t}$ - $\mathbf{O_t}$ is

$$
\begin{aligned}
{}^{t}\mathbf{FS} &= {}^{t}\mathbf{M}_{i} \cdot {}^{i}\mathbf{FS} \\
&= \begin{bmatrix} r - \cos(\theta_r)\cdot Q_2 + th\cdot\cos(\theta_a)\cdot\sin(\theta_r) + \sin(\theta_a)\cdot\sin(\theta_r)\cdot Q_1 \\ \sin(\theta_r)\cdot Q_2 + th\cdot\cos(\theta_a)\cdot\cos(\theta_r) + \cos(\theta_r)\cdot\sin(\theta_a)\cdot Q_1 \\ \cos(\theta_a)\cdot Q_1 - th\cdot\sin(\theta_a) \\ 1 \end{bmatrix}
\end{aligned} \tag{3.5}
$$

where

$$
Q_1 = R - \sin(\alpha)\cdot\left(R - \frac{th}{\cot(\tau)}\right) \tag{3.6}
$$

$$
Q_2 = R - \cos(\alpha)\cdot\left(R - \frac{th}{\cot(\tau)}\right) \tag{3.7}
$$

$0 \le \alpha \le 360^\circ$, and $0 \le th \le di$.

An indexable end mill is usually equipped with multiple inserts. The inserts are distributed uniformly around the tool axis. Supposed *n* inserts are installed on the end mill, the angle between each insert is (see Figure 3.9),

$$
\theta = \frac{360^\circ}{n} \tag{3.8}
$$

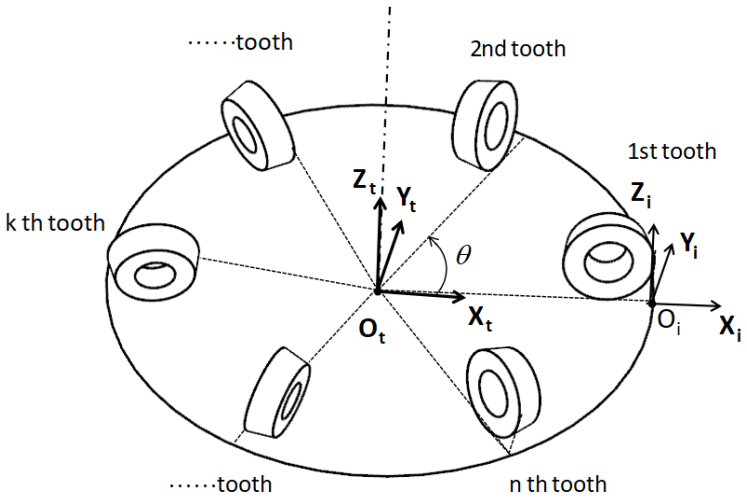

Figure 3.9. The arrangement of inserts on a cutting tool.

Supposed the $\mathbf{X}_t$ axis passes through $\mathbf{O}_i$ of the first insert and the cutting edge of the kth insert in $\mathbf{X}_t$ - $\mathbf{Y}_t$ - $\mathbf{Z}_t$ - $\mathbf{O}_t$ can be derived as

$$ {}^{t}\mathbf{EK}_o = \begin{bmatrix} \cos\left((k-1)\cdot\theta\right) & -\sin\left((k-1)\cdot\theta\right) & 0 & 0 \\ \sin\left((k-1)\cdot\theta\right) & \cos\left((k-1)\cdot\theta\right) & 0 & 0 \\ 0 & 0 & 1 & 0 \\ 0 & 0 & 0 & 1 \end{bmatrix} \cdot {}^{t}\mathbf{E}, \quad k = 1,2,\ldots,n \tag{3.9} $$

and the flank face of the kth insert in $\mathbf{X}_t$ - $\mathbf{Y}_t$ - $\mathbf{Z}_t$ - $\mathbf{O}_t$ is

$$ {}^{t}\mathbf{FSK}_o = \begin{bmatrix} \cos\left((k-1)\cdot\theta\right) & -\sin\left((k-1)\cdot\theta\right) & 0 & 0 \\ \sin\left((k-1)\cdot\theta\right) & \cos\left((k-1)\cdot\theta\right) & 0 & 0 \\ 0 & 0 & 1 & 0 \\ 0 & 0 & 0 & 1 \end{bmatrix} \cdot {}^{t}\mathbf{FS}, \quad k = 1,2,\ldots,n \tag{3.10} $$

When the tool wears out, the teeth have different heights in $\mathbf{X_t}$ - $\mathbf{Y_t}$ - $\mathbf{Z_t}$ - $\mathbf{O_t}$, and it is assumed that other tooth geometries do not change. Since the location of the first tooth is used to define $\mathbf{X_t}$ - $\mathbf{Y_t}$ - $\mathbf{Z_t}$ - $\mathbf{O_t}$, the parametric equations of the first tooth in $\mathbf{X_t}$ - $\mathbf{Y_t}$ - $\mathbf{Z_t}$ - $\mathbf{O_t}$ remain the same. For other teeth, the cutting edge of the kth insert in $\mathbf{X_t}$ - $\mathbf{Y_t}$ - $\mathbf{Z_t}$ - $\mathbf{O_t}$ is

$$ {}^{t}\mathbf{EK} = \begin{bmatrix} \cos\left((k-1)\cdot\theta\right) & -\sin\left((k-1)\cdot\theta\right) & 0 & 0 \\ \sin\left((k-1)\cdot\theta\right) & \cos\left((k-1)\cdot\theta\right) & 0 & 0 \\ 0 & 0 & 1 & W_{zk} \\ 0 & 0 & 0 & 1 \end{bmatrix} \cdot {}^{t}\mathbf{E}, \quad k = 1,2,...,n \tag{3.11} $$

and the flank face of the kth insert in $\mathbf{X_t}$ - $\mathbf{Y_t}$ - $\mathbf{Z_t}$ - $\mathbf{O_t}$ is

$$ {}^{t}\mathbf{FSK}_o = \begin{bmatrix} \cos\left((k-1)\cdot\theta\right) & -\sin\left((k-1)\cdot\theta\right) & 0 & 0 \\ \sin\left((k-1)\cdot\theta\right) & \cos\left((k-1)\cdot\theta\right) & 0 & 0 \\ 0 & 0 & 1 & W_{zk} \\ 0 & 0 & 0 & 1 \end{bmatrix} \cdot {}^{t}\mathbf{FS}, \quad k = 1,2,...,n \tag{3.12} $$

where W_{zk} is the wear amount of the kth tooth.

3.4 Kinematics and geometric models for simulation of cutter length measurement

3.4.1 Kinematics model establishment of measuring lengths of round-insert mills

To derive the kinematic model of measuring the indexable round inserted cutting tool, we need to describe the tool geometries and the measurement process in $\mathbf{X_{ts}}$ - $\mathbf{Y_{ts}}$ - $\mathbf{Z_{ts}}$ - $\mathbf{O_{ts}}$. In the tool length measurement setup (see Figure 3.10(a)), the laser tool setter coordinate system

($\mathbf{X}_{ts}$ - $\mathbf{Y}_{ts}$ - $\mathbf{Z}_{ts}$ - $\mathbf{O}_{ts}$) is defined on the laser axis and is parallel to the machine coordinate system ($\mathbf{X}_{m}$ - $\mathbf{Y}_{m}$ - $\mathbf{Z}_{m}$ - $\mathbf{O}_{m}$). The transformation matrix from $\mathbf{X}_{m}$ - $\mathbf{Y}_{m}$ - $\mathbf{Z}_{m}$ - $\mathbf{O}_{m}$ to $\mathbf{X}_{ts}$ - $\mathbf{Y}_{ts}$ - $\mathbf{Z}_{ts}$ - $\mathbf{O}_{ts}$ is

$$ {}^{ts}\mathbf{M}_{m} = \begin{bmatrix} 1 & 0 & 0 & -X_{ts} \\ 0 & 1 & 0 & -Y_{ts} \\ 0 & 0 & 1 & -Z_{ts} \\ 0 & 0 & 0 & 1 \end{bmatrix} \tag{3.13} $$

where X_{ts} , Y_{ts} , and Z_{ts} are the X, Y, and Z coordinates of $\mathbf{O}_{ts}$ in $\mathbf{X}_{m}$ - $\mathbf{Y}_{m}$ - $\mathbf{Z}_{m}$ - $\mathbf{O}_{m}$. These coordinates are determined during the calibration process. A spindle coordinate system $\mathbf{X}_{s}$ - $\mathbf{Y}_{s}$ - $\mathbf{Z}_{s}$ - $\mathbf{O}_{s}$ is used to describe the position of the spindle in $\mathbf{X}_{m}$ - $\mathbf{Y}_{m}$ - $\mathbf{Z}_{m}$ - $\mathbf{O}_{m}$. When the machine and the spindle are at home position, $\mathbf{X}_{s}$ - $\mathbf{Y}_{s}$ - $\mathbf{Z}_{s}$ - $\mathbf{O}_{s}$ coincides with $\mathbf{X}_{m}$ - $\mathbf{Y}_{m}$ - $\mathbf{Z}_{m}$ - $\mathbf{O}_{m}$. When the spindle rotates, $\mathbf{X}_{s}$ and $\mathbf{X}_{m}$ forms an angle θ_{s} . When the tool is installed on the spindle, $\mathbf{X}_{t}$ forms an angle θ_{t} with $\mathbf{X}_{s}$, $\mathbf{Z}_{t}$ coincides with $\mathbf{Z}_{s}$, and the distance between $\mathbf{O}_{t}$ and $\mathbf{O}_{s}$ defines the tool length L_{t} . The transformation matrix from $\mathbf{X}_{s}$ - $\mathbf{Y}_{s}$ - $\mathbf{Z}_{s}$ - $\mathbf{O}_{s}$ to $\mathbf{X}_{m}$ - $\mathbf{Y}_{m}$ - $\mathbf{Z}_{m}$ - $\mathbf{O}_{m}$ is

$$ {}^{m}\mathbf{M}_{s} = \begin{bmatrix} \cos\theta_{s} & -\sin\theta_{s} & 0 & X_{s} \\ \sin\theta_{s} & \cos\theta_{s} & 0 & Y_{s} \\ 0 & 0 & 1 & Z_{s} \\ 0 & 0 & 0 & 1 \end{bmatrix} \tag{3.14} $$

where X_{s} , Y_{s} , and Z_{s} are the X, Y, and Z coordinates of $\mathbf{O}_{s}$ in $\mathbf{X}_{m}$ - $\mathbf{Y}_{m}$ - $\mathbf{Z}_{m}$ - $\mathbf{O}_{m}$. These coordinates are readable from the machine control. The transformation matrix from $\mathbf{X}_{t}$ - $\mathbf{Y}_{t}$ - $\mathbf{Z}_{t}$ - $\mathbf{O}_{t}$ to $\mathbf{X}_{s}$ - $\mathbf{Y}_{s}$ - $\mathbf{Z}_{s}$ - $\mathbf{O}_{s}$ is

$$ {}^{s}\mathbf{M}_{t} = \begin{bmatrix} \cos\theta_t & -\sin\theta_t & 0 & 0 \\ \sin\theta_t & \cos\theta_t & 0 & 0 \\ 0 & 0 & 1 & -L_t \\ 0 & 0 & 0 & 1 \end{bmatrix} \tag{3.15} $$

where θ_t is the angle between $\mathbf{X}_t$ and $\mathbf{X}_s$. The transformation matrix from $\mathbf{X}_t$ - $\mathbf{Y}_t$ - $\mathbf{Z}_t$ - $\mathbf{O}_t$ to $\mathbf{X}_m$ - $\mathbf{Y}_m$ - $\mathbf{Z}_m$ - $\mathbf{O}_m$ is

$$ \begin{aligned} {}^{m}\mathbf{M}_{t} &= {}^{m}\mathbf{M}_{s} \cdot {}^{s}\mathbf{M}_{t} \\ &= \begin{bmatrix} \cos(\theta_s+\theta_t) & -\sin(\theta_s+\theta_t) & 0 & X_s \\ \sin(\theta_s+\theta_t) & \cos(\theta_s+\theta_t) & 0 & Y_s \\ 0 & 0 & 1 & Z_s - L_t \\ 0 & 0 & 0 & 1 \end{bmatrix} \end{aligned} \tag{3.16} $$

Therefore, the transformation matrix from $\mathbf{X}_t$ - $\mathbf{Y}_t$ - $\mathbf{Z}_t$ - $\mathbf{O}_t$ to $\mathbf{X}_{ts}$ - $\mathbf{Y}_{ts}$ - $\mathbf{Z}_{ts}$ - $\mathbf{O}_{ts}$ is

$$ \begin{aligned} {}^{ts}\mathbf{M}_{t} &= {}^{ts}\mathbf{M}_{m} \cdot {}^{m}\mathbf{M}_{t} \\ &= \begin{bmatrix} \cos(\theta_s+\theta_t) & -\sin(\theta_s+\theta_t) & 0 & X_s - X_{ts} \\ \sin(\theta_s+\theta_t) & \cos(\theta_s+\theta_t) & 0 & Y_s - Y_{ts} \\ 0 & 0 & 1 & Z_s - L_t - Z_{ts} \\ 0 & 0 & 0 & 1 \end{bmatrix} \end{aligned} \tag{3.17} $$

Before measurement, the tool is positioned so that its center $\mathbf{O}_t$ is offset from the $\mathbf{Z}_{ts}$ axis along the $\mathbf{Y}_{ts}+$ direction by a distance d and $\mathbf{O}_t$ lies on $\mathbf{Y}_{ts}\mathbf{Z}_{ts}$ plane. Eq.(3.17) can be written as

$$ \begin{aligned} {}^{ts}\mathbf{M}_{t} &= {}^{ts}\mathbf{M}_{m} \cdot {}^{m}\mathbf{M}_{t} \\ &= \begin{bmatrix} \cos(\theta_s+\theta_t) & -\sin(\theta_s+\theta_t) & 0 & 0 \\ \sin(\theta_s+\theta_t) & \cos(\theta_s+\theta_t) & 0 & -d \\ 0 & 0 & 1 & Z_s - L_t - Z_{ts} \\ 0 & 0 & 0 & 1 \end{bmatrix} \end{aligned} \tag{3.18} $$

Eq.(3.18) also lays the mathematical ground for tool length measurement. Suppose the coordinate of $\mathbf{O}_t$ in $\mathbf{X}_{ts}$ - $\mathbf{Y}_{ts}$ - $\mathbf{Z}_{ts}$ - $\mathbf{O}_{ts}$ is

$$ {}^{ts}\mathbf{O}_t = \begin{bmatrix} 0 \\ -d \\ Z_h \\ 1 \end{bmatrix} \tag{3.19} $$

and when the tool triggers the tool setter, Eq.(3.19) becomes

$$ {}^{ts}\mathbf{O}'_t = \begin{bmatrix} 0 \\ -d \\ Z_t \\ 1 \end{bmatrix} \tag{3.20} $$

where the apostrophe denotes ${}^{ts}\mathbf{O}_t$ at trigger instant and Z_t denotes the Z coordinates of $\mathbf{O}_t$ in $\mathbf{X}_{ts}$ - $\mathbf{Y}_{ts}$ - $\mathbf{Z}_{ts}$ - $\mathbf{O}_{ts}$ at triggering instant. The coordinate of $\mathbf{O}_t$ in $\mathbf{X}_{ts}$ - $\mathbf{Y}_{ts}$ - $\mathbf{Z}_{ts}$ - $\mathbf{O}_{ts}$ at triggering instant can also be found as

$$ \begin{aligned} {}^{ts}\mathbf{O}'_t &= {}^{ts}\mathbf{M}_t \cdot {}^{t}\mathbf{O}_t \\ &= \begin{bmatrix} \cos(\theta_s+\theta_t) & -\sin(\theta_s+\theta_t) & 0 & 0 \\ \sin(\theta_s+\theta_t) & \cos(\theta_s+\theta_t) & 0 & -d \\ 0 & 0 & 1 & Z'_s - L_t - Z_{ts} \\ 0 & 0 & 0 & 1 \end{bmatrix} \cdot \begin{bmatrix} 0 \\ 0 \\ 0 \\ 1 \end{bmatrix} \\ &= \begin{bmatrix} 0 \\ -d \\ Z'_s - L_t - Z_{ts} \\ 1 \end{bmatrix} \end{aligned} \tag{3.21} $$

where Z'_s is the Z coordinates of $\mathbf{O}_s$ in $\mathbf{X}_m$ - $\mathbf{Y}_m$ - $\mathbf{Z}_m$ - $\mathbf{O}_m$ when the tool triggers the tool setter. This data is recorded and readable from the machine control. Solve Eq.(3.19) and Eq.(3.21) for L_t and we have

$$L_t = Z'_s - Z_{ts} - Z_t \tag{3.22}$$

In conventional on-machine tool setting schemes, Z_t is considered 0 and the tool length L_t equals the difference between Z'_s and Z_{ts}. However, due to the complexity of the geometries in the tool length measurement process, in practice, Z_t does not equal 0 and thus it is the measurement error. To understand the measurement error, detailed modeling and simulations of the measurement process are derived next.

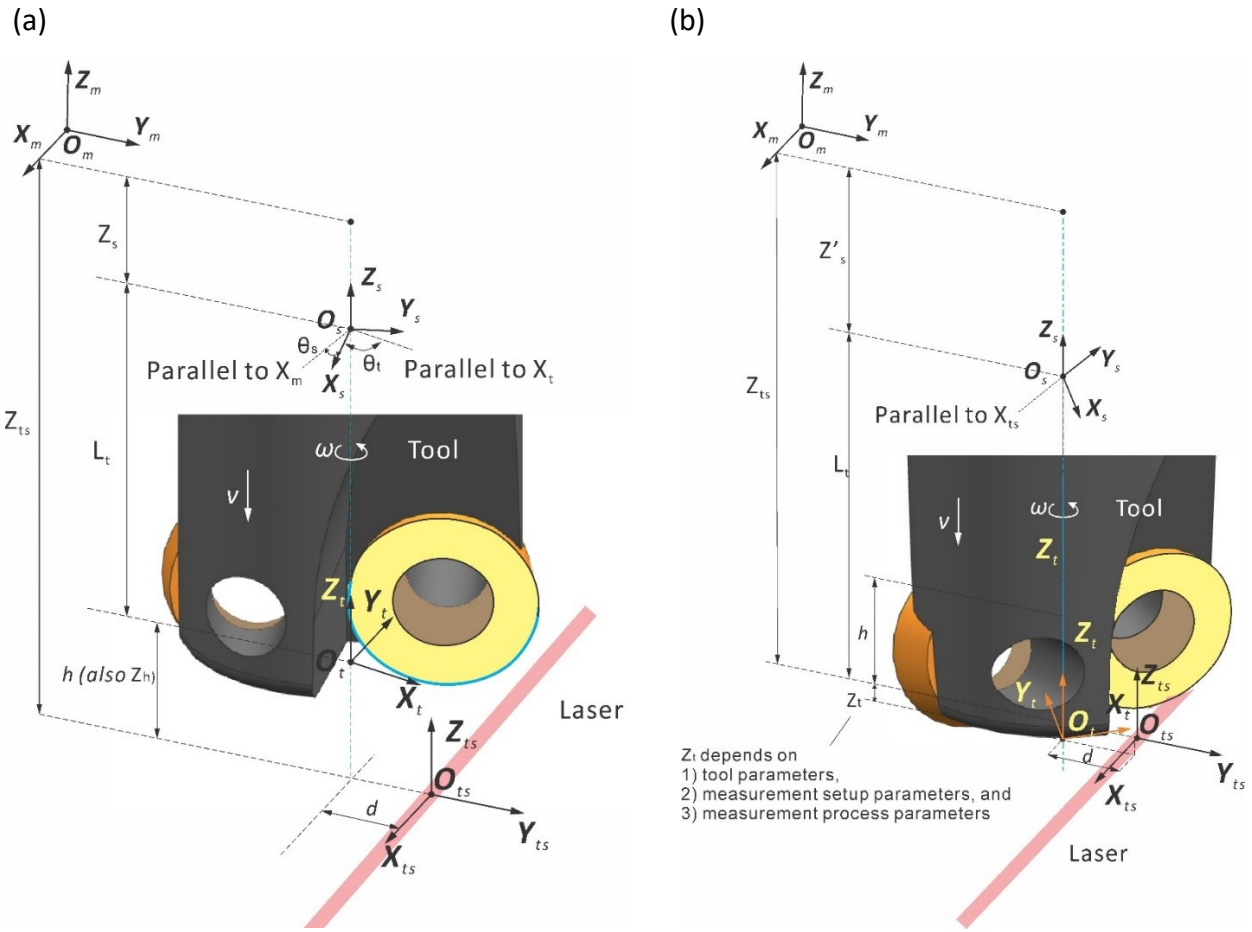

Figure 3.10. Tool length measurement setup.

During measurement, the spindle rotates and feeds towards the beam. A kinematic model is used to describe the instantaneous relationship between the tool and the laser tool setter during measurement. Supposed that the tool rotates at a spindle speed N_s (unit: revolutions per minute, or RPM). Its angular velocity ω (unit: radian) can be calculated as

$$\omega = 2 \cdot \pi \cdot N_s \tag{3.23}$$

and travels with a linear velocity v during measurement. Suppose that the process starts at a level that the coordinate of $\mathbf{O}_t$ in $\mathbf{X}_{ts}$ - $\mathbf{Y}_{ts}$ - $\mathbf{Z}_{ts}$ - $\mathbf{O}_{ts}$ is

$$ {}^{ts}\mathbf{O}^{0}_{t} = \begin{bmatrix} 0 \\ -d \\ h \\ 1 \end{bmatrix} \tag{3.24} $$

At any instant t, the equivalent transformation matrix from $\mathbf{X}_t$ - $\mathbf{Y}_t$ - $\mathbf{Z}_t$ - $\mathbf{O}_t$ to $\mathbf{X}_{ts}$ - $\mathbf{Y}_{ts}$ - $\mathbf{Z}_{ts}$ - $\mathbf{O}_{ts}$ is (see Figure 3.10(b))

$$ {}^{ts}\mathbf{M}^{i}_{t} = \begin{bmatrix} \cos(\omega \cdot t + \theta_t + \theta_{s0}) & -\sin(\omega \cdot t + \theta_t + \theta_{s0}) & 0 & 0 \\ \sin(\omega \cdot t + \theta_t + \theta_{s0}) & \cos(\omega \cdot t + \theta_t + \theta_{s0}) & 0 & -d \\ 0 & 0 & 1 & h - v \cdot t \\ 0 & 0 & 0 & 1 \end{bmatrix} \tag{3.25} $$

The parametric equation of the cutting edge of the k th insert, at any instant, in $\mathbf{X}_{ts}$ - $\mathbf{Y}_{ts}$ - $\mathbf{Z}_{ts}$ - $\mathbf{O}_{ts}$ can be expressed as

$$ {}^{ts}\mathbf{EK} = {}^{ts}\mathbf{M}^{i}_{t} \cdot {}^{t}\mathbf{EK} \tag{3.26} $$

and the parametric equation of the flank face of the k th insert, at any instant, in $\mathbf{X}_{ts}$ - $\mathbf{Y}_{ts}$ - $\mathbf{Z}_{ts}$ - $\mathbf{O}_{ts}$ can be expressed as

$$ {}^{ts}\mathbf{FSK} = {}^{ts}\mathbf{M}^{i}_{t} \cdot {}^{t}\mathbf{FSK} \tag{3.27} $$

The tool center $\mathbf{O}_t$, at any instant, in $\mathbf{X}_{ts}$ - $\mathbf{Y}_{ts}$ - $\mathbf{Z}_{ts}$ - $\mathbf{O}_{ts}$ is

$$ {}^{ts}\mathbf{O}^{i}_{t} = \begin{bmatrix} 0 \\ -d \\ h - v \cdot t \\ 1 \end{bmatrix} \tag{3.28} $$

If the tool triggers the laser tool setter at $t^{'}$, since at the trigger instant, $\mathbf{O}_t$ in $\mathbf{X}_{ts}$ - $\mathbf{Y}_{ts}$ - $\mathbf{Z}_{ts}$ - $\mathbf{O}_{ts}$ is given by Eq.(3.19), then

$$ Z_t = h - v \cdot t^{'} \tag{3.29} $$

3.4.2 Geometric model establishment for simulation of mill length measurement

The overlapping area ***S*** between the cutter insert projection ***IKp*** and the projection of the laser beam ***Bp*** on the photodiode plane determines whether the laser tool setter is triggered by the tool (See Figure 3.11). The photodiode plane is perpendicular to the laser axis. If the overlapping area ***S*** is larger than 50% of the laser beam projected area, the laser tool setter will be triggered. Therefore, there are three steps to check if the tool triggers the tool setter: 1) the projected shapes of the insert ***IKp***, and the laser beam, ***Bp***, on the photodiode plane should first be derived; 2) Check if the projected shapes overlap and calculate their overlapping area (if there is any); and 3) The overlapping area should be compared with 50% of the laser beam projection area.

To find the projected shapes of the insert ***IKp***, and the laser beam, ***Bp***, on the photodiode plane, a coordinate system $\mathbf{X}_{pd}$ - $\mathbf{Y}_{pd}$ - $\mathbf{Z}_{pd}$ - $\mathbf{O}_{pd}$ is established at the photodiode plane with the

origin $\mathbf{O}_{pd}$ on the laser axis and the $\mathbf{X}_{pd}$ axis along the laser axis (see Figure 3.11). Suppose the laser beam is also along the $\mathbf{X}_{ts}$, and the photodiode plane is selected at a distance L_d from $\mathbf{O}_{ts}$. A coordinate system $\mathbf{X}_{pd}$-$\mathbf{Y}_{pd}$-$\mathbf{Z}_{pd}$-$\mathbf{O}_{pd}$ can be established by translating $\mathbf{X}_{ts}$-$\mathbf{Y}_{ts}$-$\mathbf{Z}_{ts}$-$\mathbf{O}_{ts}$ along the laser axis by distance L_{pd}. The equivalent transformation matrix from $\mathbf{X}_{ts}$-$\mathbf{Y}_{ts}$-$\mathbf{Z}_{ts}$-$\mathbf{O}_{ts}$ to $\mathbf{X}_{pd}$-$\mathbf{Y}_{pd}$-$\mathbf{Z}_{pd}$-$\mathbf{O}_{pd}$ is

$$ {}^{pd}\mathbf{M}_{ts} = \begin{bmatrix} 1 & 0 & 0 & -L_{pd} \\ 0 & 1 & 0 & 0 \\ 0 & 0 & 1 & 0 \\ 0 & 0 & 0 & 1 \end{bmatrix} \tag{3.30} $$

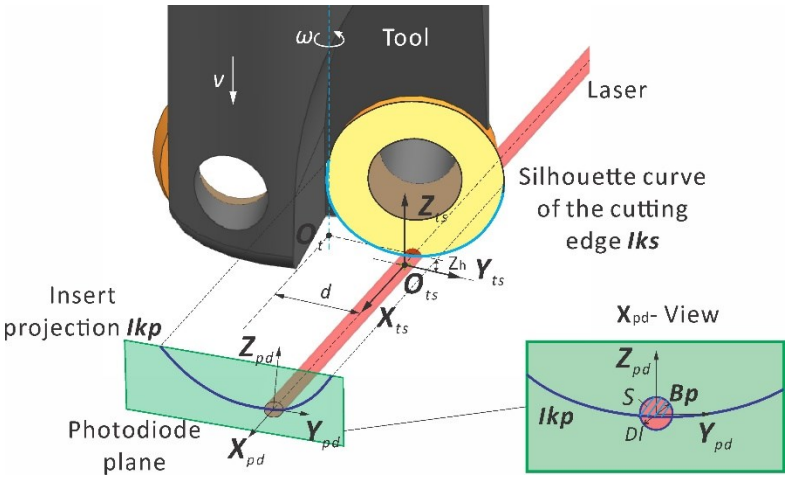

Figure 3.11. Geometric simulation of tool length measurement of an indexable mill.

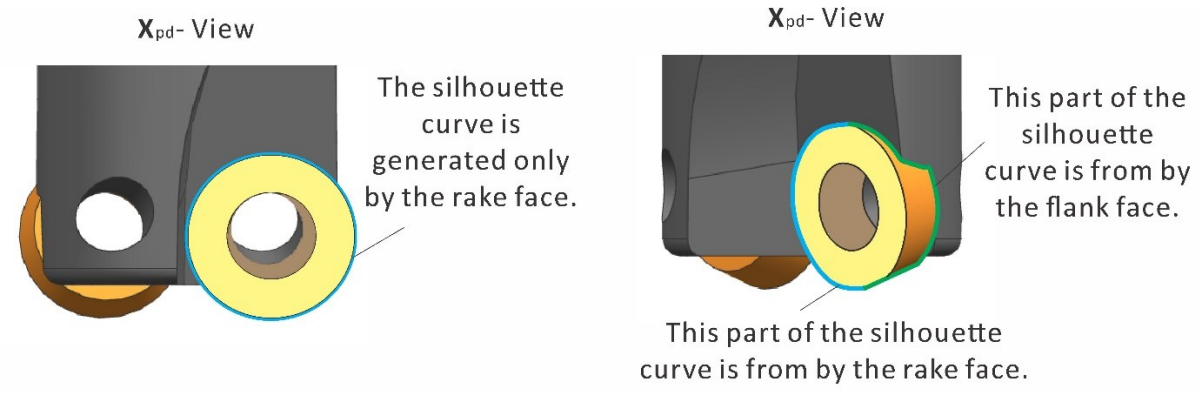

Figure 3.12. Formulation of the silhouette curve of an insert.

The projection of the insert on the photodiode plane is derived by first taking the calculating the silhouette curves of the insert along the laser beam direction ***IKs*** in $\mathbf{X}_{pd}$ - $\mathbf{Y}_{pd}$ - $\mathbf{Z}_{pd}$ - $\mathbf{O}_{pd}$ and then projecting the silhouette curves ***IKs*** on the photodiode plane (See Figure 3.12). The silhouette curves of an insert are formed by the rake face or by the rake face and the flank face together (See Figure 3.12). Since the goal is to find the projected shape of the insert on the photodiode plane, this shape can easily be found by using Boolean combine operations of the projected shapes of the rake face and the flank face. This way avoids the complex calculation of exact silhouette curves. Instead, the silhouette curves of the rake face and the flank face are calculated and their enclosed polygons are combined. In this research, the rake face is represented by a plane and thus, its silhouette curve is generated by the cutting edge. Therefore, the projection of the k th cutting edge, at any instant, in $\mathbf{X}_{pd}$ - $\mathbf{Y}_{pd}$ - $\mathbf{Z}_{pd}$ - $\mathbf{O}_{pd}$ is

$$ {}^{\mathrm{pd}}\mathbf{EKp} = \begin{bmatrix} 0 & 0 & 0 & 0 \\ 0 & 1 & 0 & 0 \\ 0 & 0 & 1 & 0 \\ 0 & 0 & 0 & 1 \end{bmatrix} \cdot {}^{\mathrm{pd}}\mathbf{M}_{\mathrm{ts}} \cdot {}^{ts}\mathbf{M}^{i}_{\mathrm{t}} \cdot {}^{t}\mathbf{EK} \tag{3.31} $$

The flank face is represented by a conic face and according to the projection direction $\mathbf{X}_{\mathrm{pd}}$, the silhouette curve of the flank surface satisfies the following equation,

$$ {}^{pd}\mathbf{N} \cdot {}^{pd}\mathbf{X}_{pd} = 0 \tag{3.32} $$

where ${}^{pd}\mathbf{N}$ is the normal vector of surfaces ${}^{pd}\mathbf{FSK}$ in $\mathbf{X}_{\mathrm{pd}}\text{-}\mathbf{Y}_{\mathrm{pd}}\text{-}\mathbf{Z}_{\mathrm{pd}}\text{-}\mathbf{O}_{\mathrm{pd}}$. ${}^{pd}\mathbf{N}$ can be calculated as

$$ {}^{pd}\mathbf{N} = \frac{\partial\, {}^{pd}\mathbf{FSK}(\alpha, th)}{\partial \alpha} \times \frac{\partial\, {}^{pd}\mathbf{FSK}(\alpha, th)}{\partial th} \tag{3.33} $$

and

$$ {}^{pd}\mathbf{FSK} = {}^{\mathrm{pd}}\mathbf{M}_{\mathrm{ts}} \cdot {}^{ts}\mathbf{M}^{i}_{\mathrm{t}} \cdot {}^{t}\mathbf{FSK} \tag{3.34} $$

Eq. (3.32) is an implicit equation, a numerical method is applied to calculate the parameters (α, th) of many points on the silhouette curve, and the parameters are substituted into Eq.(3.33) to calculate the point coordinates in $\mathbf{X}_{\mathrm{pd}}\text{-}\mathbf{Y}_{\mathrm{pd}}\text{-}\mathbf{Z}_{\mathrm{pd}}\text{-}\mathbf{O}_{\mathrm{pd}}$. By connecting these points, the silhouette curve of the flank face ${}^{\mathrm{pd}}\mathbf{FSK}$ is determined and the projection of the silhouette of the flank face on the photodiode plane is

$$ {}^{\mathrm{pd}}\mathbf{FSKp} = \begin{bmatrix} 0 & 0 & 0 & 0 \\ 0 & 1 & 0 & 0 \\ 0 & 0 & 1 & 0 \\ 0 & 0 & 0 & 1 \end{bmatrix} \cdot {}^{\mathrm{pd}}\mathbf{FSK} \tag{3.35} $$

Since the projection of the laser beam the photodiode plane is a circle, its parametric equation in $\mathbf{X}_{pd}$ - $\mathbf{Y}_{pd}$ - $\mathbf{Z}_{pd}$ - $\mathbf{O}_{pd}$ can be written as (see Figure 3.11)

$$^{pd}\mathbf{Bp} = \begin{bmatrix} 0 \\ \frac{D_l}{2} \cdot \cos\theta_l \\ \frac{D_l}{2} \cdot \sin\theta_l \\ 1 \end{bmatrix}, \theta_l \in [0, 360\,\text{deg}] \tag{3.36}$$

where D_l is the diameter of the laser beam.

The shaded region S is bounded by boundary **Bp** and the insert projection ***IKs*** on the receiver screen (see Figure 3.11). Boundaries **Bp** is represented with a polygon Poly_{Bp}. The insert projection ***IKs*** is presented with a polygon Poly_{IKs}. A well-established method of calculating polygon intersection can be applied and the intersection between polygons Poly_{Bp} and Poly_{IKs} is found. Additionally, Poly_{IKs} is formed by calculating the combination of a polygon enclosed by $^{pd}\mathbf{EKp}$ and $^{pd}\mathbf{FSKp}$. The boundary polygon Poly_S of the shaded region S is obtained by trimming polygons Poly_{Bp} and Poly_{IKs}. Suppose the vertices of the polygon Poly_S are $(y_1, z_1), (y_2, z_2), \ldots,$ (y_n, z_n). The area of the shaded region S can be calculated as

$$Sa = \frac{1}{2} \cdot \left(\begin{vmatrix} y_1 & y_2 \\ z_1 & z_2 \end{vmatrix} + \begin{vmatrix} y_2 & y_3 \\ z_2 & z_3 \end{vmatrix} + \ldots + \begin{vmatrix} y_m & y_1 \\ z_m & z_1 \end{vmatrix} \right) \tag{3.37}$$

The circular area of the laser beam projection can be calculated as

$$Sa_{Bp} = \left(\frac{D_l}{2}\right)^2 \cdot \pi \tag{3.38}$$

The ratio between the area of the shaded region and the circular area is

$$\eta = \frac{Sa}{Sa_{Bp}} \tag{3.39}$$

If the ratio η is larger than 50%, then the laser tool setter is considered to be triggered.

In summary, the measurement process can be simulated in the following manner: Starting from the location defined by h, the tool rotates and moves towards the laser beam during measurement. By monitoring the time t' when the ratio η becomes larger than 50%, the tool triggers the tool setter and $\mathbf{O}_t$ in $\mathbf{X}_{ts}\text{-}\mathbf{Y}_{ts}\text{-}\mathbf{Z}_{ts}\text{-}\mathbf{O}_{ts}$ is given by Eq.(3.29).

3.5 New discovery: tool length characteristic curve for length measurement of round-insert mills

Laser tool setter has been available for 15 years; however, little research on mill length measurement has been carried out, and the commercial measurement software has low measurement accuracy and efficiency. The main reason is that the research method is empirical, and the relationship between the measurement error and measurement parameters is simply regarded as unknown and random. In this research, every measuring parameter is set, every step of measuring the mill length is precisely simulated by using the above models with our computer software, and the relationship is determined. By analyzing the simulation results, the tool length characteristic curve is discovered. Based on this characteristic curve, an accurate and efficient approach to measuring lengths of mills with round inserts and bottom cutting edge wear.

3.5.1 Measuring simulations and tool length characteristic curve

Based on the above kinematics and geometric fundamentals of measuring the length of a round insert mill, measuring simulations of two tools are presented in three examples. In practice, the tool length is unknown and should be measured. When the tool is located at a certain level above the laser tool setter during measurement, the spindle angle θ_s cannot be determined prior to tool measurement. In these examples, the tool starts at the same level with different

initial spindle angle θ_{s0} , and the measurement processes are simulated using methods described in Section 4 and we plot the measurement error Z_t against the initial spindle angle θ_{s0} .

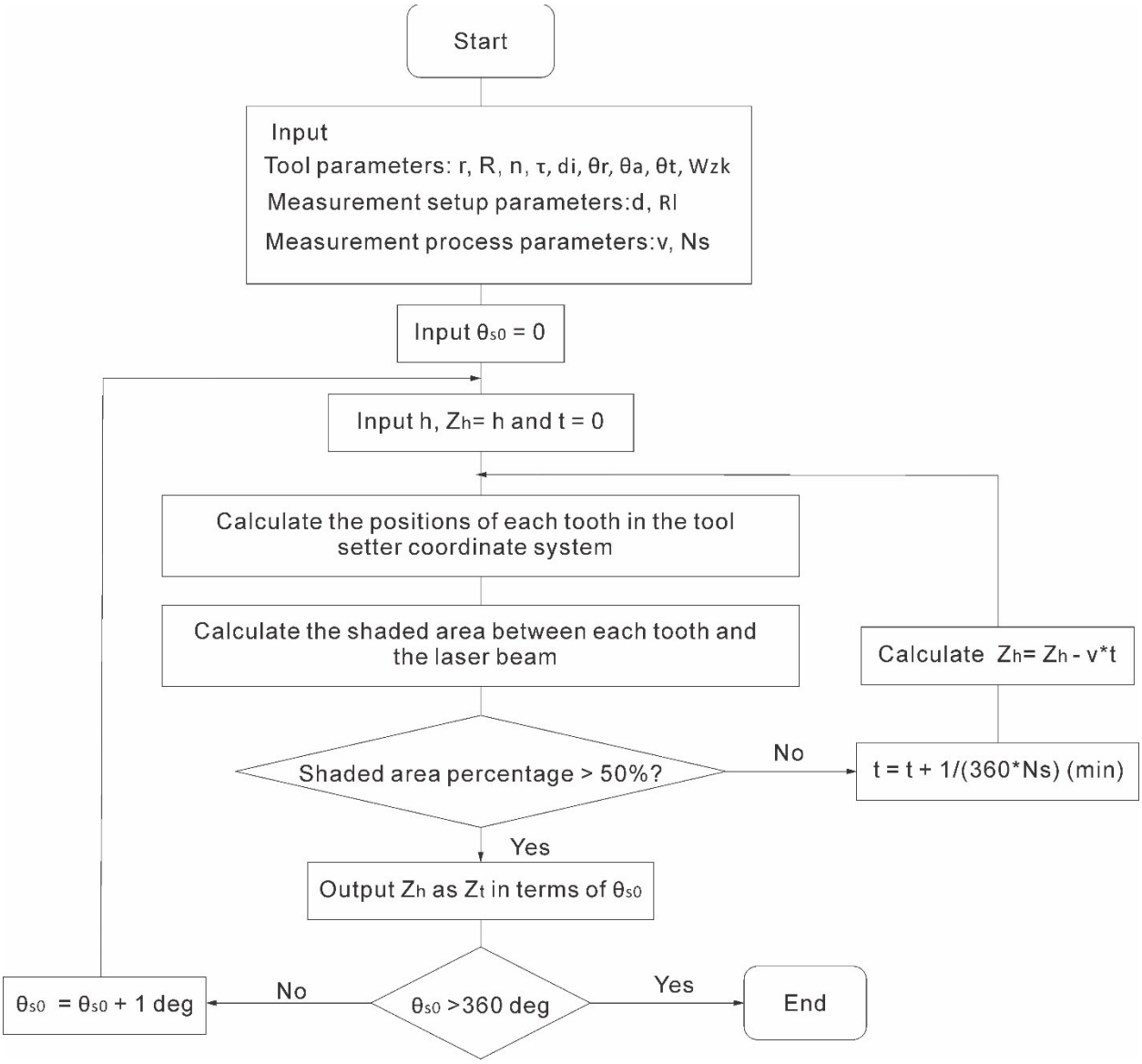

Figure 3.13. The flowchart of the simulations.

The steps for simulations are described in the flowchart shown in Figure 3.13. The simulation programs are prepared in MATLAB. In the beginning, the tool parameters (including the tool wear of each tooth), the measurement setup parameters, and the measurement process parameters are input. The initial spindle angle θ_{s0} is set at 0 degree. The initial height h is set randomly. The current Z coordinates of $\mathbf{O}_t$ in $\mathbf{X}_{ts}$ - $\mathbf{Y}_{ts}$ - $\mathbf{Z}_{ts}$ - $\mathbf{O}_{ts}$, Z_h, is initialized to equal h and the time t is reset at 0. Then for each θ_{s0}, the positions of each tooth in $\mathbf{X}_{ts}$ - $\mathbf{Y}_{ts}$ - $\mathbf{Z}_{ts}$ - $\mathbf{O}_{ts}$ are calculated. The shaded areas between each tool and the laser beam are found. If the shaded area is larger than 50% of the shaded area, the current Z_h, is output as Z_t and is plotted against θ_{s0} on a graph. Otherwise, the time increases and the tool position in $\mathbf{X}_{ts}$ - $\mathbf{Y}_{ts}$ - $\mathbf{Z}_{ts}$ - $\mathbf{O}_{ts}$ is updated and the iteration begins again. Z_t for each θ_{s0} (varying from 0 to 359 degree) are simulated in this manner.

Example 1: A two flute tool with no tool wear.

A two-insert mill cutter whose specification is given (see Table 3.1). The measurement setup parameters are also given in Table 3.1. The spindle speed N_s is set at 1000 rpm and the feed rate v is set at 30 mm/min. To save computation time, the initial height h is set at 0mm.

Table 3.1.The specification of a two-insert mill cutter and its measurement setup.

Insert mill cutter parameters	Symbols	Values
Tool radius	r	10 mm

Insert radius	R	6 mm
Number of flutes	n	2
Flute wear of each tooth	W_{zk}	0 mm
Clearance angle	τ	15 degree
Angle between $\mathbf{X}_t$ and $\mathbf{X}_s$	θ_t	0 degree
Insert thickness	d_i	3.97 mm
Insert radial angle	θ_r	-8 degree
Insert axial angle	θ_a	-5 degree
Measurement setup parameters	Symbols	Values
Radial offset distance	d	4 mm
Laser beam radius	R_l	0.2 mm

Figure 3.14 shows a few iterations before the laser beam is triggered by the tool with $\theta_{s0} = 0\text{deg}$. As can be seen, at each moment, the tool locates at different positions with different spindle angles. As result, the tooth projections have different shapes at each moment and the shaded area changes accordingly. Specifically, when the tool is positioned at $Z_h = -0.0025mm$ in $\mathbf{X}_{ts}$ - $\mathbf{Y}_{ts}$ - $\mathbf{Z}_{ts}$ - $\mathbf{O}_{ts}$, there is no shaded area on the projected plane, and thus the tool does not trigger the tool setter (see Figure 3.14(a)). As the rotating tool feeds towards the beam, it blocks some of the beam at $Z_h = -0.005mm$ but it is not enough to trigger the tool setter (see Figure 3.14 (b)). Finally, when the tool reaches $Z_h = -0.0065mm$, it also turns to an angle that blocks more than 50% of the beam and therefore triggers the tool setter and $Z_h = -0.0065mm$ is output as Z_t (see Figure 3.14 (c)).

The outputs Z_t for all the initial spindle angles θ_{s0} are plotted in Figure 3.15. The figure shows that when starting at $h = 1mm$ and, the initial spindle angle $\theta_{s0} = 94^\circ$ [illegible], the maximum measurement error would occur, $Z_{t,\max} = -0.0135mm$. On the other hand, if the initial spindle angle $\theta_{s0} = 69^\circ$ [illegible], the minimum measurement error would occur, $Z_{t,\min} = -0.0014mm$.

(a)

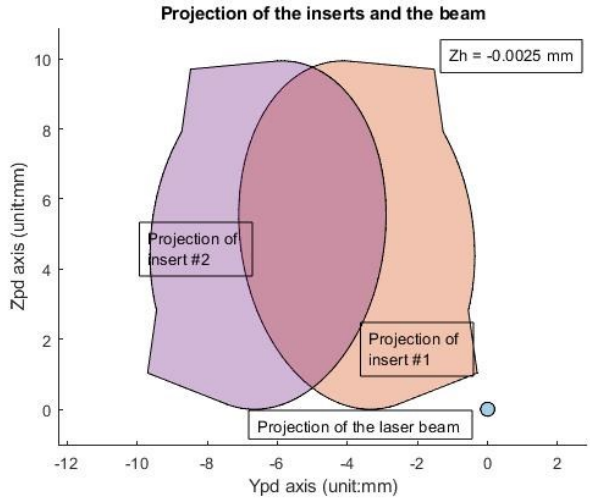

(b)

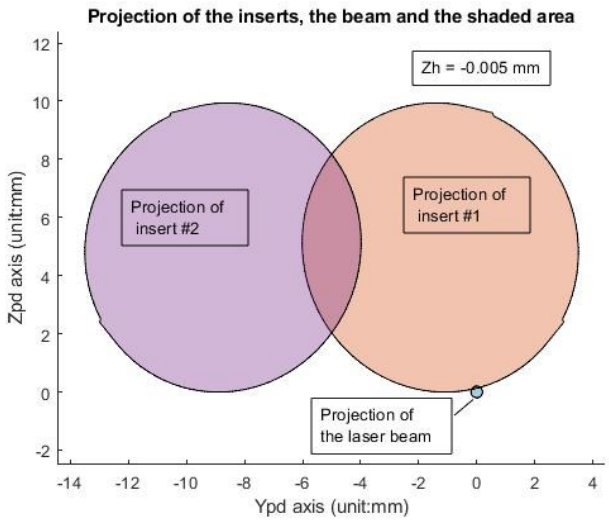

(c)

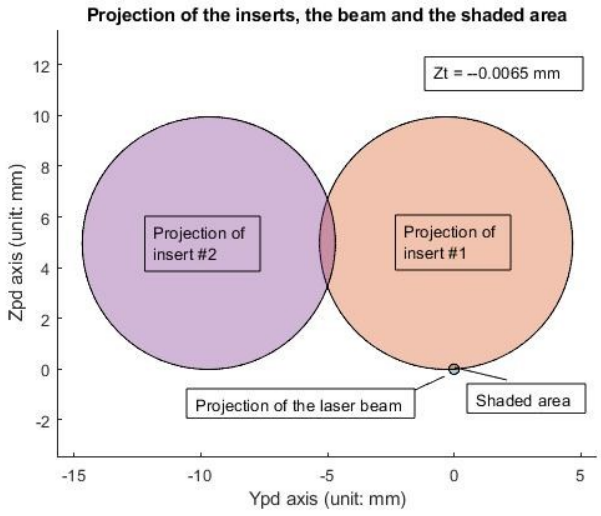

Figure 3.14. Measurement simulations were performed for the tool in example 1. (a) The projections of the inserts and the beam at Zt=-0.0025mm; (b) The projections of the inserts, the beam, and the shaded area at Zt=-0.005mm; and (c) The projections of the inserts, the beam and the shaded area when the tool triggers the laser tool setter.

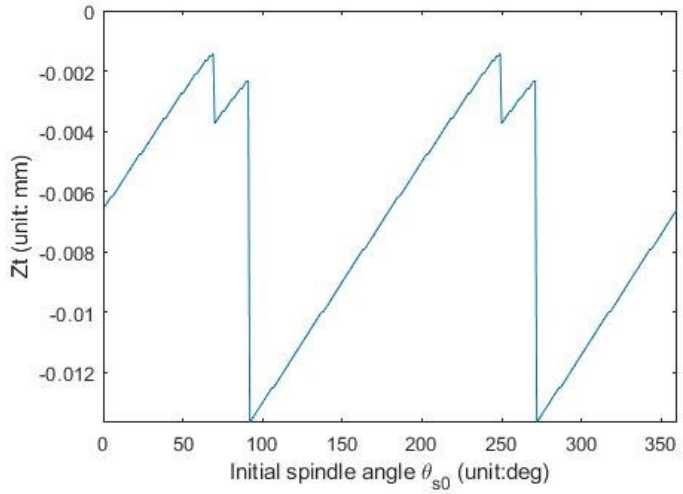

Figure 3.15. Simulation outputs for the tool in example 1 with $h = 0mm$.

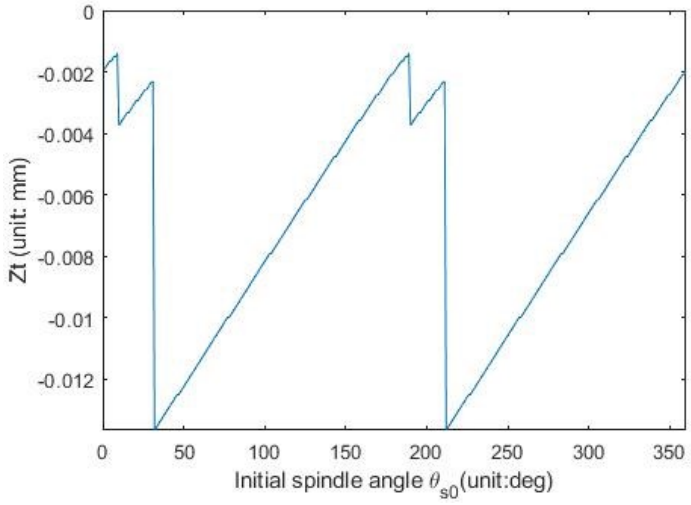

Figure 3.16. Simulation outputs for the tool in example 1 with $h = 0.005mm$.

To further examine the simulation outputs, the program was run again with the initial height $h = 0.005mm$ and other parameters remaining the same. The outputs Z_t for all the initial

spindle angles θ_{s0} are plotted in Figure 3.17. The figure shows that when starting at $h = 0.005mm$ and, the initial spindle angle $\theta_{s0} = 33^\circ$ [illegible], the maximum measurement error would occur, $Z_{t,\max} = -0.0135mm$. On the other hand, if the initial spindle angle $\theta_{s0} = 9^\circ$ [illegible], the minimum measurement error would occur, $Z_{t,\min} = -0.0014mm$. The above results indicate that although the initial height is different, the maximum and minimum measurement errors are the same. Comparing Figure 3.15 and Figure 3.16 , the intervals of the initial spindle angle that generate two maximum (or minimum) measurement errors are 180° in both figures. The patterns of both plotted curves are the same, with the plot on the second figure switched a phase angle to the right from the first figure.

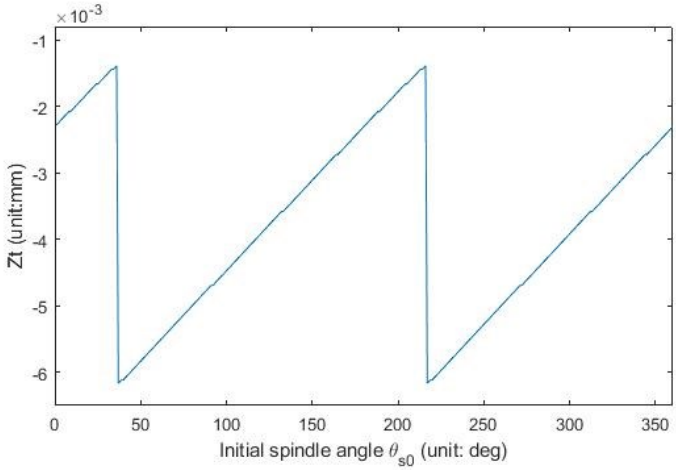

Figure 3.17. Simulation outputs for the tool in example 1 with $Ns = 1000rpm$ and $v = 10mm/\min$.

The measurement process parameters would alter the simulation outputs. To demonstrate this, the program was run again with the spindle speed N_s is set at 1000 rpm and the feed rate

v is set at 10 mm/min. The figure shows that the maximum measurement error is $Z_{t,\max} = -0.0061mm$ and the minimum measurement error is $Z_{t,\min} = -0.0014mm$. The intervals of the initial spindle angle that generate two maximum (or minimum) measurement errors are still 180°. This is reasonable because the feed rate is 1/3 of the previous run.

Example 2: A two flute tool with tool wear.

The results from the last example show that there are two minimum measurement errors corresponding to certain initial spindle angles. These two minimum measurement errors have the same magnitude. The reason for this is that the two flutes of the tool have the same height and the two minimum measurement errors are generated by the two flutes respectively. This example shows the case where the two flutes have different heights, i.e. one flute has worn out more than the other one.

The specification of the two-insert mill cutter and the measurement setup parameters are given in Table 3.1. The wear of the second tooth $W_{z2} = 0.005mm$. The spindle speed N_s is set at 1000 rpm and the feed rate v is set at 30 mm/min. The initial height h is set at 0mm.

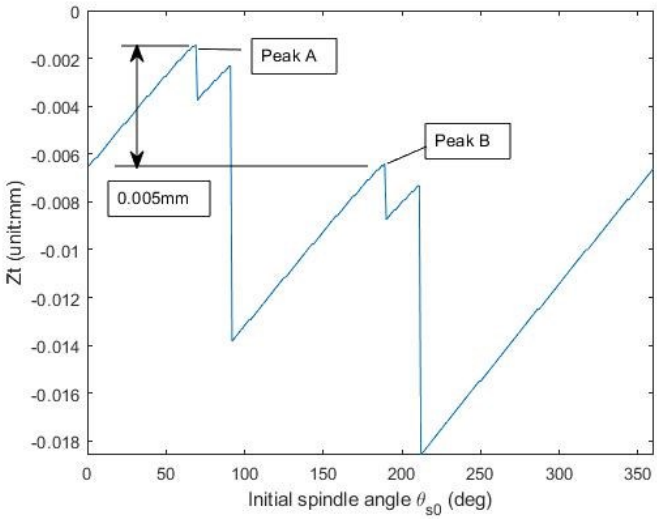

Figure 3.18. Simulation outputs for the tool in example 2.

The outputs Z_t for all the initial spindle angles θ_{s0} are plotted in Figure 3.18. Two peaks (peak A and peak B) can be seen in the figure. The two peaks are generated by the two flutes, respectively. The difference between the corresponding Z_t of these two peaks equals the wear of the flute W_{z2}.

Example 3: A three flute tool with tool wear

Table 3.2. The specification of a three-insert mill cutter and its measurement setup.

Insert mill cutter parameters	Symbols	Values
Tool radius	r	12 mm
Insert radius	R	5 mm
Number of flutes	n	3
Clearance angle	τ	15 degree
Angle between $\mathbf{X}_t$ and $\mathbf{X}_s$	θ_t	0 degree
Insert thickness	d_i	3.97 mm

Insert radial angle	θ_r	-8 degree
Insert axial angle	θ_a	-5 degree

The example performs the measurement simulation for a three-insert mill cutter with tool wear. The specifications of the cutter are given in Table 3.2. The wear of the second tooth $W_{z2} = 0.006mm$ and $W_{z3} = 0.01mm$. The spindle speed N_s is set at 500 rpm and the feed rate v is set at 30 mm/min. The initial height h is set at 0mm.

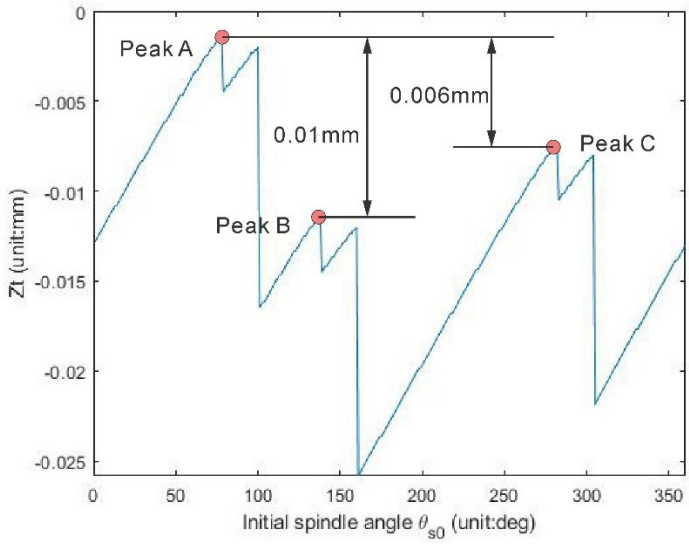

Figure 3.19. Simulation outputs for the tool in example 3.

The outputs Z_t for all the initial spindle angles θ_{s0} are plotted in Figure 3.19. There are three peaks (peak A, peak B, and peak C) in the figure. These peaks are generated by the three flutes. The difference between the corresponding Z_t of peak A and peaks B equals to $W_{z3} = 0.01mm$ and the difference between the corresponding Z_t of peak A and peaks C equals to $W_{z2} = 0.006mm$.

From the above three examples, a curve that corresponds to the current Z coordinates of $\mathbf{O}_t$ in $\mathbf{X}_{ts}$ - $\mathbf{Y}_{ts}$ - $\mathbf{Z}_{ts}$ - $\mathbf{O}_{ts}$ at the triggering instant, Z_t and the initial spindle angle θ_{s0} can be plotted for any given tool measured at the given spindle speed and feed rate. In this research, we define this curve as the tool length characteristic curve. For on-machine tool measurement, each tool is accompanied by a distinct tool length characteristic curve. Three distinct characteristics can be observed from the curve: 1) A set of peaks and troughs are present in the curve in a periodic manner. For the same tool, if the initial height of the measurement processes changes, the tool length characteristic curve shifts by a phase angle to the left or the right. 2) For the same tool, the measuring feed rate and the spindle speed change the span of the characteristic curve in the Z_t direction but the spindle angle differences between the peaks and troughs remain the same. 3) The number of peaks is defined by the number of teeth and their wear. In most cases, the number of peaks equals the number of teeth. In some cases, if the wear of a tooth is larger than 1 feed per tooth, then the peak created by this tooth would not appear on the curve.

3.5.2 Development of an accurate and efficient tool length measurement method

Using the above tool length characteristic curve, an accurate and efficient tool length measurement method can be developed using curve fitting methods. The flow chart of the developed method is shown in Figure 3.20.

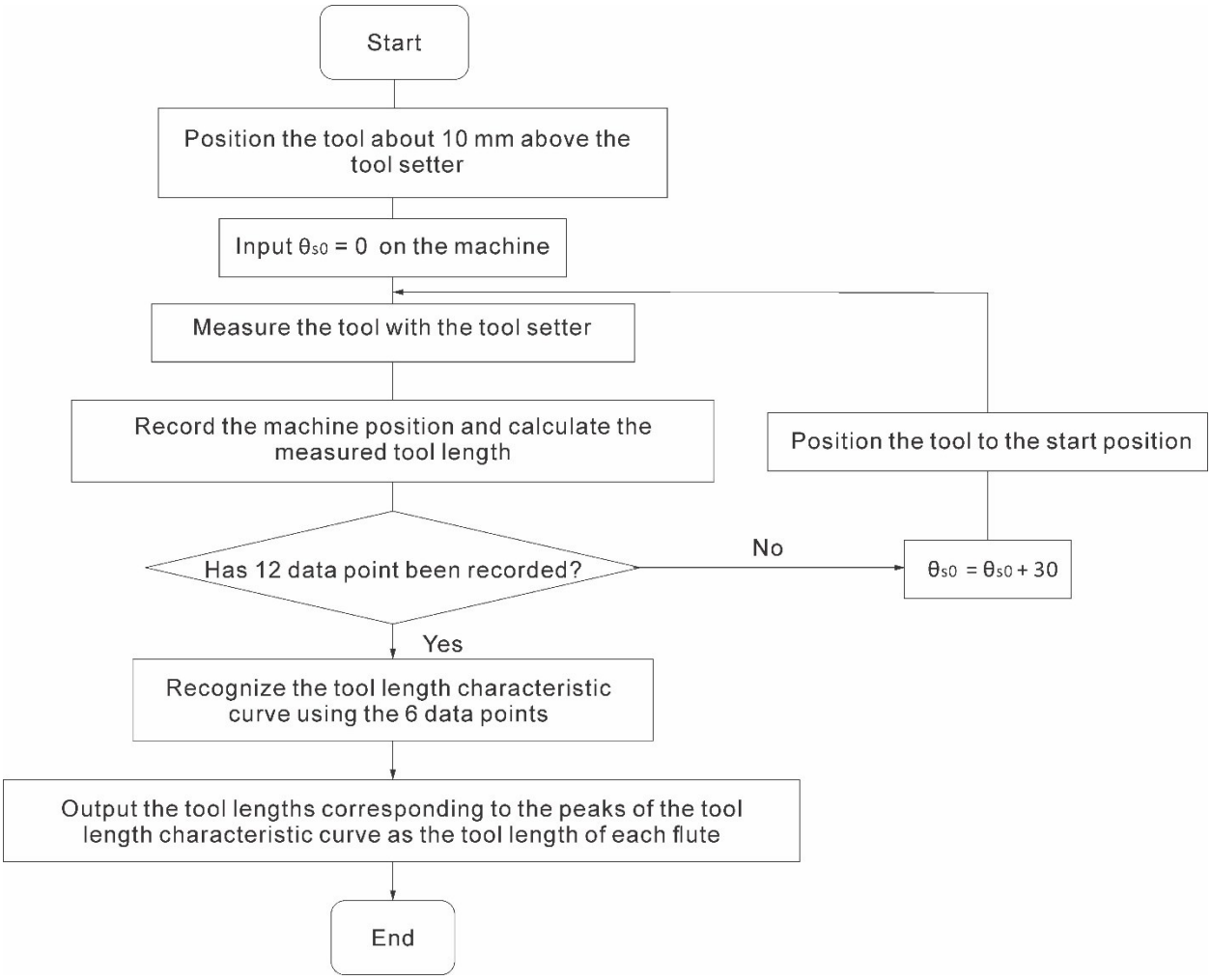

Figure 3.20. The flowchart of the developed method.

On a CNC machine, the tool is positioned at a level above the tool setter before tool measurement. The initial spindle angle can be set via a numerical control (NC) command. Starting with different initial spindle angles, twelve measured tool lengths can be obtained. Connecting the measured data with lines, the obtained data can be used to create a curve that follows the pattern of the tool length characteristic curve. After the tool length characteristic curve is

recognized, the peaks of the tool length characteristic curve represent the length of each flute and they are output accordingly.

3.6 Applications

A salient feature of the proposed approach is that the tool length measurement error is minimized when the tool length characteristics curve is recognized. A higher measurement efficiency can be achieved because the tool length characteristic curve eliminates the measurement uncertainties due to the rotation of the tool. Additionally, the measurement speed is allowed to be very aggressive and the spindle speed can be used as the ones in machining operations. In this section, experiments were carried out to verify this approach and to demonstrate its advantage of this new approach.

To verify the tool length characteristics curve, an experiment was conducted. In this experiment, the tool length characteristics curve of a tool with a known dimension is obtained on a CNC machine and it is also calculated with the measurement simulation proposed in the last section. The measured tool length characteristics curve is compared with the simulated tool length characteristics curve to demonstrate the validity. The tool used is a two-insert mill cutter whose dimensions are measured on an optical tool pre-setter. Its dimensions are listed in Table 3.3 and the tool is shown in Figure 3.21. The measurement setup and measurement process parameters are listed in Table 3.4. 12 tool length data points corresponding to the initial spindle

angles are obtained on a machine during the experiments. The initial spindle angles for each data point is uniformly distributed in the range of 0 degree to 360 degree. The experiment was carried out on a Bridgeport 3-axis machining center (see Figure 3.22).

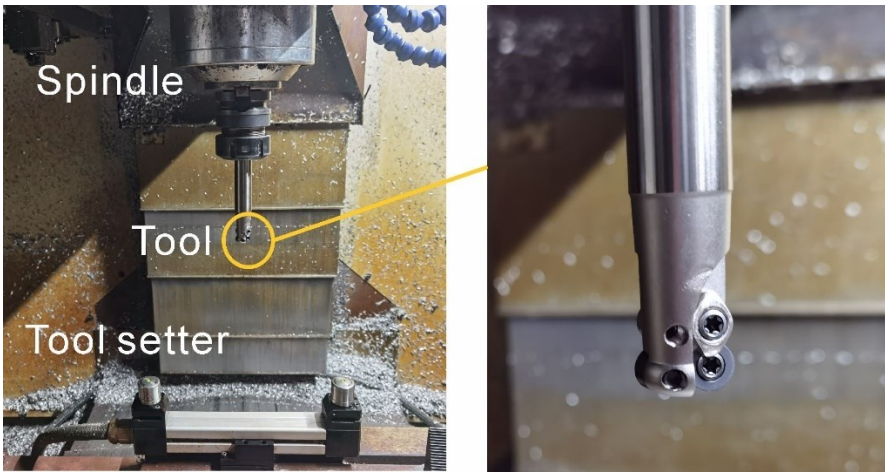

Figure 3.21. The tool is to be measured on the laser tool setter.

Figure 3.22. The machine used for the experiment: Bridgeport 3-axis machining center.

Table 3.3. The specification of a two-insert mill cutter.

Insert mill cutter parameters	Symbols	Values
Tool radius	r	10 mm
Insert radius	R	5 mm
Number of flutes	n	2
Tool length	L_t	176.641 mm
Flute wear of each tooth	W_{zk}	0.002 mm
Clearance angle	τ	15 degree
Angle between $\mathbf{X}_t$ and $\mathbf{X}_s$	θ_t	140 degree
Insert thickness	d_i	3.2 mm
Insert radial angle	θ_r	-12 degree
Insert axial angle	θ_a	6 degree

Table 3.4. The measurement setup parameters and the measurement process parameters.

Measurement setup parameters	Symbols	Values
Radial offset distance	d	4.9 mm
Laser beam radius	R_l	0.2 mm
Z-coordinates of $\mathbf{O}_{ts}$ in $\mathbf{X}_m$ - $\mathbf{Y}_m$ - $\mathbf{Z}_m$ - $\mathbf{O}_m$	$\mathbf{O}_{ts}$	-1172.015 mm
Initial height before measurement	h	5 mm
Measurement setup parameters	**Symbols**	**Values**
Spindle speed	N_s	1000 rpm
Feed rate	v	30 mm/min

The results of the experiment are plotted in Figure 3.23. In the figure, the red dots are the measured data points. The vertical axis represents the measured tool length and the horizontal axis represents the initial spindle angle. By connecting the measured tool lengths, a tool length characteristic curve is formed (represented by the solid blue curve). The simulated tool length

characteristic curve is also plotted (represented by the solid orange curve). The vertical axis of the simulated tool length characteristic curve represents the $\mathbf{O}_t$ in $\mathbf{X}_{ts} - \mathbf{Y}_{ts} - \mathbf{Z}_{ts} - \mathbf{O}_{ts}$ at the trigger instant. Thus, the tool length measured on the optical tool presetter is added to the values of the vertical axis of the simulated tool length characteristic curve so that they match with those tool lengths measured on a machine. As can be seen from Figure 3.23, the simulated and the measured tool length characteristic curve have similar patterns, where two peaks A and B, and two valleys can be recognized. Specifically, the measured tool length characteristic curve shows two peaks that correspond to the two peaks (marked by A and B) of the simulated tool length characteristic curve. The maximum of the measured tool length characteristic curve is 176.639 mm (at peak B) and the maximum of the simulated tool length characteristic curve is 176.640 mm (at peak B). The maximum tool length represents the tool length of the tool measured on the laser tool setter. The tool length measured on the optical tool presetter is 176.641 mm, which is only 2 microns different from the on-machine measured results. This shows the proposed method is accurate. Additionally, peak A represents the tool length of the second flute. As can be seen, the simulated tool length at peak A is 176.637mm and the measured tool length at peak A is 176.636 mm which are also very similar. Comparing peak A and peak B, the difference for the simulated curve is 0.003mm and the difference for the measured curve is also 0.003mm. This difference represents the tool length difference between the two flutes, which was measured as 0.002mm on the tool presetter. This further suggests the proposed method is accurate.

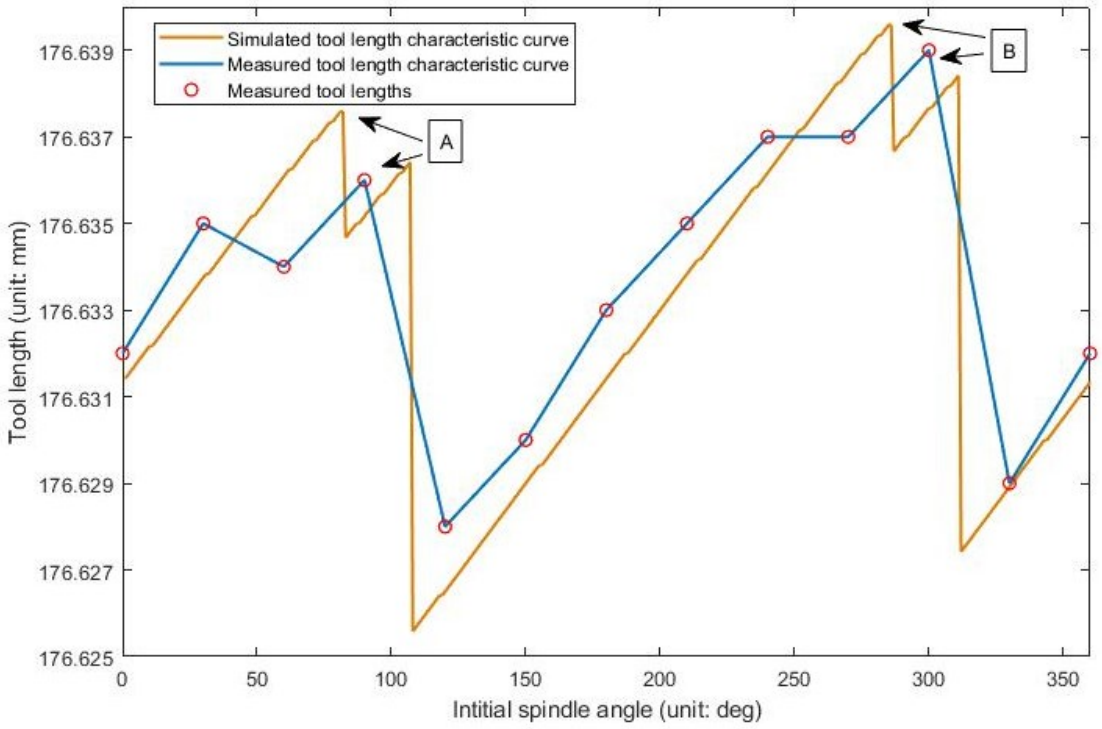

Figure 3.23. Experiment results show that the simulated tool length characteristic curve is very close to the measured tool length characteristic curve.

To further demonstrate the validity of the proposed method, another tool is measured. The measured lengths for its flutes were compared to those measured on an optical tool presetter. The tool used was a two insert mill and the lengths of its flutes were measured as 185.649mm and 185.643mm. The spindle speed and the feed rate of the measurement task were 1000 rpm and 30 mm/min. The NC program placed the tool about 10mm above the laser tool setter and positioned the spindle at the specified angles before measurement. The program looped until 12 measured tool lengths were obtained and the tool length characteristic curve was constructed. Two peaks were expected to occur on the tool length characteristic curve and the values of the

two peaks represent the length of each flute. In addition, the NC program runtime was also recorded.

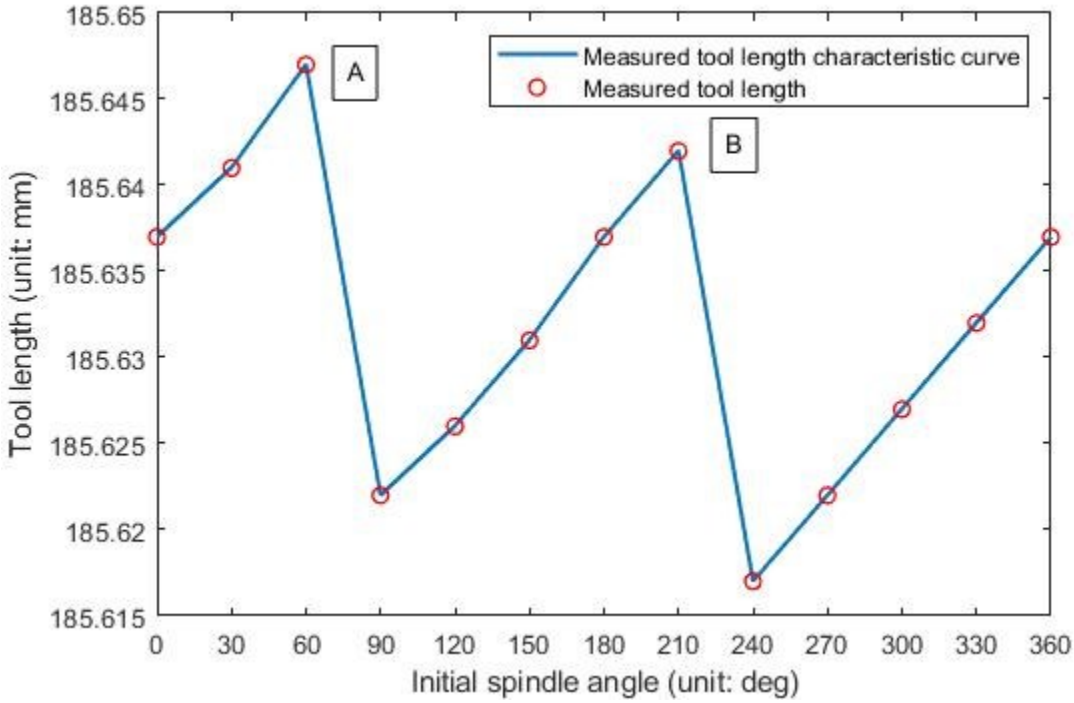

Figure 3.24. Experiment results show that the simulated tool length characteristic curve is very close to the measured tool length characteristic curve.

The results of the experiment are shown in

Figure 3.24. The value of peak A is 185.647 mm and it corresponds to the tool length of one flute, which only deviated 0.002mm from the tool length measured on a tool presetter. The value for peak B is 185.642 mm and it corresponds to the tool length of the other flute, which only deviated 0.001mm from the tool length measured on a tool presetter. Additionally, the

program run time was about 1 minute 20 seconds, benefiting from the large measurement feed rate. The runtime for the currently available tool setting NC program is about 2 minutes. This showed the proposed method is accurate and efficient.

3.7 Summary

This paper developed an accurate and efficient approach for measuring the round insert end-mill length and bottom cutting edges wear with on-machine laser tool setters. First, the fundamentals of on-machine tool length measurement and the geometric principles were described. To address the random errors that occurred in the current methods of tool length measurement with laser tool setters, a measurement simulation is built by modeling the tool and the tool measurement process. The simulation provides means to calculate tool length measurement errors of the tool length measurement process. Based on the calculation results, this research discovered a tool length characteristic curve for round insert cutters. Based on the tool length characteristic curve, a new method for accurate and efficient tool length on-machine measurement was proposed. Experiments showed the validity of the simulated tool length characteristic curve and the accuracy and efficiency of the proposed tool length measurement method. This work lays a foundation for the further development of accurate and efficient on-machine tool length measurement methods for other common tools.

Chapter 4

Simultaneous calibration of probe parameters and location errors of rotary axes on multi-axis CNC machines by using a sphere

4.1 Introduction

The accuracy of OMM systems is limited by the machine tool motion inaccuracy in following planned paths. When motions of rotary axes are involved, such limits expand, particularly in two aspects. On the one hand, the calibration task is restraint, which prompts an ill-determined probe position in the machine. On the other hand, the readouts in measurement tasks incorporate errors due to the unexpected positioning of machine axes. The straightforward endeavor for improvement via hardware update is often expensive and its achievable accuracy is finite to address this problem. Consequently, cost-effective methods to identify and compensate the machine motion inaccuracy have long been a research topic.

Geometric errors of the machine axes are the major contributor to the machine tool inaccuracy [22, 28, 30, 83-88]. With geometric errors, the actual machine positions do not accord to the command positions [10, 89]. Consequently, the cutter does not cut at the planned location, resulting in machining errors; different positions on the workpiece will be measured by the

measurement device, resulting in measurement error. According to ISO 230-1[10] and ISO 230-7[89], the geometric errors of each axis are categorized in component errors and location errors. Component errors refer to errors due to the imperfection of machine components, and location errors refer to errors due to assembly inaccuracy. For clarity, note that in many literatures, component errors are known as position-dependent geometric errors (PDEGs) and positioning error, while location errors are known as position-independent errors (PIGEs) [28, 30, 90]. During the service of the machine tool, its components continue to wear out, leading to the geometric errors (both the component errors and the location errors) change overtime. Thus, an effective way to calibrate the machine and compensate the geometric errors periodically is important to guarantee the machine and measurement accuracy.

In the present machine calibration schemes using OMM systems, particularly touch-triggered probes, the probe is assumed to locate at the spindle axis, and its position in the machine coordinate system is known before machine calibration. However, the following two factors must be addressed to complete the machine calibration schemes using OMM systems. First, the machine axes geometric errors deviate the probe from its ideal position. The deviation is enlarged when the probe is installed on rotary axes, for example, spindle-tilting machines and spindle/table tilting machines [91], and rotation motions are involved in measurement tasks. Moreover, when probes are installed to specialized machines as add-ons, the probe often locates away from the spindle axis because its position is selected based on many engineering aspects. Accurate measurement of the probe position in consideration of the machine geometric errors is crucial for the operation of the OMM system. In other words, both the machine and the probe

require calibration. Unfortunately, the current five-axis machine calibration model cannot manage these tasks.

To address the current limitations, this study proposed a method to automatically identify the link parameters of the machine (including the probe's position) and the rotary axes location errors defined in ISO 230-7 by probing a sphere artifact. The machine in this study is a six-axis belt grinding CNC machine (see Figure 4.1). The dimension of the artifact is certified on a coordinate measurement machine. The proposed method maintains operational simplicity while overcame the difficulties of current practices, including the need to determine the position of the probe, the artifacts, and the rotary axes locations before measurement. The evaluated parameters and location errors can be compensated by updating the kinematic chain used in the post-processor. This study is organized as follows. The actual kinematic chain considering the location errors of the rotary axes for a six-axis belt grinding machine with a touch-triggered probe installed is derived in Section 4.2. The probing strategies to identify the probe parameters and the location errors of the rotary axes are presented in Section 4.3, in which necessary mathematical equations for result generations are given. Section 4.4 uses experiment results to demonstrate the validity of the proposed method. Section 4.5 discusses the influence of the uncertainties of linear axes motions to the proposed method, followed by a conclusion drawn in Section 6.

4.2 The Machine Structure, Parameters to Identify, and the Actual Configuration of a Six-axis CNC Belt Grinding Machine

4.2.1 The structure of a six-axis CNC belt grinding machine

Figure 4.1 shows the structure of the machine tool adopted in this study which has three translational axes (e.g., the X-, Y-, and Z- axes) and three rotary axes (e.g., the A-, B- and C- axes). The X-axis is a slide on a rail that is supported by the rail of the Y-axis. The column supporting the Z-axis slide is installed on the Y-axis slide. Two swing heads are in the machine, representing the B-axis and the C –axis. The B-axis is assembled at the height of the Z-axis column, and the C-axis is attached to the B –axis assembly. The B- and C- axes do not intersect. Meanwhile, the axis of the flange of a rotary table, assembled on the X-axis, is the A-axis. The translation motion of the X-, Y- and Z- axes are actuated by ball screws pairs. The rotational movement of the A-axis is directly generated by a high precision servo motor, to which the spindle is the A-axis flange is directly connected. The rotational motion of the B- and C- axes are achieved by gear pairs (see Figure 4.1). A touch-triggered probe assembled to a pneumatic actuator attached to the front of the C-axis swing head.

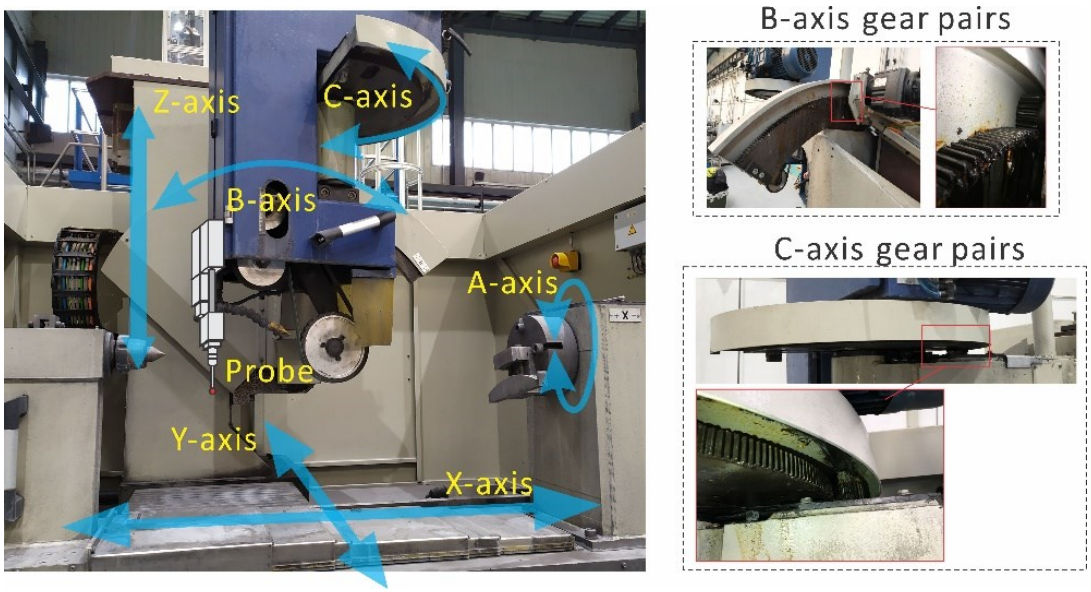

Figure 4.1 The machine structure of the belt grinding machine and the gear pairs of the B-axis and the C-axis

The machine zero position is set up at a unique position. The six-axis CNC belt grinding machine is a special purposed machine without a spindle reference point. The establishment of the machine coordinate system takes the followed procedure. When all the machine axes return to zero, the center of the end face of the grinding wheel supporting rod $\mathbf{O}_r$ and the top face of the A-axis flange $\mathbf{O}_a$ both locate at a point $\mathbf{O}_m$ on the A-axis (see Figure 4.2). $\mathbf{O}_m$ is chosen as the machine coordinate system origin. The machine coordinate system ($\mathbf{X}_m$ - $\mathbf{Y}_m$ - $\mathbf{Z}_m$ - $\mathbf{O}_m$) is established at $\mathbf{O}_m$. The $\mathbf{X}_m$ -, $\mathbf{Y}_m$ - and $\mathbf{Z}_m$ - axes are along the X, Y, and Z rail, respectively. This is a fixed frame, and it can be viewed as a reference coordinate system. Following ISO 841:2001 [92], the machine moving to the $\mathbf{X}_m$ - positive direction will affect the rail of the $\mathbf{X}_m$ -axis moving to the opposite direction. When the machine moves linearly, $\mathbf{O}_r$ remains in the $\mathbf{Y}_m\mathbf{Z}_m$ plane and

$\mathbf{O}_a$ remains in the $\mathbf{X}_m\mathbf{Y}_m$ plane. The distance between $\mathbf{O}_r$ and $\mathbf{O}_m$ along with the positive $\mathbf{Y}_m$- and $\mathbf{Z}_m$- directions are the machine command values Y_{cmd} and Z_{cmd}. The distance between $\mathbf{O}_a$ and $\mathbf{O}_m$ along the positive $\mathbf{X}_m$- direction is the negative machine command value X_{cmd}. Note that the command values are input to the CNC control for linear motions commands such as G00 and G01.

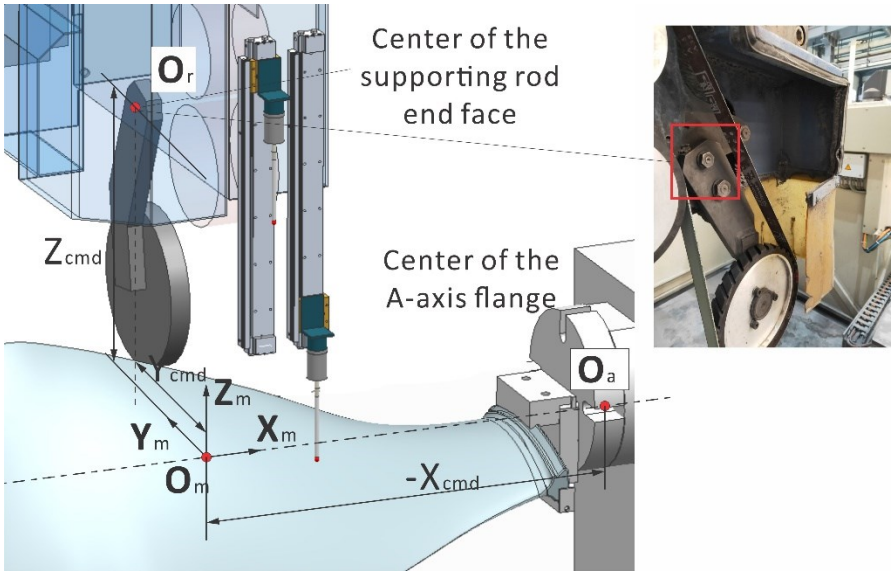

Figure 4.2 The machine coordinate system

4.2.2 Parameters to identify

In this paper, we refer to the parameters that define the actual probe center position as the probe parameters in $\mathbf{X}_m$ - $\mathbf{Y}_m$ - $\mathbf{Z}_m$ - $\mathbf{O}_m$ and the rotary axes' location errors to describe how much in terms of orientation and position that the axes deviate from their ideal locations in $\mathbf{X}_m$ - $\mathbf{Y}_m$ - $\mathbf{Z}_m$ - $\mathbf{O}_m$. Without proper measurement, the accurate probe position in $\mathbf{X}_m$ - $\mathbf{Y}_m$ - $\mathbf{Z}_m$ - $\mathbf{O}_m$ is unknown, and the rotary axes' location errors can only be assumed as negligible. Consequently,

the design values for the probe center position and the ideal location for the B- and C- axes, obtained from the machine manufacturer's design drawings, are used in the post-processing stage of CNC programming. The command values for the cutter or the probe will be generated referencing rotary axes other than the actual axes, which will lead to significant positioning errors. The followings describe in detail the definitions for these two groups of parameters with the belt-grinding CNC machine as the example.

The machine B- and C- axes' positions in $\mathbf{X}_m - \mathbf{Y}_m - \mathbf{Z}_m - \mathbf{O}_m$ must always be known to position the grinding wheel or the probe accurately. This is achieved by defining the distances of the B- and C- axis to $\mathbf{O}_r$ at the machine command values B = 0 and C=0. The spatial relationship between the machine axes is shown in Figure 4.3. The distance between the machine B-axis and $\mathbf{O}_r$ along the $\mathbf{X}_m$ -axis and $\mathbf{Z}_m$ -axis is d_{rbx} and d_{rbz}, respectively. The distance between the machine C-axis and $\mathbf{O}_r$ along the $\mathbf{X}_m$ - and $\mathbf{Y}_m$ - axis is d_{rcx} and d_{rcy}, respectively. Aside from the B- and C- axis, the probe's position installed on the machine must also be traced as the machine moves. For this purpose, the distances between the probe tip $\mathbf{O}_p$ and $\mathbf{O}_r$ in the $\mathbf{X}_m$ -, $\mathbf{Y}_m$ - and $\mathbf{Z}_m$ - positive directions are defined as d_{rpx}, d_{rpy}, and d_{rpz} respectively.

As shown in Figure 4.3, these parameters are distances in space and are very difficult to measure directly. One of our goals in this research is to propose an approach to calibrating these parameters indirectly.

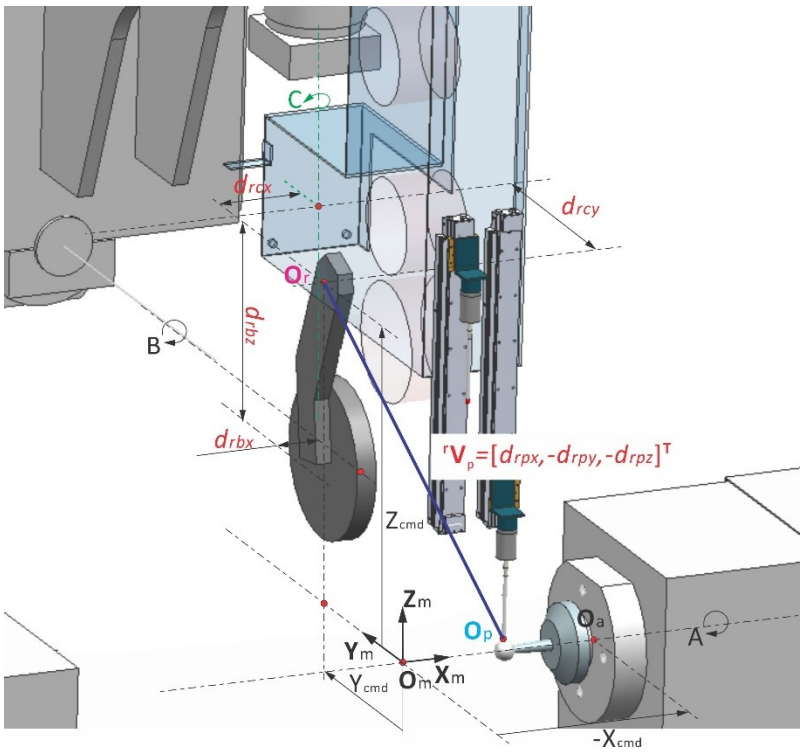

Figure 4.3 Spatial relationship between the machine axes

According to ISO 230-1, location errors of the machine linear axes refer to the orientations of the average line of the actual linear axis in the machine coordinate system. Similarly, location errors of the machine rotary axes are defined as the orientations and positions of the actual rotary axis average line in the machine coordinate system. To fully define a rotary axis, four location errors are needed. This research makes attempts to ensure OMM systems are set up accurately on a six-axis CNC machine tool. We investigate only the B-axis and the C-axis location errors based on the following reasons. First, the probe is installed on the C – axis, which is related to the B-axis, meaning that the location errors of the C- and B- axes will influence the probe position. Second, the B- and C- axes are both driven by exposed gear pairs, and the heavy structures of the C- and B- axes are stacked together on the rails, rendering them more prone to

errors. Additionally, we assume that the location errors of the linear axes are previously compensated, and their uncertainties are insignificant. However, the influence from the linear axes will be analyzed in Section 4.5.

According to ISO 230 – 1, the location errors for the B – axis and C- axis are shown in Table 4.1. Therefore, in summary, the probe parameters (d_{rpx}, d_{rpy} and d_{rpz}), the location errors for the B-axis (E_{XOB}, E_{ZOB}, E_{AOB} , and E_{COB}) and the location errors for the C-axis (E_{XOC}, E_{YOC}, E_{AOC} and E_{BOC}) are to identify.

Table 4.1 Location errors associated with the rotary axes

Symbols	Description
E_{XOB}	Linear offset of B-axis in the machine X direction
E_{ZOB}	Linear offset of B-axis in the machine Z direction
E_{AOB}	Squareness error of B-axis to the machine X direction
E_{COB}	Squareness error of B-axis to the machine Z direction
E_{XOC}	Linear offset of C-axis in the machine X direction
E_{YOC}	Linear offset of C-axis in the machine Y direction
E_{AOC}	Squareness error of C-axis to the machine X direction
E_{BOC}	Squareness error of C-axis to the machine Y direction

4.2.3 Actual configuration of the six-axis CNC belt grinding machine

The actual configuration of the six-axis CNC belt grinding machine is described using kinematic chains. This research establishes the kinematic chain from the probe tip center to the workpiece using homogeneous transformation matrices. Both the probe parameters and the rotary location errors participate in the kinematic chain.

We define the frame representing each axis in Figure 4.4 to describe the actual machine configuration and facilitate the kinematic chain's derivation. The frame for the X-axis ($\mathbf{X}_x$ - $\mathbf{Y}_x$ - $\mathbf{Z}_x$ - $\mathbf{O}_x$) is attached to the center of the flange of the A-axis rotary table. All its axes are parallel to $\mathbf{X}_m$ - $\mathbf{Y}_m$ - $\mathbf{Z}_m$ - $\mathbf{O}_m$. The translation motion of the X-axis to the positive direction of $\mathbf{X}_m$ will create a distance $-X_{cmd}$ between the flange of the A-axis rotary table and $\mathbf{O}_m$. The frame for the A-axis ($\mathbf{X}_a$ - $\mathbf{Y}_a$ - $\mathbf{Z}_a$ - $\mathbf{O}_a$) is defined to coincide with $\mathbf{X}_x$ - $\mathbf{Y}_x$ - $\mathbf{Z}_x$ - $\mathbf{O}_x$. The A-axis rotates about the $\mathbf{X}_a$ axis, and this rotation will form an angle $-A_{cmd}$ between $\mathbf{Y}_a$ and $\mathbf{Y}_x$. The workpiece is required to be installed on the A-axis table, and the workpiece coordinate system ($\mathbf{X}_w$ - $\mathbf{Y}_w$ - $\mathbf{Z}_w$ - $\mathbf{O}_w$) is coincided with $\mathbf{X}_a$ - $\mathbf{Y}_a$ - $\mathbf{Z}_a$ - $\mathbf{O}_a$. When the machine is at home position, the frame for the Y-axis ($\mathbf{X}_y$ - $\mathbf{Y}_y$ - $\mathbf{Z}_y$ - $\mathbf{O}_y$) and the frame for the Z-axis ($\mathbf{X}_z$ - $\mathbf{Y}_z$ - $\mathbf{Z}_z$ - $\mathbf{O}_z$) are both defined to coincide with $\mathbf{O}_m$. Their axes are parallel to $\mathbf{X}_m$ - $\mathbf{Y}_m$ - $\mathbf{Z}_m$ - $\mathbf{O}_m$. The translation motion of the Y-axis to the positive direction of $\mathbf{Y}_m$ will create a distance Y_{cmd} between $\mathbf{O}_y$ and $\mathbf{O}_m$. The translation motion of the Z-axis to the positive direction of $\mathbf{Z}_y$ will create a distance Z_{cmd} between $\mathbf{O}_z$ and $\mathbf{O}_y$. When $B_{cmd} = 0$ and $C_{cmd} = 0$, the center of the end face of the grinding wheel supporting rod, $\mathbf{O}_r$, will coincide with $\mathbf{O}_z$. $\mathbf{O}_r$ is used to define the frames for the B-axis, the C-axis, and the probe. The frame for the actual B axis ($\mathbf{X}'_b$ - $\mathbf{Y}'_b$ - $\mathbf{Z}'_b$ - $\mathbf{O}'_b$) is defined with the $\mathbf{Y}'_b$ axis coincided with the actual machine B axis. $\mathbf{O}'_b$ lies on a plane defined by $\mathbf{O}_r$ and the $\mathbf{Y}_m$ axis. The distance between $\mathbf{O}'_b$ and $\mathbf{O}_r$ along the $\mathbf{Z}_m$ direction is D_{rbz} and the distance along the $\mathbf{X}_m$ direction is D_{rbx} (D signifies that this is the distance referring to the actual axis). The frame

for the actual C axis ($\mathbf{X}'_c$ - $\mathbf{Y}'_c$ - $\mathbf{Z}'_c$ - $\mathbf{O}'_c$) is defined with $\mathbf{Z}'_c$ is along the actual machine C- axis. $\mathbf{O}'_c$ lies on a plane defined by $\mathbf{O}_r$ and $\mathbf{Z}_m$. The distance between $\mathbf{O}_r$ and $\mathbf{O}'_c$ along the $\mathbf{X}_m$ direction is D_{rcx} and the distance along the $\mathbf{Y}_m$ direction is D_{rcy}. For convenience, a frame ($\mathbf{X}_r$ - $\mathbf{Y}_r$ - $\mathbf{Z}_r$ - $\mathbf{O}_r$) is defined at $\mathbf{O}_r$ with all its axes parallel to $\mathbf{X}_m$ - $\mathbf{Y}_m$ - $\mathbf{Z}_m$ - $\mathbf{O}_m$. The frame for the probe ($\mathbf{X}_p$ - $\mathbf{Y}_p$ - $\mathbf{Z}_p$ - $\mathbf{O}_p$) is attached to the probe center and is parallel to $\mathbf{X}_m$ - $\mathbf{Y}_m$ - $\mathbf{Z}_m$ - $\mathbf{O}_m$. The distances between the probe tip and $\mathbf{O}_r$ in the $\mathbf{X}_m$, $\mathbf{Y}_m$ and $\mathbf{Z}_m$ directions are defined as d_{rpx}, d_{rpy} and d_{rpz} respectively.

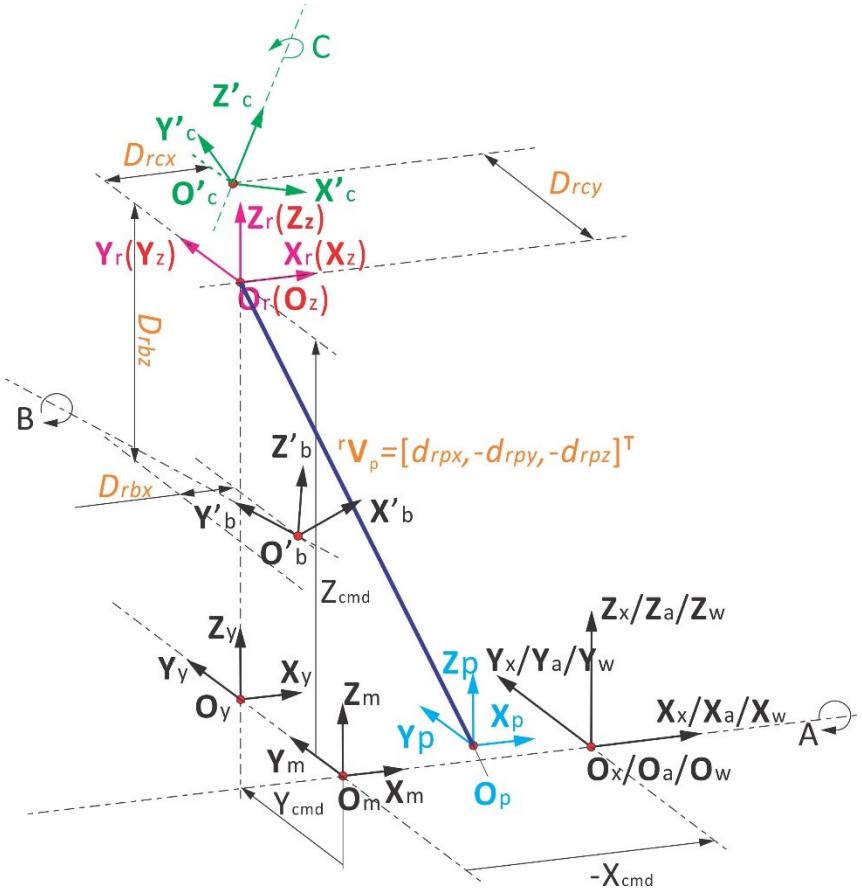

Figure 4.4 The actual configuration of the CNC machine

The kinematic chain branch from the workpiece to the machine frame is derived as follows. Thus, the spatial relationship that transforms from $\mathbf{X}_w$ - $\mathbf{Y}_w$ - $\mathbf{Z}_w$ - $\mathbf{O}_w$ to $\mathbf{X}_m$ - $\mathbf{Y}_m$ - $\mathbf{Z}_m$ - $\mathbf{O}_m$ can be derived as

$$ {}^{m}\mathbf{T}_{w} = \begin{bmatrix} 1 & 0 & 0 & -X_{cmd} \\ 0 & \cos(-A_{cmd}) & \sin(-A_{cmd}) & 0 \\ 0 & -\sin(-A_{cmd}) & \cos(-A_{cmd}) & 0 \\ 0 & 0 & 0 & 1 \end{bmatrix} \tag{4.1} $$

The kinematic chain branch from the probe tip to the machine frame is derived as follows. From $\mathbf{X}_p$ - $\mathbf{Y}_p$ - $\mathbf{Z}_p$ - $\mathbf{O}_p$ to $\mathbf{X}_r$ - $\mathbf{Y}_r$ - $\mathbf{Z}_r$ - $\mathbf{O}_r$, the sub kinematic chain is

$$ {}^{r}\mathbf{T}_{p} = \begin{bmatrix} 1 & 0 & 0 & d_{rpx} \\ 0 & 1 & 0 & -d_{rpy} \\ 0 & 0 & 1 & -d_{rpz} \\ 0 & 0 & 0 & 1 \end{bmatrix} \tag{4.2} $$

The offset location errors of the B-axis and C-axis are given as

$$ E_{XOB} = D_{rbx} - d_{rbx} \tag{4.3} $$

$$ E_{ZOB} = D_{rbz} - d_{rbz} \tag{4.4} $$

$$ E_{XOC} = D_{rcx} - d_{rcx} \tag{4.5} $$

$$ E_{YOC} = D_{rcy} - d_{rcy} \tag{4.6} $$

Assuming only minor location errors exist and the unit of the location errors is radian, from $\mathbf{X}_r$ - $\mathbf{Y}_r$ - $\mathbf{Z}_r$ - $\mathbf{O}_r$ to $\mathbf{X}_{c'}$ - $\mathbf{Y}_{c'}$ - $\mathbf{Z}_{c'}$ - $\mathbf{O}_{c'}$, the sub kinematic chain can be approximated as

$$
{}^{c'}\mathbf{T}_{\mathrm{r}}=\begin{bmatrix}\cos(C_{cmd}) & -\sin(C_{cmd}) & 0 & 0\\ \sin(C_{cmd}) & \cos(C_{cmd}) & 0 & 0\\ 0 & 0 & 1 & 0\\ 0 & 0 & 0 & 1\end{bmatrix}\begin{bmatrix}1 & 0 & -E_{B0C} & 0\\ 0 & 1 & E_{A0C} & 0\\ E_{B0C} & -E_{A0C} & 1 & 0\\ 0 & 0 & 0 & 1\end{bmatrix}\begin{bmatrix}1 & 0 & 0 & -D_{rcx}\\ 0 & 1 & 0 & -D_{rcy}\\ 0 & 0 & 1 & 0\\ 0 & 0 & 0 & 1\end{bmatrix} \tag{4.7}
$$

and the sub kinematic chain from $\mathbf{X}_{c'}\text{-}\mathbf{Y}_{c'}\text{-}\mathbf{Z}_{c'}\text{-}\mathbf{O}_{c'}$ to $\mathbf{X}_{b'}\text{-}\mathbf{Y}_{b'}\text{-}\mathbf{Z}_{b'}\text{-}\mathbf{O}_{b'}$ can be approximated as

$$
\begin{aligned}
{}^{b'}\mathbf{T}_{c'}=&\begin{bmatrix}\cos(B_{cmd}) & 0 & \sin(B_{cmd}) & 0\\ 0 & 1 & 0 & 0\\ -\sin(B_{cmd}) & 0 & \cos(B_{cmd}) & 0\\ 0 & 0 & 0 & 1\end{bmatrix}\begin{bmatrix}1 & E_{C0B} & 0 & 0\\ -E_{C0B} & 1 & E_{A0B} & 0\\ 0 & -E_{A0B} & 1 & 0\\ 0 & 0 & 0 & 1\end{bmatrix}\cdot\\
&\begin{bmatrix}1 & 0 & 0 & D_{rcx}-D_{rbx}\\ 0 & 1 & 0 & D_{rcy}\\ 0 & 0 & 1 & D_{rbz}\\ 0 & 0 & 0 & 1\end{bmatrix}\begin{bmatrix}1 & 0 & E_{B0C} & 0\\ 0 & 1 & -E_{A0C} & 0\\ -E_{B0C} & E_{A0C} & 1 & 0\\ 0 & 0 & 0 & 1\end{bmatrix}
\end{aligned} \tag{4.8}
$$

The sub kinematic chain from $\mathbf{X}_{b'}\text{-}\mathbf{Y}_{b'}\text{-}\mathbf{Z}_{b'}\text{-}\mathbf{O}_{b'}$ to $\mathbf{X}_{m}\text{-}\mathbf{Y}_{m}\text{-}\mathbf{Z}_{m}\text{-}\mathbf{O}_{m}$ is

$$
{}^{m}\mathbf{T}_{b'}=\begin{bmatrix}1 & 0 & 0 & D_{rbx}\\ 0 & 1 & 0 & Y_{cmd}\\ 0 & 0 & 1 & Z_{cmd}-D_{rbz}\\ 0 & 0 & 0 & 1\end{bmatrix}\begin{bmatrix}1 & -E_{C0B} & 0 & 0\\ E_{C0B} & 1 & -E_{A0B} & 0\\ 0 & E_{A0B} & 1 & 0\\ 0 & 0 & 0 & 1\end{bmatrix} \tag{4.9}
$$

and the kinematic chain branch from $\mathbf{X}_{p}\text{-}\mathbf{Y}_{p}\text{-}\mathbf{Z}_{p}\text{-}\mathbf{O}_{p}$ to $\mathbf{X}_{m}\text{-}\mathbf{Y}_{m}\text{-}\mathbf{Z}_{m}\text{-}\mathbf{O}_{m}$

$$
{}^{m}\mathbf{T}_{p}={}^{m}\mathbf{T}_{b'}\cdot{}^{b'}\mathbf{T}_{c'}\cdot{}^{c'}\mathbf{T}_{r}\cdot{}^{r}\mathbf{T}_{p} \tag{4.10}
$$

The kinematic chain of the six-axis CNC belt grinding machine can be formed by combing the sub kinematic chain from $\mathbf{X}_{p}\text{-}\mathbf{Y}_{p}\text{-}\mathbf{Z}_{p}\text{-}\mathbf{O}_{p}$ to $\mathbf{X}_{m}\text{-}\mathbf{Y}_{m}\text{-}\mathbf{Z}_{m}\text{-}\mathbf{O}_{m}$ and the sub kinematic chain from

$\mathbf{X}_w$ - $\mathbf{Y}_w$ - $\mathbf{Z}_w$ - $\mathbf{O}_w$ to $\mathbf{X}_m$ - $\mathbf{Y}_m$ - $\mathbf{Z}_m$ - $\mathbf{O}_m$. Therefore, the transformation matrix that describes the spatial relationship between $\mathbf{X}_p$ - $\mathbf{Y}_p$ - $\mathbf{Z}_p$ - $\mathbf{O}_p$ and $\mathbf{X}_w$ - $\mathbf{Y}_w$ - $\mathbf{Z}_w$ - $\mathbf{O}_w$ is given by

$$ {}^{w}\mathbf{T}_p = \left({}^{m}\mathbf{T}_w \right)^{-1} \cdot {}^{m}\mathbf{T}_p \tag{4.11} $$

Specifically, the probe center ${}^{w}\mathbf{O}_p$ in the workpiece coordinate system ($\mathbf{X}_w$ - $\mathbf{Y}_w$ - $\mathbf{Z}_w$ - $\mathbf{O}_w$) is given by

$$ {}^{w}\mathbf{O}_p = {}^{w}\mathbf{T}_p \cdot \begin{bmatrix} 0 \\ 0 \\ 0 \\ 1 \end{bmatrix} \tag{4.12} $$

Two sets of parameters are presented in the derivation of the kinematic chain. The parameters X_{cmd}, Y_{cmd}, Z_{cmd}, A_{cmd}, B_{cmd}, and C_{cmd} are the machine command values defined in the machine coordinate system. These are the parameters to be input as the G-code coordinate values to drive the machine. The other set of parameters are the parameters to calibrate and identify, namely, the probe parameters (d_{rpx}, d_{rpy} and d_{rpz}), the location errors for the B-axis (E_{XOB}, E_{ZOB}, E_{AOB}, and E_{COB}) and the location errors for the C-axis (E_{XOC}, E_{YOC}, E_{AOC} and E_{BOC}). These parameters describe the actual relative positions for the structure of each axis and the probe. It is crucial to calibrate these parameters to guarantee the conformity between the planned tool paths and the actual tool paths on the CNC machine. The methods to calibrate and identify these parameters are introduced in the following section.

4.3 Identification and Calibration of Machine Parameters

4.3.1 The working principle of the calibration method

This research proposes a machine and probe calibration method using on-machine measurement techniques. Two steps are involved in the method. First, the parameters of interest are identified. Second, the identified parameters should be updated to the kinematic chain used in post-processing to eliminate the machine's overall positional errors.

The working principles of the identification process are provided as the following. The process uses an on-machine touch-triggered probe to measured target surface points on the sphere artifacts. The coordinates of the targeted surface points on the artifact in the artifact coordinate system are measured separately on a coordinate measurement machine (CMM) before the identification process. When the artifact is installed on the CNC machine, measures are taken to ensure that the artifact coordinate system coincides with the workpiece coordinate system. A set of specialized paths are planned for the probe to ensure that the probe tip can always contact the top of the sphere, whose coordinates in the workpiece coordinate system are known. This way, at the probe trigger instant, both the machine linear axes command values (X, Y, and Z) are recorded, and the coordinate of the probe center in $\mathbf{X}_w$ - $\mathbf{Y}_w$ - $\mathbf{Z}_w$ - $\mathbf{O}_w$ is known. On the other hand, the kinematic model can obtain the relation between the theoretical command values, probe center, and the parameters to identify. The parameters can be identified by minimizing the difference between the theoretical command values and the actual recorded command values pairs.

Once the parameters are identified, the calibration process can be completed by revising the design machine link parameters used in the kinematic chains to be the parameters identified. Moreover, the kinematic chain taking the location errors into account must be used in the post-processing software with the identified location errors. Section 4.2 has described such a kinematic chain.

4.3.2 The measurement instruments and the testing artifact

A touch-triggered probe is used in our method. The probe (see Figure 4.5) is wired to the CNC machine control and is driven by the CNC machine. Once the probe tip sphere comes into contact with an object, the probe raises a signal, and the CNC machine will capture its current command values in the machine coordinate system. A typical touch-triggered probe has a repeatability of 1 μm. Before using the probe, the small antistrophic sensitivities issues of the probe are calibrated and compensated.

Figure 4.5 Touch-triggered probe

The artifact is a high-accuracy ceramic sphere mounted on a plate at a height. The plate is designed to fit the A-axis flange so that the sphere center locates on the A-axis. The bottom of the plate contacts the A-axis flange surface, which is the datum for all workpieces machined on the CNC machine. The distance between the sphere center and the bottom of the plate, d_s, is calibrated on a coordinate measurement machine and expressed in the artifact coordinate system, which locates at the center of the sphere and its X-axis perpendicular to the bottom of the plate. After the artifact is installed on the machine, a slight adjustment can be made to guarantee the sphere center being on the A-axis (See Figure 4.6). Consequently, the artifact coordinate system coincides with the workpiece coordinate system in this setup. The coordinates of the sphere surface points in the workpiece coordinate system are determined. Specifically, the coordinate of the top of the sphere in the workpiece coordinate system is

$$ {}^{w}\mathbf{P}_s = \begin{bmatrix} -d_s \\ 0 \\ R_s \\ 1 \end{bmatrix} \tag{4.13} $$

where R_s is the radius of the sphere.

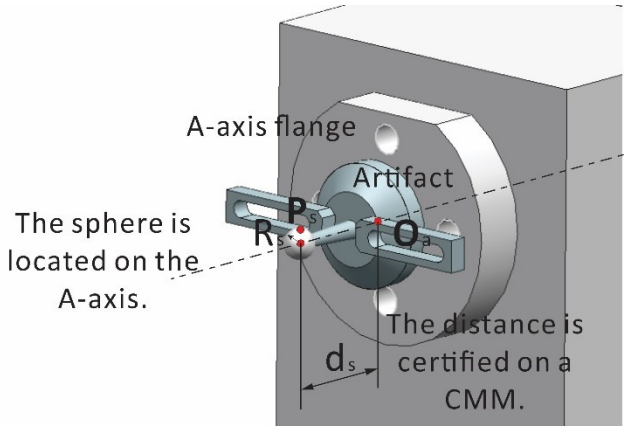

Figure 4.6 The artifact used and its setup on the machine

In the proposed method, the machine will drive the probe to contact the known coordinates of the spheres at different rotation angles commanded to the rotary axes and with different patterns. Considering the complexity and nonlinearity of the kinematic chain, categorically, two probing patterns described in the following sections are used to simplify the parameters identification process. The obtained data can be used to calculate the probe parameters and the machine rotary axes location errors using optimization techniques.

4.3.3 Probing pattern for the probe parameters and the location errors for the C-axis

We perform the probing task to identify parameters for the probe and the C-axis with the B-axis fixed. Fixing the B-axis can reduce the unknowns. The probing pattern is as follows. The B-axis is set at 0 degrees. The C-axis is set at different angles C_i . At each C-axis angle, the top of the sphere is probed, and the machine command values (X_{cmd}^{ci} , Y_{cmd}^{ci} and Z_{cmd}^{ci}) are stored at the trigger instant (see Figure 4.7).

The alignment of the probe tip and the top of the sphere is essential. To guarantee this, the machine command values to roughly align the probe tip to the sphere center were determined first. A cross-section *I* on the sphere parallel to the machine XY plane was selected, and the sphere was probed along the Xm+, Xm-, Ym+, and Ym- directions (see Figure 4.8(a)). By averaging the X components from the data of Xm+ and Xm- and the Y components from the Ym+ and Ym-, the machine command values that roughly align the probe tip to the center of the sphere can be

found. Then on the same cross-section, 6 points uniformly distributed on the sphere were probed, and the best fit circle was used to approximate the data corresponding to the 6 sampled points (see Figure 4.8(b)). The center of the best fit circle can accurately align the probe tip to the sphere's center. After alignment, the probe moves along the Zm- direction towards the sphere to sample the top of the sphere (see Figure 4.8(c)).

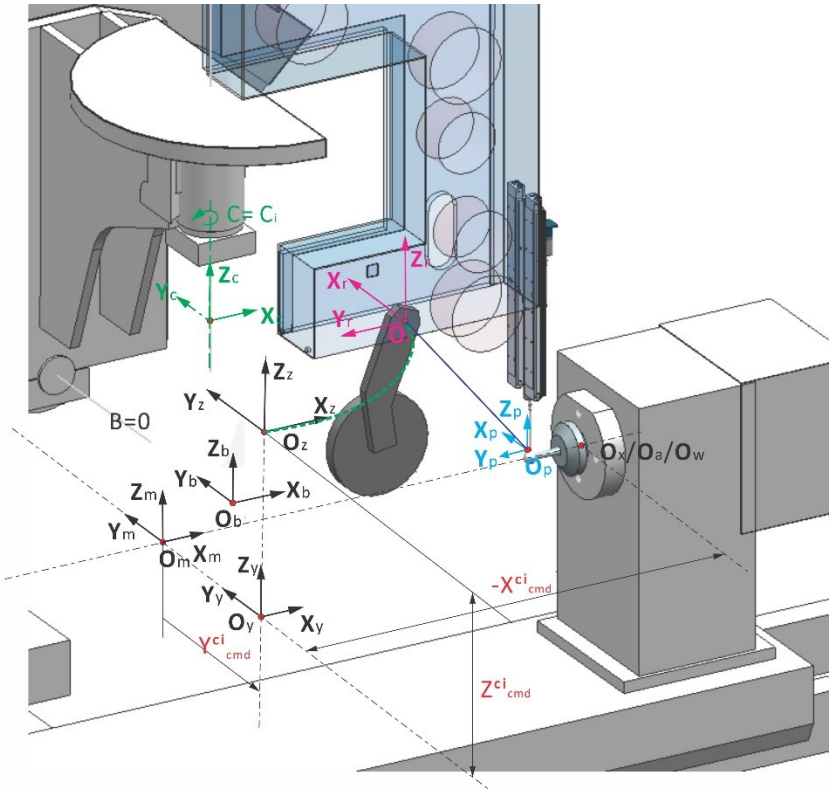

Figure 4.7 One sampling position in probing pattern I and its recorded data

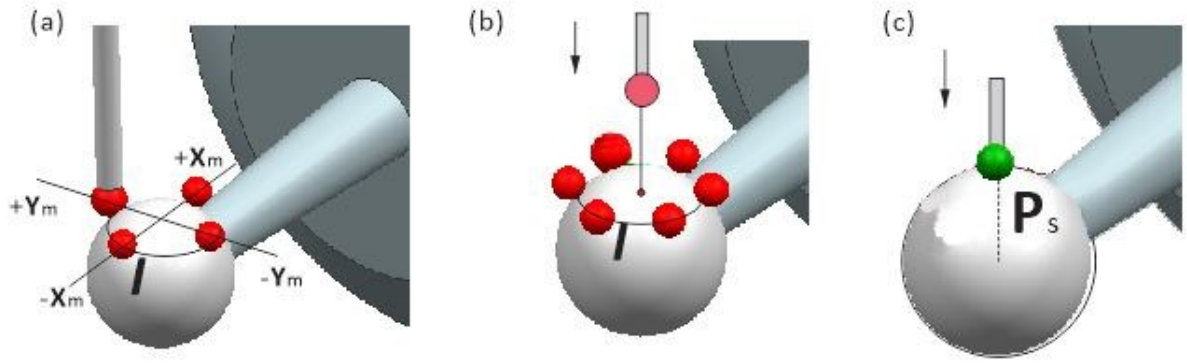

Figure 4.8 Aligning the probe tip to the top of the sphere

We first identify the location errors of the C-axis using the recorded data. Supposed *n* numbers of angles for the C- axis are tested. The recorded data for each C-axis angle C_i is the machine command values for the X-, Y- and Z- axis (X_{cmd}^{ci} , Y_{cmd}^{ci} and Z_{cmd}^{ci}), and they are defined in $\mathbf{X}_m - \mathbf{Y}_m - \mathbf{Z}_m - \mathbf{O}_m$. These command values can be used to represent the $\mathbf{O}_z$ in $\mathbf{X}_w - \mathbf{Y}_w - \mathbf{Z}_w - \mathbf{O}_w$ using

$$ {}^{w}\mathbf{O}^{ci}{}_{z} = \begin{bmatrix} 1 & 0 & 0 & X_{cmd}^{ci} \\ 0 & 1 & 0 & Y_{cmd}^{ci} \\ 0 & 0 & 1 & Z_{cmd}^{ci} \\ 0 & 0 & 0 & 0 \end{bmatrix} {}^{Z}\mathbf{O}^{ci}{}_{z} = \begin{bmatrix} X_{cmd}^{ci} \\ Y_{cmd}^{ci} \\ Z_{cmd}^{ci} \\ 1 \end{bmatrix} \tag{4.14} $$

Because the probe tip always references the top of the sphere whose position is fixed in the machine and only the C-axis is rotated, ${}^{w}\mathbf{O}^{ci}{}_{z}$ obtained from the recorded command values scatter on a plane parallel to the XY plane of $\mathbf{X}_w - \mathbf{Y}_w - \mathbf{Z}_w - \mathbf{O}_w$. When the squareness location errors of the C-axis exist, the data scatter on a plane perpendicular to the actual C-axis in

$\mathbf{X}_w$ - $\mathbf{Y}_w$ - $\mathbf{Z}_w$ - $\mathbf{O}_w$ (see Figure 4.9). Supposed the normal of the regression plane for these calculated ${}^{w}\mathbf{O}^{ci}{}_{z}$ values is $\mathbf{V}_c = \begin{bmatrix} v_{cx} & v_{cy} & v_{cz} \end{bmatrix}^T$ in $\mathbf{X}_w$ - $\mathbf{Y}_w$ - $\mathbf{Z}_w$ - $\mathbf{O}_w$. Since $\mathbf{X}_w$ - $\mathbf{Y}_w$ - $\mathbf{Z}_w$ - $\mathbf{O}_w$ is parallel to $\mathbf{X}_m$ - $\mathbf{Y}_m$ - $\mathbf{Z}_m$ - $\mathbf{O}_m$, when the actual C-axis is represented in $\mathbf{X}_m$ - $\mathbf{Y}_m$ - $\mathbf{Z}_m$ - $\mathbf{O}_m$, its normal vector equals to of $\mathbf{V}_c = \begin{bmatrix} v_{cx} & v_{cy} & v_{cz} \end{bmatrix}^T$. Then the squareness location errors of the C-axis are given as

$$E_{AOC} = \arctan\left(-\frac{v_{cy}}{v_{cz}}\right) \cdot \frac{180^\circ}{\pi} \tag{4.15}$$

and

$$E_{BOC} = \arctan\left(\frac{v_{cx}}{v_{cz}}\right) \cdot \frac{180^\circ}{\pi} \tag{4.16}$$

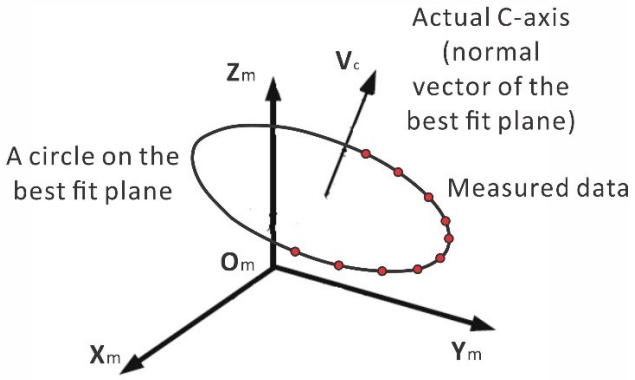

Figure 4.9 Estimation of the actual C-axis direction

The probe parameters (d_{rpx}, d_{rpy} and d_{rpz}) and the linear location errors of the C-axis (E_{XOC} and E_{YOC}) are related to the machine command values. The recorded machine command values

in the pattern are used to identify these parameters. In the probing process, the B-axis is fixed, and the sphere center is on the A-axis. We select $A=0$ and $B=0$. By setting $B=0$, the influence of parameters for the B-axis can be eliminated. Then, if $C=C_{cmd}^{ci}$ is commanded, Eq. (4.12) can be rewritten as

$$ {}^{w}\mathbf{O}_{p}=\begin{bmatrix} Q_1\cdot\cos\left(C_{cmd}^{ci}\right)+Q_2\cdot\sin\left(C_{cmd}^{ci}\right)+X+d_{rcx}-E_{BOC}\cdot d_{rpz} \\ -Q_2\cdot\cos\left(C_{cmd}^{ci}\right)+Q_1\cdot\sin\left(C_{cmd}^{ci}\right)+Y+d_{rcy}+E_{AOC}\cdot d_{rpz} \\ Q_3\cdot\cos\left(C_{cmd}^{ci}\right)+Q_4\cdot\sin\left(C_{cmd}^{ci}\right)+Z-d_{rpz}+E_{AOC}\cdot\left(d_{rpy}+D_{rcy}\right)-E_{BOC}\cdot\left(D_{rcx}-d_{rpx}\right) \\ 1 \end{bmatrix} \tag{4.17} $$

where,

$$ Q_1=d_{rpx}-D_{rcx}+E_{BOC}\cdot d_{rpz} \tag{4.18} $$

$$ Q_2=D_{rcy}+d_{rpy}+E_{AOC}\cdot d_{rpz} \tag{4.19} $$

$$ Q_3=E_{BOC}\cdot\left(D_{rcx}-d_{rpx}\right)-E_{AOC}\cdot\left(d_{rpy}+D_{rcy}\right) \tag{4.20} $$

$$ Q_4=E_{AOC}\cdot\left(d_{rpx}-D_{rcx}\right)-E_{BOC}\cdot\left(D_{rcy}+d_{rpy}\right) \tag{4.21} $$

When the probe tip touches the top of the sphere at $C=C_{cmd}^{ci}$, the coordinates of the probe tip center in the work coordinate system is

$$ {}^{w}\mathbf{O}_{p}=\begin{bmatrix} -d_s \\ 0 \\ R_c+R_p \\ 1 \end{bmatrix} \tag{4.22} $$

Combine Eq. (4.17) and Eq. (4.22) and solve for the command values renders,

$$X_{cmd}^{ci} = -d_s - Q_1 \cdot \cos\left(C_{cmd}^{ci}\right) - Q_2 \cdot \sin\left(C_{cmd}^{ci}\right) - D_{rcx} + E_{BOC} \cdot d_{rpz} \tag{4.23}$$

$$Y_{cmd}^{ci} = Q_2 \cdot \cos\left(C_{cmd}^{ci}\right) - Q_1 \cdot \sin\left(C_{cmd}^{ci}\right) - D_{rcy} - E_{AOC} \cdot d_{rpz} \tag{4.24}$$

$$Z_{cmd}^{ci} = R_c + R_p - Q_3 \cdot \cos\left(C_{cmd}^{ci}\right) - Q_4 \cdot \sin\left(C_{cmd}^{ci}\right) + d_{rpz} - E_{AOC} \cdot \left(d_{rpy} + D_{rcy}\right) + E_{BOC} \cdot \left(D_{rcx} - d_{rpx}\right)$$

(4.25)

Supposed at C_i angle, the recorded command values for the machine X-, Y- and Z- axes are $X_{cmd}^{ci'}$, $Y_{cmd}^{ci'}$ and $Z_{cmd}^{ci'}$ while the command values can be calculated as X_{cmd}^{ci} , Y_{cmd}^{ci} and Z_{cmd}^{ci} from Eq.(4.23)to Eq.(4.25). Then their differences are

$$\begin{aligned} \Delta X_{cmd}^{ci} &= X_{cmd}^{ci'} - X_{cmd}^{ci} \\ \Delta Y_{cmd}^{ci} &= Y_{cmd}^{ci'} - Y_{cmd}^{ci} \\ \Delta Z_{cmd}^{ci} &= Z_{cmd}^{ci'} - Z_{cmd}^{ci} \end{aligned} \tag{4.26}$$

After the location errors of the C-axis are identified, they can be used as known parameters in the model. If the number of sample points is nm, and the selected C axis angles are uniformly distributed in the travel range of the machine, then by substituting Eq.(4.5) and Eq.(4.6) to Eq.(4.26), the problem of calibrating the link parameters can be converted to the following minimization problem.

$$\min_{LP_{pc}} \sum_{i=1}^{nm} \left| \Delta X_{cmd}^{ci\ 2} + \Delta Y_{cmd}^{ci\ 2} + \Delta Z_{cmd}^{ci\ 2} \right| \tag{4.27}$$

where LP_{pc} is the set of link parameters for the probe and the C-axis and $LP_{pc} = E_{XOC}, E_{YOC}, d_{rpx}, d_{rpy}, d_{rpz}$. In the research, a genetic algorithm is used to solve this problem.

4.3.4 Probing pattern for identifying the location errors for the B-axis

A second probing pattern is needed to identify the location errors for the B-axis. In this pattern, the C-axis stays stationary, and the B-axis is positioned to given angles. Then the probe is driven to contact the top of the sphere, and the machine records the current command values. Considering the machine travel limits, the C-axis is set at 90 degrees. The B-axis varies at different angles B_i. At each B-axis angle B_i, the top of the sphere is probed, and the machine command values ($-X_{cmd}^{bi}$, Y_{cmd}^{bi} and Z_{cmd}^{bi}) are stored at the trigger instant (see Figure 4.10).

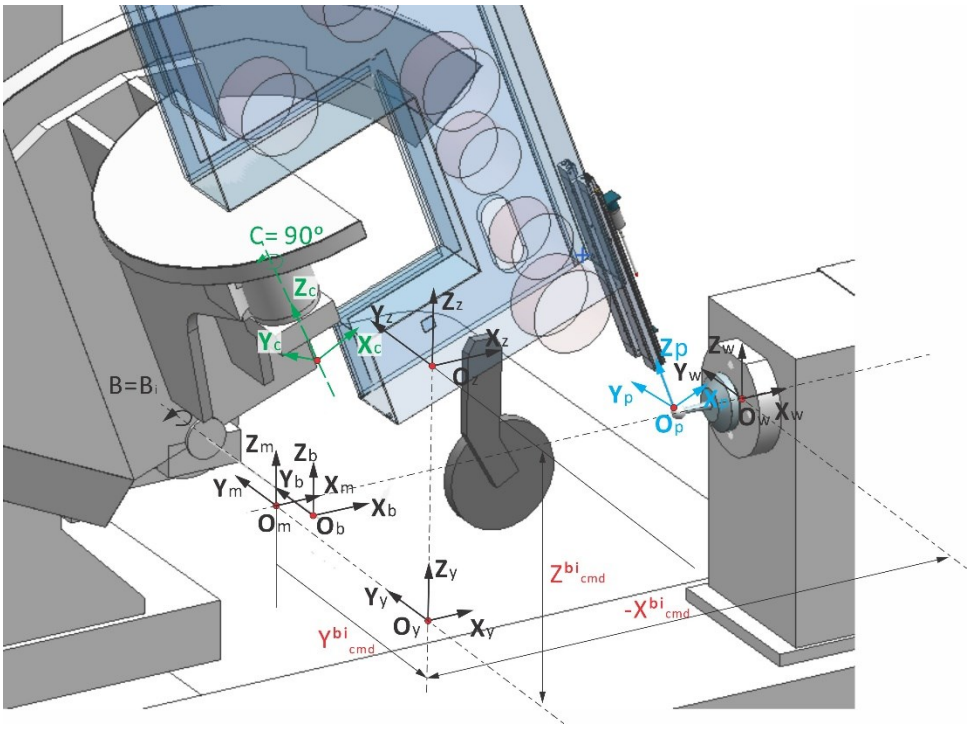

Figure 4.10 One sampling position in probing pattern II and its recorded data

Similar to probing pattern I, the squareness location errors for the B-axis are first identified. The data obtained in probing pattern II scatter on a plane perpendicular to the actual B-axis (see

Figure 4.11). The normal of the regression plane for these data is $\mathbf{V}_b = \begin{bmatrix} v_{bx} & v_{by} & v_{bz} \end{bmatrix}^T$, the squareness location errors of the B-axis are given as

$$E_{AOB} = \arctan\left(\frac{v_{bz}}{v_{by}}\right) \cdot \frac{180^\circ}{\pi} \tag{4.28}$$

and

$$E_{COB} = \arctan\left(-\frac{v_{cx}}{v_{cy}}\right) \cdot \frac{180^\circ}{\pi} \tag{4.29}$$

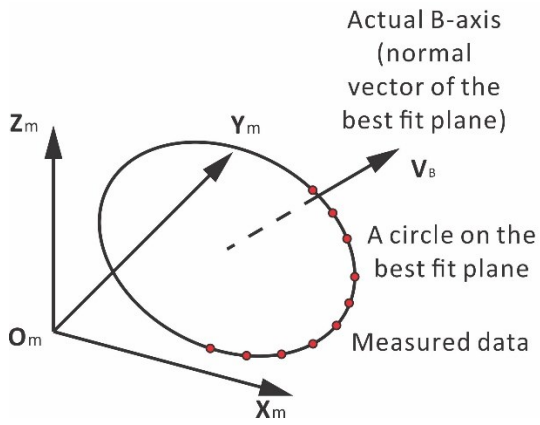

Figure 4.11 Estimation of the actual B-axis direction

In this probing process, the C-axis is fixed, and the sphere center is on the A-axis. We select $A = 0$ and $C = 90^\circ$. When the probe tip touches the top of the sphere at the specified angle for the B-axis, the recorded command values X, Y, and Z are,

$$X_{cmd}^{bi} = Q_6 \cdot \cos\left(B_{cmd}^{bi}\right) + Q_7 \cdot \sin\left(B_{cmd}^{bi}\right) + E_{COB} \cdot Q_5 - d_s - D_{rbx} \tag{4.30}$$

$$Y_{cmd}^{bi} = Q_8 \cdot \cos\left(B_{cmd}^{bi}\right) + Q_9 \cdot \sin\left(B_{cmd}^{bi}\right) + Q_{10} \tag{4.31}$$

$$Z_{cmd}^{bi} = Q_7 \cdot \cos\left(B_{cmd}^{bi}\right) - Q_6 \cdot \sin\left(B_{cmd}^{bi}\right) + R_c + R_p + D_{rbz} - E_{AOB} \cdot Q_5 \tag{4.32}$$

where

$$Q_5 = D_{rcy} - D_{rcx} + d_{rpx} \tag{4.33}$$

$$Q_6 = D_{rbx} - D_{rcx} - D_{rcy} - d_{rpy} + \left(E_{BOC} - E_{AOC}\right) \cdot d_{rpz} - E_{COB} \cdot Q_5 \tag{4.34}$$

$$Q_7 = d_{rpz} - D_{rbz} + E_{AOB} \cdot Q_5 - E_{AOC} \cdot \left(Q_5 + d_{rpy}\right) + E_{BOC} \cdot \left(D_{rcx} + D_{rcy} - d_{rpx} + d_{rpy}\right) \tag{4.35}$$

$$Q_8 = E_{AOB} \cdot \left(D_{rbz} - d_{rpz}\right) + E_{COB} \cdot \left(D_{rbx} - D_{rcx} - D_{rcy} - d_{rpy}\right) \tag{4.36}$$

$$Q_9 = E_{COB} \cdot \left(d_{rpz} - D_{rbz}\right) + E_{AOB} \cdot \left(D_{rbx} - D_{rcx} - D_{rcy} - d_{rpy}\right) \tag{4.37}$$

$$Q_{10} = \left(-D_{rbz}\right) \cdot E_{AOB} - d_{rpz} \cdot \left(E_{AOC} + E_{BOC}\right) + \left(D_{rcx} - D_{rbx} + D_{rcy} + d_{rpy}\right) \cdot E_{COB} - Q_5 \tag{4.38}$$

Supposed at B_i angle, $X_{cmd}^{bi'}$, $Y_{cmd}^{bi'}$ and $Z_{cmd}^{bi'}$ while the ideal command values are X_{cmd}^{bi} , Y_{cmd}^{bi} and Z_{cmd}^{bi} . Then their differences are

$$\begin{aligned} \Delta X_{cmd}^{bi} &= X_{cmd}^{bi'} - X_{cmd}^{bi} \\ \Delta Y_{cmd}^{bi} &= Y_{cmd}^{bi'} - Y_{cmd}^{bi} \\ \Delta Z_{cmd}^{bi} &= Z_{cmd}^{bi'} - Z_{cmd}^{bi} \end{aligned} \tag{4.39}$$

If the number of sample points is mm , and the selected B axis angles are uniformly distributed in the travel range of the machine, by substituting Eq.(4.3) and Eq.(4.4) to Eq.(4.39), then the problem of calibrating the link parameters can be converted to the following minimization problem

$$\min_{LP_b} \sum_{i=1}^{mm} \left| \Delta X_{cmd}^{bi\ 2} + \Delta Y_{cmd}^{bi\ 2} + \Delta Z_{cmd}^{bi\ 2} \right| \tag{4.40}$$

where LP_b is the set of link parameters for the probe and the C-axis and $LP_b = E_{XOB}, E_{ZOB}$. In the research, a genetic algorithm is used to solve this problem.

4.4 Experimental Results

4.4.1 Experimental setup

The proposed method was verified on a 6-axis turbine blade belt grinding machine manufactured by IMM Maschinenbau GmbH, shown in Figure 4.1. The machine travel limits are listed in Table 4.2. A touch-triggered probe, LP2, manufactured by Renishaw assembled with an SMC magnetically coupled air slide table, was installed on the machine. LP2 is a high precision probe with compacted size, and the influence of its antistrophic sensitivity is negligible. The probe tip was a ruby sphere with a diameter of 6mm. The specifications of the probe are summarized in Table 4.3.

The measured artifact was a ceramic sphere with a diameter of 25.000 mm and a roundness of 0.2 μm . Before installing the artifact, we verified that the front face of the A-axis flange has a flatness of about 5 microns. The perpendicularity of the front face to the A-axis is about 4 microns. To ensure the base of the artifact mate well with the front face of the A-axis flange, which is a datum plane for the workpiece coordinate system. The bottom face of the artifact base was machined to reach a flatness of 2 microns. The distance from the ceramic sphere to the end face of the base, measured on a CMM, was 184.183mm. It should also be mentioned that this distance

is often measured on the CNC machine using dial indicators in current literature. We believe measuring this distance on a CMM is more accurate based on two reasons. First, measuring directly on CNC machines with dial indicators is subjected to machine linear axes errors. Second, the extreme point of the sphere is hard to determine, which leads to the erroneous length measurement. With this artifact, alignment of the artifact coordinate system to the workpiece coordinate system requires only positioning the sphere center on the A-axis. A dial indicator can achieve such alignment. After the artifact was installed on the machine A-axis, both the concentricity of the sphere and the A-axis and the distance from the sphere center to the A-axis end face were checked again with a dial indicator.

The experiment was conducted at room temperature of $20 \pm 1\ ^{\circ}C$. The geometric errors of the linear axes were identified and compensated using a laser interferometer before this experiment (see Figure 4.12). Additionally, the location errors of the A-axis were measured using conventional methods before the experiment. The A-axis base was adjusted to eliminate the location errors.

Table 4.2 Travel limits of each axis of the six-axis belt-grinding machine

X	-1876 mm to -142.2 mm
Y	-329 mm to 172 mm
Z	183 mm to 685 mm
A	360°
B	from -45° to 45°
C	from -90° to 90°

Table 4.3 Specification of LP2 touch trigger probe

Model type	LP2
Sensing directions	$\pm X$, $\pm Y$ and $+Z$
Unidirectional repeatability	1 μm using 2 σ as estimator
Stylus length	50 mm
Stylus tip radius	6 mm
Measuring force perpendicular to the stylus axis	0.5N – 0.9N
Measuring force along the stylus axis	5.85 N
Signal transmission method	Hard-wired to the CNC control

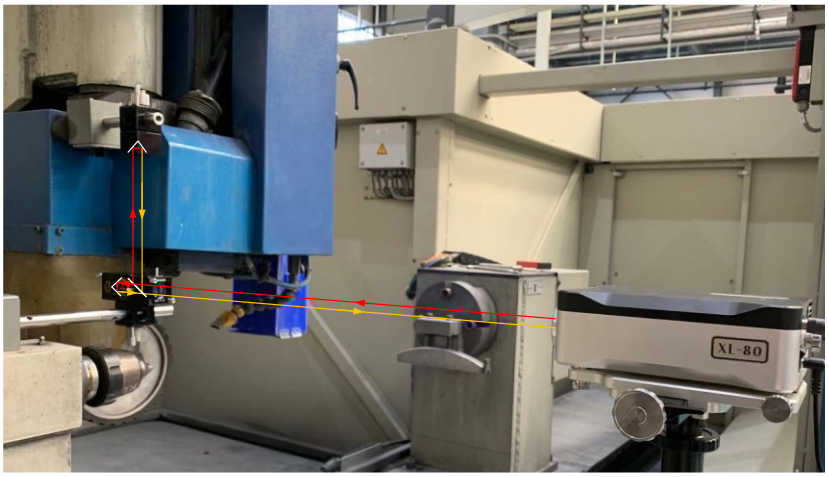

Figure 4.12 Geometric errors of the linear axes were identified with a laser interferometer

4.4.2 Measurement of the probe parameters and the location errors for the rotary axes

In the experiment (see Figure 4.13), to avoid machine over-travel and collision, the experiment range for the machine C-axis was $0^\circ \sim 90^\circ$, and the range for the machine B-axis was $-20^\circ \sim 45^\circ$. The probe aligned its center to the top of the spheres at each pattern described in Section 3. The command values of the machine were captured upon the probe contacting the sphere top. 20 sets of data at the interval of 5° were obtained for Pattern I. Namely, the selected angles for the C axis were

$$C_i = \left\{0^\circ, 5^\circ, 10^\circ \ldots, 85^\circ, 90^\circ\right\} \quad (i = 1, \ldots, 19) \tag{4.41}$$

and both the selected angles for the A-axis and B-axis were 0°. Eq.(4.15), Eq. (4.16) , and Eq.(4.27) were used with the obtained data to identify the link parameters for the probe and the link parameters and the location errors of the C-axis. Similar, 14 sets of data at the interval of 5° were obtained for Pattern II and the selected angles for the B axis were

$$B_j = \left\{-20^{\circ}, -15^{\circ}, \ldots, 40^{\circ}, 45^{\circ}\right\} \quad (j = 1, \ldots, 14) \tag{4.42}$$

and the selected angles for the A-axis was 0° and for the C-axis was 90°. Eq.(4.28), Eq. (4.29) , and Eq.(4.40) were to identify the link parameters for the link parameters and the location errors of the B-axis. A two-touch strategy was employed during the probing process to improve the accuracies of the measurement. At the first touch, the measurement speed was 30 mm/min for rapid positioning of the probe, and at the second touch, the measurement speed was 4 mm/min, at which the command values were captured. After sampling each point, the machine remained idle for 3 minutes to eliminate the influence of the temperature change. The experiment was repeated five times.

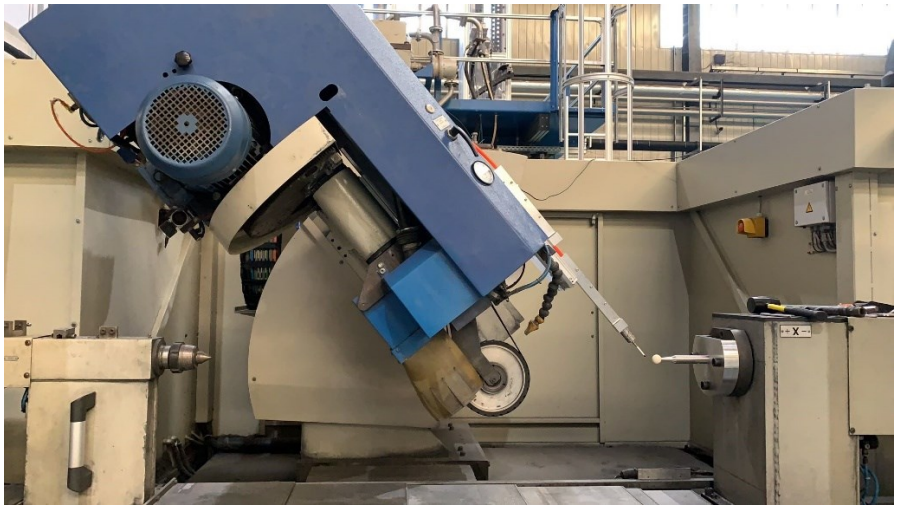

Figure 4.13 Experiment setup

4.4.3 Measurement results

Before the measurement, the geometric errors of the machine linear axes were measured and compensated taking advantage of the CNC machine control's error compensation functionality. The measured location errors of the C-axis and B-axis are presented in Table 4.4. The average squareness errors for the C-axis are 0.0433° for E_{AOC} and 0.0121° for E_{BOC}. The average squareness errors for the B-axis are -0.267° for E_{AOB} and -0.1843° for E_{COB}. These data suggest that the B-axis deviates more from its ideal orientation than the C-axis. The linear location errors for the B-axis, E_{XOB} and E_{ZOB}, are -0.406 mm and 0.544 mm. The linear location errors for the C-axis, E_{XOC} and E_{YOC}, are 0.230 mm and 0.369. These data indicate that the actual B-axis and C-axis are offset significantly from their designed positions. As shown in Table 4.4, the maximum linear location error is up to 0.559 mm (at E_{ZOB}). If this is left uncompensated, the machined parts will have large form deviations, and the grinding belt can even damage the part.

The probe parameters are summarized in Table 4.5 with d_{rpx}, d_{rpy} and d_{rpz} being 85.564 mm, 287.428 mm, and 454.22 mm. They deviate from the design values by 0.564 mm, 1.428mm, and -2.78 mm. The significant probe parameters deviation from the design values can be explained as the probe is a customized add-on component to the machine. Consequently, only a rough estimation is obtained for its design parameters before performing the fine calibration process offered by the proposed method.

Table 4.4 Identified location errors of rotary axes

Location errors	Maximum	Minimum	Average
E_{XOB}	-0.366 mm	-0.431 mm	-0.406 mm
E_{ZOB}	0.559 mm	0.517 mm	0.544 mm
E_{AOB}	-0.2669°	-0.2671°	-0.267°
E_{COB}	-0.181°	-0.184°	-0.184°
E_{XOC}	0.235 mm	0.225mm	0.230 mm
E_{YOC}	0.374 mm	0.364 mm	0.369mm
E_{AOC}	0.0434°	0.0432°	0.0433°
E_{BOC}	0.0122°	0.0120°	0.0121°

Table 4.5 Design and Identified probe parameters (mm)

Probe parameters	d_{rpx}	d_{rpy}	d_{rpz}
Design values	85	286	457
Average	85.564	287.428	454.220
Maximum	85.572	287.434	454.227
Minimum	85.555	287.422	454.214
Deviation of average from the design values	0.564	1.428	-2.78

The error compensation is carried out by inputting the identified location errors and probe parameters to the kinematic model. The actual command values for driving the probe to contact the top of the sphere are calculated with the updated kinematic model. Suppose the theoretical command values when the probe contacts the top of the sphere are $\begin{bmatrix} X_{cmd}^{ca} & Y_{cmd}^{ca} & Z_{cmd}^{ca} \end{bmatrix}^T$ and the recorded command values are $\begin{bmatrix} X_{cmd}^{r} & Y_{cmd}^{r} & Z_{cmd}^{r} \end{bmatrix}^T$. We define the residues between each set of the theoretical and recorded data in the X, Y, and Z directions of $\mathbf{X}_m$ - $\mathbf{Y}_m$ - $\mathbf{Z}_m$ - $\mathbf{O}_m$ as

$$\Delta d_x = X_{cmd}^{ca} - X_{cmd}^{r} \tag{4.43}$$

$$\Delta d_y = Y_{cmd}^{ca} - Y_{cmd}^{r} \tag{4.44}$$

$$\Delta d_z = Z_{cmd}^{ca} - Z_{cmd}^{r} \tag{4.45}$$

To demonstrate the validity of the approach, one set of the experiment data from pattern II is used, and the corresponding command values are calculated using the kinematic model described in Section 3 with the probe parameters and location errors updated according to the average values shown in Table 4.4 and Table 4.5. For each direction in the machine coordinate system (X, Y, and Z), the differences between the theoretical command values and the recorded command values against the input angles for the B axis are shown in Figure 4.14. After compensation, the difference signifies the residual machine geometric error at the given angle sets for the B-axis and the C-axis. As can be seen, the maximum residual machine geometric error is -0.011 mm (in X-direction). Given the repeatability of the linear axes of the CNC belt-grinding machine (about $0.008mm$), this result suggests the proposed method can effectively compensate for the machine geometry errors.

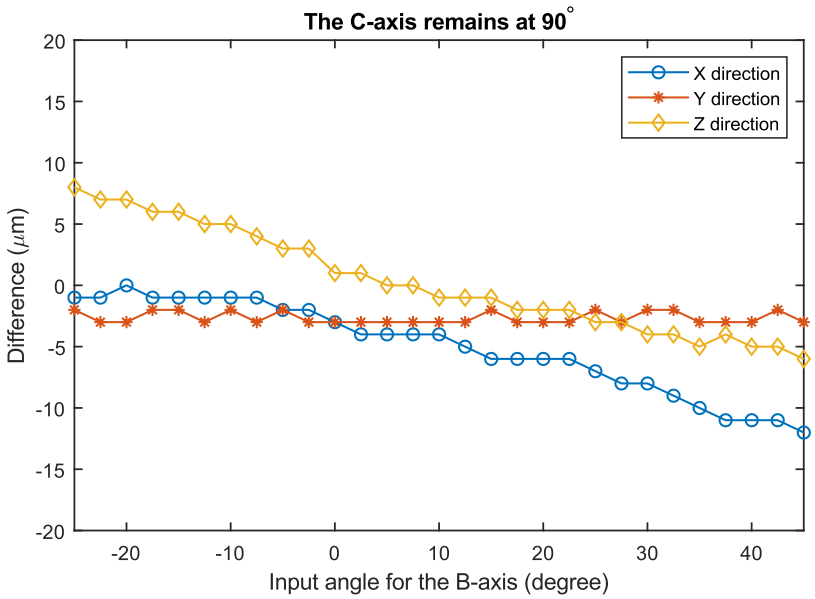

Figure 4.14 The differences between the theoretical command values and the recorded command values against the input angles for the B axis with C = 90°

To further demonstrate the validity of the approach, another 14 sets of command values are measured upon the contact between the probe tip and the sphere top. The input angle for the C axis remains at 70° , and the input angles for the B-axis are

$$B_j = \left\{-20^{\circ}, -15^{\circ}, \ldots, 40^{\circ}, 45^{\circ}\right\} \quad \left(j = 1, \ldots, 14\right) \tag{4.46}$$

The theoretical command values are yielded from using the updated kinematic model. For each direction (X, Y, and Z), the differences between the theoretical command values and the recorded command values against the input angles for the B axis are shown in Figure 4.15. As can be seen, the maximum residual machine geometric error is -0.012 mm (in X-direction). The range of the residual machine geometric errors in a particular direction does not exceed 14 μm , which is similar to those shown in Figure 4.14. This result further validates the effectiveness of the proposed method.

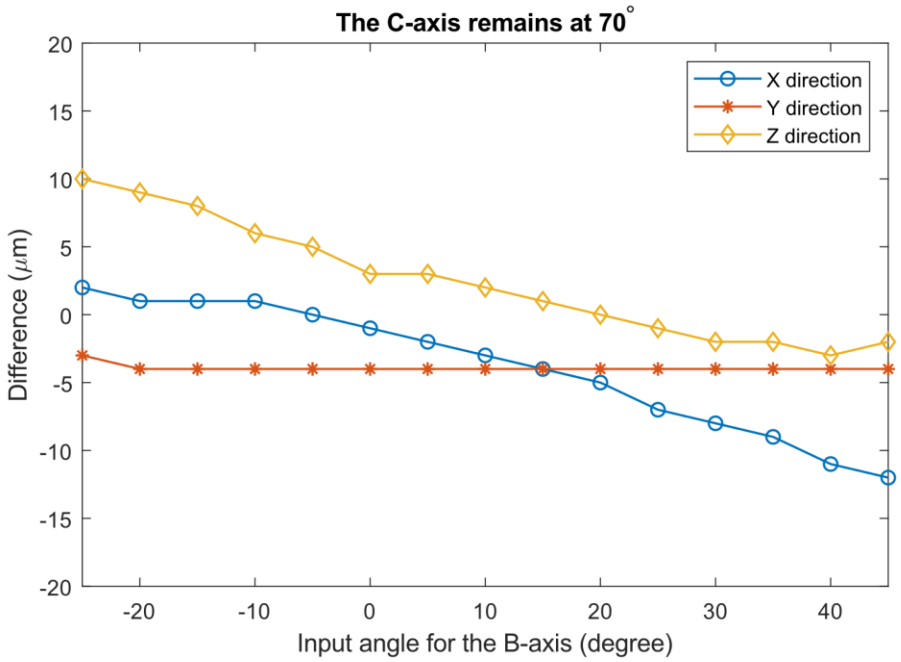

Figure 4.15 The differences between the theoretical command values and the recorded command values against the input angles for the B axis with C = 70°

For a complete estimation of the performance of the proposed method, the synchronous motions were tested for the two rotary axes according to ISO 10791 [25]. In this experiment, each set of test angles are a doublet of input angles for the C-axis and the B-axis. Considering the travel limits of the machine, the following input angles are tested

$$\mathbf{BC}(i)=\begin{Bmatrix}(0^{\circ},0^{\circ}),(85^{\circ},4^{\circ}),(80^{\circ},8^{\circ}),(75^{\circ},12^{\circ}),(70^{\circ},16^{\circ}),\\(65^{\circ},12^{\circ}),(60^{\circ},8^{\circ}),(55^{\circ},4^{\circ}),(50^{\circ},0^{\circ})\end{Bmatrix} \qquad (i=1,2,\ldots,9) \qquad (4.47)$$

where the first angle in the doublet is the angle for the C-axis and the second angle in the pair is the angle for the B-axis. The experiment results are shown in Figure 4.16 and Figure 4.17. In Figure 4.16, the differences of the theoretical command values using the design parameters

and the recorded command values are plot for each input angle set. Significant differences can be witnessed in the figure, up to 2.838 mm in the X-direction. These results prove that the traditional post-processing methods using only design machine parameters obtained from the machine manufacturers can lead to incorrect positioning. Consequently, the machine can damage the workpiece. The on-machine measurement system will detect surface points far away from the intended surface points, rendering large deviations for the measurement results. In Figure 4.17, compensation is made based on the proposed method by calculating the command values with the updated kinematic model. As can be readily seen, the difference between the theoretical command values and the recorded values are significantly reduced to the maximum of 0.024 mm in the X direction, -0.028 mm in the Y direction, and - 0.03mm in the Z direction. The remaining differences in the results are due to the randomness of each machine axes and the inevitable temperature-induced errors. Nevertheless, these results show the effectiveness of the proposed method.

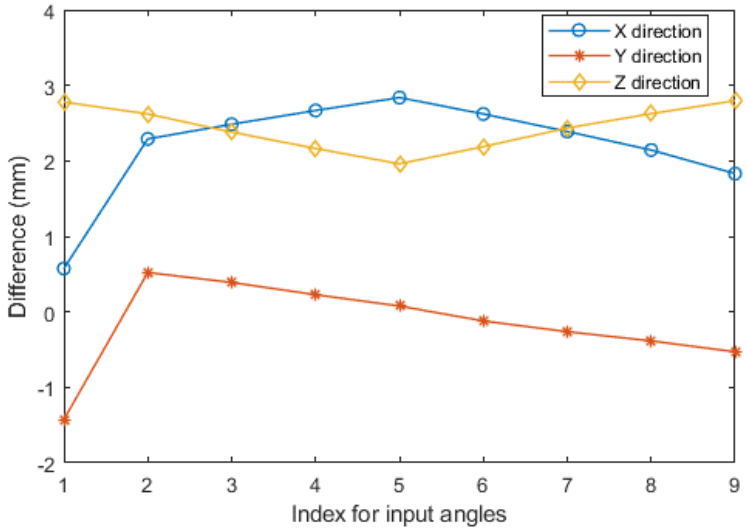

Figure 4.16 The differences between the theoretical command values and the recorded command values against the input angles sets before compensation

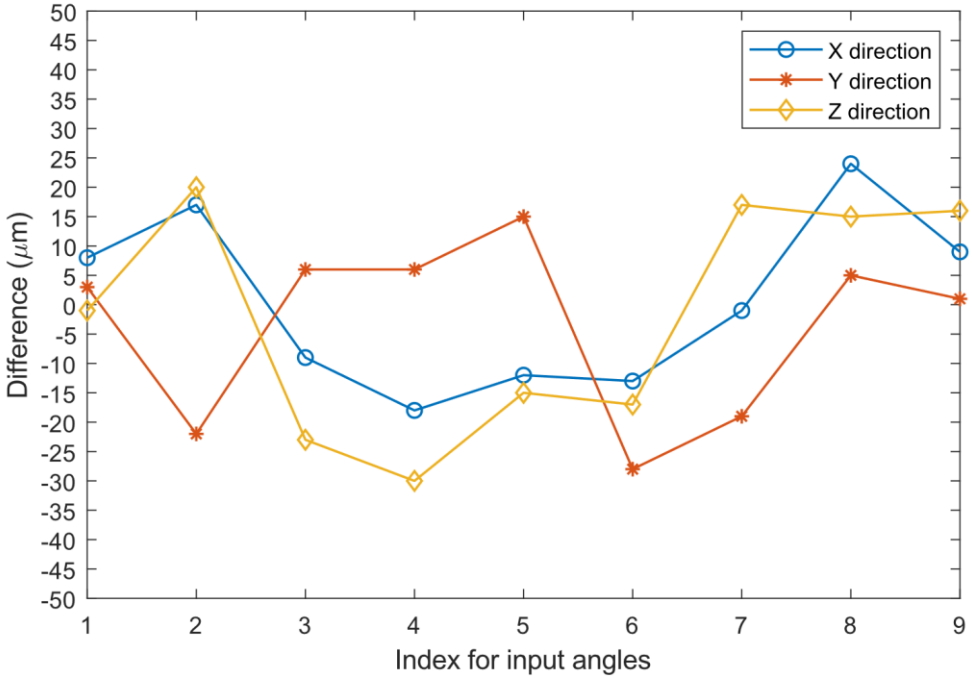

Figure 4.17 The differences between the theoretical command values and the recorded command values against the input angles sets after compensation

4.5 Analysis of the developed method

In this research, two groups of machine components errors and their influences on the calibration results are considered, namely, the accuracy of the rotary axes and the machine linear axes geometric errors. These component errors greatly influence the proposed method because it is assumed that the rotary axes can position to the required angles, and the geometric errors of the linear axes are properly compensated. Consequently, these errors are not represented in

the kinematic model, and they are assumed not to be present in the recorded command values nor the nominal command values. When rotary axis positioning errors exist, the machine linear axes have to travel extra distances to align the probe with the sphere for the measurement tasks, leading to different recorded values. Rotary axes positioning errors are often random errors and not effectively compensated. Thus, their influence must be studied. On the other hand, although the geometric errors of the linear axes are compensated, uncertainties in measuring the linear axes errors render the incomplete compensation of those errors. This will also lead to uncertainties in the recording values whose influences must be estimated on the machine calibration results.

In terms of probing procedures, compensations are carried out to account for the sensitive directional variations of the touch-triggered probe and thus probing uncertainties root from its repeatability. According to the manufacturer's test certificates, the probe uncertainties are about 0.5 μm , which is negligible compared to the geometric uncertainties of the machine linear axes. Regarding the artifact setup errors, the sphere is set up carefully on the A-axis, which is used to define the machine coordinate, with a dial indicator with 1 μm resolution. Hence, the setup error can be neglected. In summary, the machine calibration uncertainty analysis focuses on the positioning error of the rotary axes and both the positioning errors and the location errors of the linear axes.

One appropriate statistical approach to the uncertainty assessment of machine calibration results is Monte Carlo simulation. This approach is well established in [82, 84, 93, 94]. Generally, in Monte Carlo simulation, outputs from the model of interest are calculated with a large number

of possible inputs. The distribution of the outputs is used to represent the output uncertainty. In this research, due to the nonlinear nature of the model, it is convenient to adopt Monte Carlo simulation to estimate the uncertainty of the proposed method for the identification of probe parameters and rotary axes location errors.

The Monte Carlo simulation in this research performs 1000 runs to obtain the distribution of the machine calibration results (for probe parameters and location errors of the rotary axes). Before running the simulation, a set of probe parameters and rotary axes location errors are given. At each run, the recorded command values are modeled for the probing patterns described in Section 3. The proposed method is used to identify the probe parameters and the rotary axes' location errors. The recorded command values can be modeled as

$$\begin{aligned} X_a &= X_{ar} + e_x \\ Y_a &= Y_{ar} + e_y \\ Z_a &= Z_{ar} + e_z \end{aligned} \tag{4.48}$$

where the recorded command values under the influence of the rotary axes positioning errors are X_{ar}, Y_{ar} and Z_{ar}; and e_x, e_y, and e_z are the uncertainties of linear axes positioning errors in the X, Y, and Z directions. X_{ar}, Y_{ar} and Z_{ar} are found in the following fashion. Assuming a small-sized machine and neglecting the radial, axial, and tilt error motions of the rotary axes, the actual positions of the B- and C- axis are

$$B_a = B_n + E_{BB} \tag{4.49}$$

and

$$C_a = C_n + E_{CC} \tag{4.50}$$

where B_n and C_n are the nominal commanded positions of the B- and C- axis; E_{BB} and E_{CC} are the angular positioning errors of the B- and C- axis whose are picked randomly from the ranges listed in Table 4.6. X_{ar}, Y_{ar} and Z_{ar} are computed by inputting B_a and C_a to Eq.(4.23) – Eq.(4.25) and Eq.(4.30) – Eq.(4.32). In addition, e_x, e_y, and e_z are given, according to [95], as

$$\begin{aligned} e_x &= E_{XX} + E_{XY} + E_{XZ} + S_{XZ} \cdot Z_n - S_{XY} \cdot Y_n \\ e_y &= E_{YX} + E_{YY} + E_{YZ} - S_{YZ} \cdot Z_n \\ e_z &= E_{ZX} + E_{ZY} + E_{ZZ} \end{aligned} \tag{4.51}$$

assuming that angular error uncertainties are negligible for each linear axis. The magnitude of each term in Eq.(4.51) is chosen randomly in the range of each geometric error given in Table 4.6. Data in Table 4.6 are obtained from manufacturer specifications, standards, and experiments using conventional measurement methods. The modeled recorded command values are used with Eq.(4.27) and Eq.(4.40) presented in Section 4.3 to identify the probe parameters and the location errors for the rotary axes.

Table 4.6 Contributors and their ranges in machine calibration uncertainty assessment

Contributors	Symbols	Unit	Range
Angular positioning errors of B-axis	E_{BB}	deg	±0.04
Angular positioning errors of C-axis	E_{CC}	deg	±0.04
Squareness of Y- to X-axis	S_{XY}	μm / m	±8
Squareness of Z- to X-axis	S_{XZ}	μm / m	±8
Squareness of Z- to Y-axis	S_{YZ}	μm / m	±8
Linear error of X-axis	E_{XX}	μm	±4
Straightness error of X-axis in Y direction	E_{YX}	μm	±4

Straightness error of X-axis in Z direction	E_{ZX}	μm	± 4
Straightness error of Y-axis in X direction	E_{XY}	μm	± 4
Linear error of Y-axis	E_{YY}	μm	± 4
Straightness error of Y-axis in Z direction	E_{ZY}	μm	± 4
Straightness error of Z-axis in X direction	E_{XZ}	μm	± 4
Straightness error of Z-axis in Y direction	E_{YZ}	μm	± 4
Linear error of Z-axis	E_{ZZ}	μm	± 4

Table 4.7 shows the estimated probe parameters' mean and the rotary axes' location errors against their given quantities. The standard uncertainties of the estimated probe parameters and the location errors for the rotary axes are also listed. As can be seen from Table 4.7, both the standard deviations and the differences between the mean of the estimated values for E_{AOB}, E_{COB}, E_{AOC}, E_{BOC} and their given values are very small. The maximum standard deviation is 0.0013 degrees and the difference is -0.5414×10^{-3} degree. This suggests that the proposed method performs very well in identifying the squareness errors of the rotary axes. For the probe parameters and the linear offsets of the rotary axes, the mean of the estimated values is also very close to the given values. However, the standard deviations are more significant. The maximum standard deviation is 0.022 mm at E_{XOB}. This deviation is believed to originate from uncompensated angular positioning errors. Although this is still acceptable according to the test values given by laser interferometers, it is suggested that the angular positioning errors of the rotary axes need to be measured and compensated before using the proposed method.

Table 4.7 Simulation results for identification

Symbols	Units	Given values	Mean Identified Values	Difference	Standard deviation

d_{rpx}	*mm*	85.557	85.567	0.01	0.012
d_{rpy}	*mm*	287.435	287.430	-0.005	0.006
d_{rpz}	*mm*	454.22	454.221	0.001	0.008
E_{XOB}	*mm*	- 0.417	- 0.406	0.011	0.022
E_{ZOB}	*mm*	0.532	0.534	0.002	0.020
E_{AOB}	deg	-0.2669	-0.2671	-0.1757×10^{-3}	0.0009
E_{COB}	deg	-0.1839	-0.1845	-0.5414×10^{-3}	0.0013
E_{XOC}	*mm*	0.23	0.24	0.01	0.0168
E_{YOC}	*mm*	0.367	0.371	0.004	0.013
E_{AOC}	deg	0.0434	0.0434	-0.0073×10^{-3}	0.0006
E_{BOC}	deg	0.0121	0.0122	0.0625×10^{-3}	0.0007

4.6 Summary

This chapter offers a complete on-machine measurement system establishment scheme for multi-axis machine tools. The pre-certified sphere artifact used in the method allows for easy set-up, and the fully automated probing programs significantly reduce the operation difficulties compared to traditional calibration methods such as DBB and R-tests. The proposed method calibrates the machine geometric errors and the probe parameters simultaneously. The experiment results show that the proposed method is accurate and is very necessary in machines with difficult-to-measure link parameters such as probe parameters and rotary axes positions (in which case, design link parameters are often wrongly used for post-processing). Uncertainty analysis shows that the method is robust even though randomness occurs in measurement procedures' rotating and linear motions. Finally, the proposed method is beneficial for establishing on-machine measurement systems in special purposed CNC machines without traditional tool-holding spindles. In this case, determining the probe center location in the

machine coordinate system is difficult. The method can be extended to general multi-axis CNC machines for rotary axes location determination purposes.

Chapter 5

Conclusions and future work

5.1 Conclusions

In this work, some critical scientific methods for high precision and high-efficiency on-machine measurement have been proposed. The focuses were mainly on the studies of geometric principles of on-machine tool settings with laser tool setters and the studies of kinematic modeling of machine calibrations. The major contributions of this work were concluded as the followings:

1) A new mechanism for gauging the laser axis in practical situations was developed and a new and applied mathematical model for calculating the area of the shaded region was proposed. Based on these fundamentals, an approach to calculating the Z-coordinate of the rod bottom center in the tool setter coordinate system was established. The machine kinematics chain was derived to accurately determine the coordinates of the laser axis reference point in the machine coordinate system. These approaches improve the laser tool setter accuracy, and its tool setting accuracy and can greatly promote on-machine tool setting with laser tool setters in the industry.

2) The tool length characteristic curve was discovered originally in this work, by modeling the on-machine tool length measurement process with laser tool setters. This curve reveals the length and the wear of all the flutes of a round-inserted mill being measured.

It allows for tool setting and tool condition monitoring to be performed on machine, which was once only possible on an expensive offline tool presetter.

3) A novel calibration method was proposed to address current difficulties for multi-axis CNC on-machine measurement. This work provides a means for simultaneous identification of the probe parameters and the location errors of rotary axes, using a touch-triggered probe to sample a sphere. The method formulates a mathematical model based on machine kinematics to represent errors between the theoretical probed data and the actual recorded data, minimizing which can solve for necessary parameters. Two proposed probing patterns simplify the solution to the model. Experiment results demonstrate that the method is effective and accurate. Monte Carlo simulations were carried out to prove the robustness of the method. The proposed method offered a low-cost and efficient way for both periodic machine checks and OMM system recalibrations.

5.2 Future work

For future work, the following topics are recommended to expand the current research:

1) Cutting tool radius and flute radial wear conditions on-machine measurement can be developed;

   Tool radius and flute radial wear conditions are important factors during manufacturing tasks. Since there is a lack of geometric models for tool radius and flute radial wear, the current industry treats this problem via the trial and error approach, leading to the waste

of tools and even scrapes. It is thus recommended to build such a geometric model to measure these important parameters.

2) On-machine tool measurement models with laser tool setters can be developed for all sorts of tools, such as end-mills, ball end-mills, drills, etc.

3) A holistic machine calibration method using on-machine measurement techniques can be developed.

   Geometric errors exist in the whole machine's working volume and they should be compensated accordingly. The results can improve both manufacturing performance and on-machine measurement accuracy.

5.3 Publications related to the thesis

[1] Fang, Zixi, et al. "Simultaneous calibration of probe parameters and location errors of rotary axes on multi-axis CNC machines by using a sphere." Measurement 188 (2022): 110389.

[2] Fang, Zixi and Chen, Zezhong. “Novel techniques of on-machine tool setting with laser tool setters: precise mathematical model for computer simulation of gauging in practical situations and its application in the calibration process.” International Journal of Machine Tools and Manufacture, Under review.

[3] Fang, Zixi and Chen, Zezhong. “An accurate and efficient approach for measuring the round insert end-mill length and bottom cutting edges wear with on-machine laser tool setters.” International Journal of Machine Tools and Manufacture, Under review.

References

[1] R.Y. Zhong, X. Xu, E. Klotz, S.T. Newman, Intelligent manufacturing in the context of industry 4.0: a review, J Engineering, 3 (2017) 616-630.
[2] A.B. Feeney, S.P. Frechette, V. Srinivasan, A portrait of an ISO STEP tolerancing standard as an enabler of smart manufacturing systems, J Journal of computing information science in engineering, 15 (2015).
[3] S.L. Robinson, R.K. Miller, Automated inspection and quality assurance, CRC Press, 2017.
[4] J. Berthold, D.J.J.o.S. Imkamp, S. Systems, Looking at the future of manufacturing metrology: roadmap document of the German VDI/VDE Society for Measurement and Automatic Control, 2 (2013) 1-7.
[5] H. Eldessouky, S. Newman, A. Nassehi, Closed loop CNC machining and inspection of interlinked manufacturing features for “Right First Time” production, 2015.
[6] R. Guiassa, J. Mayer, M. Balazinski, S. Engin, F.-E. Delorme, Closed door machining error compensation of complex surfaces using the cutting compliance coefficient and on-machine measurement for a milling process, J International Journal of Computer Integrated Manufacturing, 27 (2014) 1022-1030.
[7] M. Verma, E. Chatzivagiannis, D. Jones, P. Maropoulos, Comparison of the measurement performance of high precision multi-axis metal cutting machine tools, J Procedia CIRP, 25 (2014) 138-145.
[8] Usinedufutur.safran-group.com, The production lines at Safran are becoming autonomous (2009).
[9] Renishaw, Probing systems for CNC machine tools 2014, Part No. H-2000-3020-10-A.
[10] ISO 230-1:2012, Test code for machine tools — Part 1: Geometric accuracy of machines operating under no-load or quasi-static conditions, 2012.
[11] https://www.machinery.co.uk/content/news/thermal-compensation-to-become-standard-for-mori-seiki-machines, Thermal compensation to become standard for Mori Seiki machines.(2006).
[12] ISO 10791-2:2001, Test conditions for machining centres — Part 2: Geometric tests for machines with vertical spindle or universal heads with vertical primary rotary axis (vertical Z-axis), (2001).
[13] H.J. Pahk, Y.S. Kim, J.H. Moon, A new technique for volumetric error assessment of CNC machine tools incorporating ball bar measurement and 3D volumetric error model, J International Journal of Machine Tools Manufacture, 37 (1997) 1583-1596.

[14] R. Schultschik, The components of the volumetric accuracy, J A CIRP, 26 (1977) 223-226.
[15] A.W. Khan, W. Chen, A methodology for systematic geometric error compensation in five-axis machine tools, J The International Journal of Advanced Manufacturing Technology, 53 (2011) 615-628.
[16] V. Kiridena, P.M. Ferreira, Mapping the effects of positioning errors on the volumetric accuracy of five-axis CNC machine tools, J International Journal of Machine Tools Manufacture, 33 (1993) 417-437.

[17] A. Srivastava, S. Veldhuis, M. Elbestawit, Modelling geometric and thermal errors in a five-axis CNC machine tool, J International Journal of Machine Tools Manufacture, 35 (1995) 1321-1337.

[18] S. Xiang, Y. Altintas, Modeling and compensation of volumetric errors for five-axis machine tools, J International Journal of Machine Tools Manufacture, 101 (2016) 65-78.
[19] S. Zhu, G. Ding, S. Qin, J. Lei, L. Zhuang, K. Yan, Integrated geometric error modeling, identification and compensation of CNC machine tools, International journal of machine tools manufacture, 52 (2012) 24-29.
[20] J.H. Lee, Y. Liu, S.-H. Yang, Accuracy improvement of miniaturized machine tool: geometric error modeling and compensation, J International Journal of Machine Tools Manufacture, 46 (2006) 1508-1516.
[21] J. Yang, Y. Altintas, Generalized kinematics of five-axis serial machines with non-singular tool path generation, J International Journal of Machine Tools Manufacture, 75 (2013) 119-132.
[22] H. Schwenke, W. Knapp, H. Haitjema, A. Weckenmann, R. Schmitt, F. Delbressine, Geometric error measurement and compensation of machines—an update, J CIRP annals, 57 (2008) 660-675.
[23] ISO 10791-1:2015, Test conditions for machining centres — Part 1: Geometric tests for machines with horizontal spindle (horizontal Z-axis), 2015.
[24] ISO 10791-3:1998, Test conditions for machining centres — Part 3: Geometric tests for machines with integral indexable or continuous universal heads (vertical Z -axis), 1998.
[25] ISO 10791-4:1998, Test conditions for machining centres — Part 4: Accuracy and repeatability of positioning of linear and rotary axes, (1998).
[26] N. Huang, Q. Bi, Y. Wang, Identification of two different geometric error definitions for the rotary axis of the 5-axis machine tools, J International Journal of Machine Tools Manufacture, 91 (2015) 109-114.
[27] Renishaw plc, XL-80 laser measurement system (L-9908-1300-01-B), 2016.
[28] S. Ibaraki, W. Knapp, Indirect measurement of volumetric accuracy for three-axis and five-axis machine tools: a review, J International Journal of Automation Technology, 6 (2012) 110-124.
[29] M. Givi, J. Mayer, Validation of volumetric error compensation for a five-axis machine using surface mismatch producing tests and on-machine touch probing, J International Journal of Machine Tools Manufacture, 87 (2014) 89-95.
[30] Y.-T. Chen, P. More, C.-S. Liu, Identification and verification of location errors of rotary axes on five-axis machine tools by using a touch-trigger probe and a sphere, J The International Journal of Advanced Manufacturing Technology, 100 (2019) 2653-2667.
[31] FANUC, FANUC Series 0+ Mate-MODEL D Common to Lathe System / Machining Center System Operator's Manual (B-64304EN/02).
[32] SIEMENS, SINUMERIK 840D sl / 828D Job Planning, 2013.
[33] S. Fraser, M.H. Attia, M.O.M. Osman, Modelling, Identification and Control of Thermal Deformation of Machine Tool Structures, Part 1: Concept of Generalized Modelling, Journal of Manufacturing Science and Engineering, 120 (1998) 623-631.

[34] S. Fraser, M.H. Attia, M.O.M. Osman, Modelling, Identification and Control of Thermal Deformation of Machine Tool Structures, Part 2: Generalized Transfer Functions, Journal of Manufacturing Science and Engineering, 120 (1998) 632-639.
[35] H. Zou, B. Wang, Investigation of the contact stiffness variation of linear rolling guides due to the effects of friction and wear during operation, J Tribology international, 92 (2015) 472-484.
[36] E. Gomez-Acedo, A. Olarra, L.J.T.I.J.o.A.M.T. Lopez de La Calle, A method for thermal characterization and modeling of large gantry-type machine tools, 62 (2012) 875-886.
[37] A. Woźniak, M. Dobosz, Metrological feasibilities of CMM touch trigger probes. Part I: 3D theoretical model of probe pretravel, J Measurement, 34 (2003) 273-286.
[38] Y.-L. Shen, X. Zhang, Pretravel compensation for vertically oriented touch-trigger probes with straight styli, J International Journal of Machine Tools Manufacture, 37 (1997) 249-262.
[39] T. Jarman, A. Traylor, Performance characteristics of touch trigger probes, J Proceedings of precision metrology with coordinate measurement systems, (1990).
[40] P. Cauchick-Miguel, T. King, Factors which influence CMM touch trigger probe performance, J International Journal of Machine Tools Manufacture, 38 (1998) 363-374.
[41] Renishaw, Inspection Plus for machining centres with Fanuc and Meldas controllers, 2018, Part No. H-5755-8600-03-A.
[42] Y. Shen, S. Moon, Mapping of probe pretravel in dimensional measurements using neural networks computational technique, J Computers in Industry, 34 (1997) 295-306.
[43] J. RenéMayer, A. Ghazzar, O. Rossy, 3D characterisation, modelling and compensation of the pre-travel of a kinematic touch trigger probe, J Measurement, 19 (1996) 83-94.
[44] W.T. Estler, S.D. Phillips, B. Borchardt, T. Hopp, C. Witzgall, M. Levenson, K. Eberhardt, M. McClain, Y. Shen, X. Zhang, Error compensation for CMM touch trigger probes, J Precision Engineering, 19 (1996) 85-97.
[45] Y. Shen, M.E. Springer, A Robust Pretravel Model for Touch Trigger Probes in Coordinate Metrology, Journal of Manufacturing Science and Engineering, 120 (1998) 532-539.
[46] M. Jankowski, A. Wozniak, Mechanical model of errors of probes for numerical controlled machine tools, J Measurement, 77 (2016) 317-326.
[47] W. Reiser, Laser system for non-contact tool setting and breakage detection, J WIT Transactions on Engineering Sciences, 16 (1970).
[48] O. Ryabov, K. Mori, N. Kasashima, Laser displacement meter application for milling diagnostics, J Optics lasers in engineering, 30 (1998) 251-263.
[49] P. Khajornrungruang, K. Kimura, K. Suzuki, On-machine measurement of a distance between high speed rotation tool tip and workpiece by laser diffraction, 2012.
[50] C. Zhang, J. Zhang, On-line tool wear measurement for ball-end milling cutter based on machine vision, J Computers in industry, 64 (2013) 708-719.
[51] G. Shi, J. Liu, Z. Yu, G. Shi, Laser diffraction application on detection technology of online tool setting, IEEE, 2015, pp. 62-64.
[52] G. Shi, Y. Zhang, H. Zhang, J. Wang, G. Shi, Analysis of the influence of installation tilt error on the tool setting accuracy by laser diffraction, J Applied optics, 57 (2018) 3012-3020.
[53] Heidenhain, Touch probes for machine tools, 2019, Part No. 1113984-25 · 10.
[54] Hexagon, m&h laser tool setters measuring on machine tools, 2017.

[55] Renishaw, Renishaw's non-contact laser tool setting technology 2011, Part No. H-5650-2024-01-B.
[56] Renishaw, Understanding non-contact tool setting, 2013, Part No. pd-4114-9043-02-c.
[57] V.G. Stimpson, Merrifield, Benjamin J, Measuring device and method for detecting objects interrupting a beam of radiation, U.S. Patent 7,312,433, 2007.
[58] H.W. Park, Y.B. Park, S.Y. Liang, Non-contact measurement methods for micro-and meso-scale tool positioning, J The International Journal of Advanced Manufacturing Technology, 60 (2012) 251-260.
[59] H.-H. Lee, W.-C. Shin, S.-K. Ro, J.-K. Park, M. Noh, Optical Sensor Using Light Intensity Modulation: Feasibility Test, IEEE, 2008, pp. 182-185.
[60] Z.-L. Li, L.-M. Zhu, Envelope surface modeling and tool path optimization for five-axis flank milling considering cutter runout, J Journal of Manufacturing Science Engineering, 136 (2014).
[61] M. Wan, W.-H. Zhang, J.-W. Dang, Y. Yang, New procedures for calibration of instantaneous cutting force coefficients and cutter runout parameters in peripheral milling, J International Journal of Machine Tools Manufacture, 49 (2009) 1144-1151.
[62] Renishaw, Non-contact tool setting software: Programming guide, 2016.
[63] E.S. Lee, C.H. Lee, S.C. Kim, Machining accuracy improvement by automatic tool setting and on machine verification, Trans Tech Publ, 2008, pp. 199-202.
[64] M. Vieira Júnior, F.H. Pereira, W.C. Lucato, F.S. da Costa, Influence of feed rate and spindle speed on referencing laser tool-setters, J Journal of the Brazilian Society of Mechanical Sciences Engineering, 37 (2015) 1015-1028.
[65] S.A. Ashton, V.G. Stimpson, J.P. Fuge, D.R. McMurtry, Machine tool analysis device and method, U.S. Patent 7,315,018, 2008.
[66] Renishaw, Non-contact tool setting system for Heidenhain TNC 620/640 controllers, 2018, Part No. H-2000-6885.
[67] Z.-L. Li, J.-B. Niu, X.-Z. Wang, L.-M. Zhu, Mechanistic modeling of five-axis machining with a general end mill considering cutter runout, J International Journal of Machine Tools Manufacture, 96 (2015) 67-79.
[68] C.M. Hoffmann, J.E. Hopcroft, The potential method for blending surfaces and corners, Cornell University, 1985.
[69] H. Chiyokura, An extended rounding operation for modeling solids with free-form surfaces, in: Computer graphics 1987, Springer, 1987, pp. 249-268.
[70] B.K. Choi, S. Ju, Constant-radius blending in surface modelling, J Computer-Aided Design, 21 (1989) 213-220.
[71] Y. Tokuyama, S. Bae, An approximate method for generating draft on a free-form surface, J The Visual Computer, 1 (1999) 1-8.
[72] G. Elber, Curve evaluation and interrogation on surfaces, J Graphical Models, 63 (2001) 197-210.
[73] D.S. Arnon, Topologically reliable display of algebraic curves, J ACM SIGGRAPH Computer Graphics, 17 (1983) 219-227.
[74] D. Sutcliffe, An algorithm for drawing the curve f (x, y)= 0, J The Computer Journal, 19 (1976) 246-249.

[75] R.E. Chandler, A tracking algorithm for implicitly defined curves, J IEEE Computer Graphics Applications, 8 (1988) 83-89.
[76] I.D. Faux, M.J. Pratt, Computational geometry for design and manufacture, (1979).
[77] I.E. Sutherland, G.W. Hodgman, Reentrant polygon clipping, J Communications of the ACM, 17 (1974) 32-42.
[78] B.R. Vatti, A generic solution to polygon clipping, J Communications of the ACM, 35 (1992) 56-63.
[79] G. Greiner, K. Hormann, Efficient clipping of arbitrary polygons, J ACM Transactions on Graphics, 17 (1998) 71-83.
[80] D. Zwillinger, CRC standard mathematical tables and formulas, chapman and hall/CRC, 2018.
[81] Renishaw, Renishaw – cranking down cycle time for Hope Technology, 2017.
[82] P. Pérez, S. Aguado, J. Albajez, J. Santolaria, Influence of laser tracker noise on the uncertainty of machine tool volumetric verification using the Monte Carlo method, J Measurement Science Technology, 133 (2019) 81-90.
[83] Q. Bi, N. Huang, C. Sun, Y. Wang, L. Zhu, H. Ding, Identification and compensation of geometric errors of rotary axes on five-axis machine by on-machine measurement, J International Journal of Machine Tools Manufacture, 89 (2015) 182-191.
[84] S. Ibaraki, T. Iritani, T. Matsushita, Calibration of location errors of rotary axes on five-axis machine tools by on-the-machine measurement using a touch-trigger probe, J International Journal of Machine Tools Manufacture, 58 (2012) 44-53.
[85] Z. Jiang, B. Song, X. Zhou, X. Tang, S. Zheng, On-machine measurement of location errors on five-axis machine tools by machining tests and a laser displacement sensor, J International Journal of Machine Tools Manufacture, 95 (2015) 1-12.
[86] M. Tsutsumi, A. Saito, Identification and compensation of systematic deviations particular to 5-axis machining centers, J International Journal of Machine Tools Manufacture, 43 (2003) 771-780.
[87] M. Tsutsumi, S. Tone, N. Kato, R. Sato, Enhancement of geometric accuracy of five-axis machining centers based on identification and compensation of geometric deviations, J International Journal of Machine Tools Manufacture, 68 (2013) 11-20.
[88] R. Ramesh, M. Mannan, A. Poo, Error compensation in machine tools—a review: part I: geometric, cutting-force induced and fixture-dependent errors, J International Journal of Machine Tools Manufacture, 40 (2000) 1235-1256.
[89] ISO 230-7:2015, Test code for machine tools — Part 7: Geometric accuracy of axes of rotation, ISO 230-7:2015, 2015.
[90] J. Yang, J. Mayer, Y. Altintas, A position independent geometric errors identification and correction method for five-axis serial machines based on screw theory, J International Journal of Machine Tools Manufacture, 95 (2015) 52-66.
[91] R.-S. Lee, C.-H. She, Developing a postprocessor for three types of five-axis machine tools, J The International Journal of Advanced Manufacturing Technology, 13 (1997) 658-665.
[92] ISO 841:2001, Industrial automation systems and integration — Numerical control of machines — Coordinate system and motion nomenclature, 2001.

[93] B. Bringmann, W. Knapp, Machine tool calibration: Geometric test uncertainty depends on machine tool performance, J Precision Engineering, 33 (2009) 524-529.
[94] A. Los, J. Mayer, Application of the adaptive Monte Carlo method in a five-axis machine tool calibration uncertainty estimation including the thermal behavior, J Precision Engineering, 53 (2018) 17-25.
[95] J.A. Soons, Analysis of the step-diagonal test, 2005, pp. 126-137.